Collinear Factorization at sub-asymptotic kinematics and validation in a diquark spectator model

Juan V. Guerrero*

Jefferson Lab, Newport News, VA 23606, USA and

Department of Physics, Old Dominion University, Norfolk, Virginia 23529, USA

Alberto Accardi[†]
Hampton University, Hampton, VA 23668, USA and
Jefferson Lab, Newport News, VA 23606, USA

(Dated: October 16, 2020)

We revisit the derivation of collinear factorization for Deep Inelastic Scattering at sub-asymptotic values of the four momentum transfer squared, where the masses of the particles participating in the interaction cannot be neglected. By using an inclusive jet function to describe the scattered quark final state, we can restrict the needed parton kinematic approximations just to the overall four-momentum conservation of the hard scattering process, and explicitly expand the rest of the diagram in powers of the unobserved parton transverse momenta rather than neglecting those. This procedure provides one with more flexibility in fixing the virtuality of the scattered and recoiling partons, and naturally leads to scaling variables that more faithfully represent the partonic kinematic at sub-asymptotic energy than Bjorken's x_B variable.

We verify the validity of the obtained factorization formula by considering a diquark spectator model designed to reproduce the main features of electron-proton scattering at large x_B in Quantum Chromo-Dynamics, where the Deep Inelastic Scattering contribution to the cross section can be explicitly isolated and analytically calculated. Limiting ourselves to the leading twist contribution, we show that use of the new scaling variables maximizes the kinematic range of validity of collinear factorization, and highlight the intrinsic limitations of this approach due to the approximate treatment of four momentum conservation in factorized diagrams. Finally, we briefly discuss how these limitations may be overcome by including higher-twist corrections to the factorized calculation.

^{*} juanvg@jlab.org

 $^{^{\}dagger}$ accardi@jlab.org

CONTENTS

I.	Introduction and overview	3
II.	Diquark spectator model as a proxy for $\mathbf{e} + \mathbf{p}$ scattering A. Calculation of the hadronic tensor B. Gauge invariant decomposition into DIS, resonance, and interference processes C. Kinematics D. Transverse structure function E. Longitudinal structure function	4 6 8 9 11 13
III.	Collinear factorization at sub-asymptotic momentum transfer A. Derivation B. Discussion	15 15 18
IV.	Testing the kinematic approximations A. Kinematic approximations B. Average internal variables C. Numerical validation	19 19 20 20
V.	Testing the limits of factorization A. Validity of the factorization approximations B. Breaking of Collinear Factorization C. Discussion: theory and phenomenology beyond the leading twist	24 24 26 28
VI.	Summary and conclusions A. Collinear Factorization in DIS at sub-asymptotic Q^2 B. Beyond Deep Inelastic Scattering	29 29 30
	Acknowledgments	30
Α.	Invariant and helicity structure functions	31
В.	Scaling at small x_B 1. Small- x_B scaling of F_L 2. Small- x_B scaling of F_T	33 33 35
С.	Kinematic bounds 1. Limits on x_B 2. Limits on k_T^2 3. Exact solutions of the delta functions 4. Approximating v^2 in DIS 5. Approximating v'^2 in DIS	36 36 36 37 38 39
D.	Model systematics	40
	References	43

I. INTRODUCTION AND OVERVIEW

Unraveling the quark and gluon structure of the nucleon still remains a major challenge in hadronic and particle physics notwithstanding the significant experimental and theoretical advances made in this area throughout the last decade [1–5].

The Large Hadron Collider can measure a large variety of observables, especially at the energy frontier, and access the proton structure at the smallest scales. However utilizing its data remains challenging due to tensions between various observables, and its impact on the determination of unpolarized Parton Distribution Functions (PDFs) is so far somewhat statistically limited [6–8]. Proton-proton collisions at the Relativistic Heavy Ion Collider (RHIC) provide complementary access to PDFs at lower energy scale and higher parton fractional momentum, notably in polarized collisions. Use of RHIC data in unpolarized PDF fits has however not received much attention, so far, despite its potential for flavor separation of sea quarks via weak boson production data, and gluon PDF determination through jet observables. Lowering the collision energy and changing reaction to electron-proton collisions, recent data from the Jefferson Lab 6 GeV program and those being collected at its 12 GeV upgrade [9, 10], as well as those expected from the future Electron Ion Collider [11, 12] will enable us to access quarks and gluons in unprecedented ways, and to build an accurate, 3-dimensional picture of the inner structure of the proton.

In order to use high-energy scattering data to describe the proton's structure in terms of quark and gluon PDFs one relies on QCD factorization theorems, such as Collinear Factorization (CF) [13]. These theorems allow one to write the cross sections of large momentum transfer scattering processes such as Deep Inelastic Scattering (DIS) as a convolution of a short distance matrix element, which can be computed perturbatively and describes the quark and gluon "hard" interaction with a probe, and long distance non perturbative matrix elements – the PDFs – that describe the quark and gluon momentum distribution within the proton.

In this paper we are interested in assessing the viability of Collinear Factorization in describing DIS events with large enough 4-momentum transfer to justify a perturbative QCD analysis of the cross sections in terms of quark and gluon interactions, but not large enough to neglect any other mass or dynamical momentum scale characterizing the process. For example, experiments at Jefferson Lab with a 6 GeV energy beam, involve low photon virtualities Q^2 that require control of $1/Q^2$ power corrections to the calculation of cross sections. At 12 GeV, the accessible Q^2 increases, without, however, reaching asymptotic values. In this sub-asymptotic regime, for example, the mass of the proton target and the mass of an observed hadron, both denoted by μ , induce finite- Q^2 corrections of order μ^2/Q^2 , which we call "Hadron Mass Corrections" (HMCs). These can compete with the experimental uncertainties at Jefferson Lab energy, and can also affect higher-energy experiments such as HERMES and COMPASS, see Refs. [14–16]. These papers propose to not only take into account the target's and observed hadron mass through a rescaling of the Bjorken variable x_B , as already discussed in [17–19], but to also account for the fact that the scattered parton needs to have a virtuality substantially different from 0 in order to fragment into a massive hadron. This kinematic requirement can in fact be implemented in a gauge invariant way through a modified scaling variable, and numerical estimates at JLab kinematics suggest large effects for pions, and even more for kaons or heavier hadrons [15]. In fact, HMCs may even explain [16] the apparent large discrepancy between the measurements of integrated kaon multiplicities performed at HERMES and COMPASS [20–22]. Two subsequent papers from the COMPASS collaboration have furthermore analyzed kaons and protons produced at even larger hadron momentum fractions than reported before, highlighting strong departures from pQCD calculations [23, 24]. This discrepancy between theory and experiment seems too large to be only due to the phase space limitations induced by finite mass effects (which could be treated as a correction to the usual pQCD formalism, as for example discussed in Refs. [15, 16]) and may indicate that the factorization formalism is being applied in a kinematic region where this is not a good approximation to the semi-inclusive cross section.

If the correct treatment of the partonic kinematics and the very validity of QCD factorization are under question at high-energy experiments such as HERMES and COMPASS already for transverse momentum integrated observables, investigating these issues becomes essential for a correct interpretation of the upcoming semi-inclusive measurements at the JLab 12 GeV upgraded facility [9, 10], since the $p_{h\perp}$ -dependent cross sections are even more sensitive to HMCs than their integrated counterparts, and the partonic 3D imaging of the proton encounters novel challenges of its own [25, 26].

In this paper, we will approach these issues in the framework of a QCD-like idealized field-theoretical model describing a spin 1/2 idealized nucleon, which contains an active quark as well as a scalar diquark that does not participate in the interaction [27, 28], and complete the analysis presented in Refs. [29, 30]. In the chosen "diquark spectator model", one can perform fully analytic calculations of the DIS cross section, as well as collinear factorization with or without HMCs. The model is designed to reproduce the main feature of the QCD process at large x_B , and a comparison of the full and collinearly factorized cross sections will determine the validity of the proposed HMC scheme, as well as test the limit of collinear factorization itself. To start with, in this paper we will discuss inclusive DIS scattering, where we can avoid purely technical complications due to the interplay of initial and final state kinematics

[15], and limit ourselves to Leading-Order (LO) perturbative calculations, that do not require renormalization of the quark fields and limit the final state to 2 particles. Nonetheless, we will be able to address in full the need for, and means of, an improved kinematic approximation. Furthermore, working within an explicit model we will be able to investigate the role of the parton's transverse momentum, that is by necessity neglected in the Leading-Twist calculation of the inclusive DIS cross section, but contributes to Higher-twist (HT) $O(\langle k_T^2 \rangle/Q^2)$ corrections. As we will very briefly discuss in Section VI A, we believe that an extension of our HMC scheme to Next-to-Leading Order (NLO) – and, in fact, also to SIDIS – should not encounter essential difficulties .

The paper is organized as follows. In Section II, we present the diquark spectator model adopted for our study, and use this to calculate the inelastic lepton-proton cross section at LO. We then show how the cross section can be decomposed in a gauge invariant way into DIS, proton resonance, and interference contributions, and study in detail the proton's F_T and F_L transverse and longitudinal structure functions as well as their scaling properties with respect to the photon virtuality Q^2 . The low- x_B behavior of the model also turns out to be interesting, even if the model is not designed to provide one with a realistic description of experimental measurements in that regime. Indeed, our explicit calculation will highlight a quite different Q^2 scaling of the DIS component of F_L compared to simple dimensional arguments and to what happens for F_T . As we will explain, this is however a general consequence of gauge invariance rather than a model artifact, which may also explain the need for phenomenological $O(1/Q^2)$ corrections in order for CF calculation of F_L to agree with recent HERA data at small values of the Bjorken invariant x_B [31].

In Section III, we discuss our proposal for performing Collinear Factorization of the DIS structure functions at sub-asymptotic hard scale Q^2 , and how one can account for hadron masses and non-zero parton virtualities in the treatment of partonic kinematics. Our central tenet is to confine the needed "pure" kinematic to the external kinematics of the partonic hard-scattering, and to perform a controlled, "twist" expansion of the rest of the diagram. The end result is quite simple: at leading twist (LT), the cross section and its structure functions are given by their asymptotic (or massless) counterparts evaluated at a suitably defined scaling variable \bar{x} instead of x_B . This is not an entirely new concept, as it has been proposed in a similar context by, for example, in Refs. [17, 18, 32, 33] and even earlier in Refs. [34–37]. Here we attempt, however, at a more systematic treatment that avoids a priori parton model considerations. In fact our end result cannot be interpreted in parton model terms except in well defined limits, but, conversely, gives one enhanced freedom in devising realistic kinematic approximations to the full process. In particular, as already mentioned, the virtuality of the partons needs not be approximated to zero, and can be chosen differently for the incoming and scattered quarks without breaking gauge invariance.

The choice of scaling variable can be motivated by studying the kinematics of the handbag diagram, and tested against full model calculations. This is accomplished in Section IV, where the approximated parton momentum fraction and virtuality is compared to the average values calculated in the full model. In particular, we show that one can approximate to the 90% level the average parton fractonal momentum by including all external mass scales in the quark-mass-corrected Nachtmann scaling variable $\xi_q = \xi(1 + m_q^2/Q^2)$ (where m_q is the quark mass the Nachtmann variable ξ [37] accounts for the proton mass); small corrections of $O(\langle k_T^2 \rangle/Q^2)$ account for the rest.

These conclusions are confirmed in Section V, where we compare the full and factorized transverse F_T structure functions and show that only corrections of order $O(\langle k_T^2 \rangle/Q^2)$ are needed to describe the full structure functions after removing all mass corrections by the use of the ξ_q in our generalized CF formula. ($F_L=0$ at LO in collinear factorization, and is not further discussed in this paper.) These additional corrections are not experimentally controllable in inclusive measurements, but given their small size one can hope to theoretically treat them in the twist expansion, without resorting to the TMD factorization formalism [38, 39]. A detailed analysis of these issues is left for future work.

In Section VI, we summarize and discuss the many results of our paper and their implications, and in the Appendices we include technical details on process kinematics and the dependence (or rather independence) of our conclusions on the model parameters. In the Appendix section, we also provide a complete discussion of the structure function projectors and their small- x_B limit, as well as an analytic calculation of the small- x_B scaling behaviour of the model structure functions.

II. DIQUARK SPECTATOR MODEL AS A PROXY FOR e + p SCATTERING

Deeply inclusive lepton-nucleon scattering on a proton or neutron target is illustrated in Figure 1, where the incident lepton (with four-momentum momentum l) interacts with a nucleon (p) through the exchange of a virtual photon (q). At large values of the virtuality $Q^2 = -q^{\mu}q_{\mu}$, the virtual photon scatters, on a short time scale, on a quark of four momentum k belonging to the nucleon. In the final state, one measures the recoil lepton momentum l', while the recoiled quark with four momentum k', as well as the remnant X of the proton are unobserved. The remnant is a system of many particles produced by the fragmentation of the target after the photon extracted one of its quarks. The colored quark and remnant are subject to QCD confinement, and, on a much longer time scale compared to the photon-

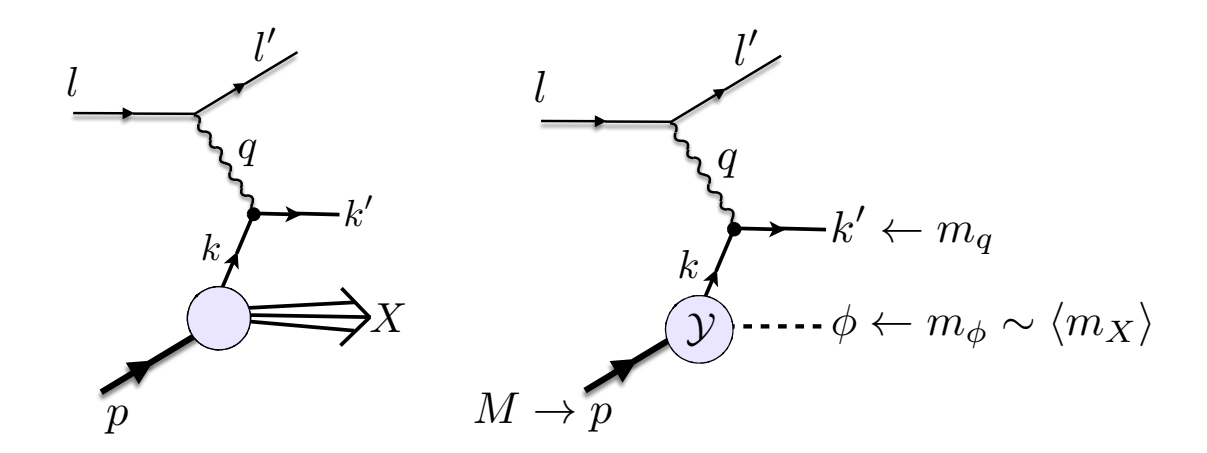


FIG. 1. Electron-proton DIS at leading order in the strong coupling constant. Left: in QCD, where X is remnant of the fragmentation of the target nucleon. Right: in the spectator model, where we replaced the remnant by a scalar diquark ϕ of mass m_{ϕ} , assumed to be of the order of the average remnant mass m_X , and \mathcal{Y} is the model's proton-quark-diquark vertex, with ultraviolet modes cut off by a suitable form factor. The labels indicate the momenta of the particles involved in the collision: q is the momentum of the photon; p is the momentum target nucleon; k and k' are the momenta of the incoming and scattered quark participating in the hard scattering; p_{ϕ} is the momentum of the spectator diquark. M is the mass of the target nucleon, ad m_q the mass of the active quark.

quark scattering process, hadronize into a system of color neutral hadrons. Far from kinematic thresholds, unitarity arguments show that color neutralization can be ignored in an inclusive measurement such as we are discussing, and the process calculated as if quarks where asymptotic states, see the left panel of Figure 1.

Target fragmentation in QCD is a complex, non-perturbative process that cannot be computed exactly, as yet. Instead, we wish to mimic it with a suitable proton-quark-meson vertex in a model theory. To this purpose, we consider a QCD idealized field-theoretical model describing an electrically charged spin 1/2 particle, for instance a proton of mass M, that contains a charged active quark of mass m_q and a neutral scalar diquark spectator, ϕ , of mass m_{ϕ} [27, 28]. In this model the proton's remnant X is mimicked by the spectator ϕ , with m_{ϕ} of the order of the average remnant's invariant mass $\langle m_X \rangle$, and we can simulate e + p collisions by studying the right diagram in Figure 1. For the proton-quark-diquark vertex we choose the following structure:

$$\mathcal{Y} = ig(k^2) \mathbb{1} , \qquad (1)$$

where $g(k^2)$ generically denotes a form factor which takes into account that a diquark is, in fact, a composite field. In this paper, we choose for simplicity the dipolar form factor

$$g(k^2) = g \frac{k^2 - m_q^2}{|k^2 - \Lambda^2|^2} , \qquad (2)$$

where g is a dimensionful coupling constant and Λ a parameter. This vertex is infrared safe, and smoothly cuts off ultraviolet modes in the quark leg when k^2 is much larger than Λ^2 . This is an effective way of simulating confinement in the proton target, since the cutoff imposes a length scale of order $1/\Lambda$. The strong coupling constant g does not play a significant role in our discussion, and we set this to $g = 1 \text{ GeV}^2$ for simplicity. The confinement scale Λ and the spectator mass m_{ϕ} , are considered free parameters of the model, and are meant to capture the salient non-perturbative features of the DIS process. Other possible choices of form factor, including an exponential form and a combination of scalar and axial diquarks to simulate up and down quarks have been discussed in Ref. [27].

The model parameters can be determined by fitting their analytic calculations of parton distribution functions, which are possible in the model due to the relative simplicity of the vertex, to phenomenological extractions from experimental data [1, 4]. Here we adopt the values fitted in Ref. [27] to the PDFs determined by the ZEUS collaboration [40], namely,

$$m_{\phi} = 0.822 \text{ GeV}, \qquad \Lambda = 0.609 \text{ GeV},$$
 (3)

with quark and proton masses kept fixed at

$$m_q = 0.3 \text{ GeV}, \qquad M = 0.939 \text{ GeV}.$$
 (4)

We will use these values as default, but we will also consider variations around these numbers in order to study the systematics of the sub-asymptotic collinear factorization scheme to be discussed later. We also note that with these mass parameters, $m_q + m_\phi > M$ and the proton is a stable particle as it happens in QCD.

In this work, we consider $m_q \neq 0$ in order to study the kinematic dependence of the process on the final state quark mass, and how to retain this in the collinear factorization of the DIS cross section. Similar studies for the inclusive DIS process have been performed in Refs. [17, 32, 33], with a focus on heavy-quark production, and for SIDIS in Refs [15, 16], that analyzed the role of the observed hadron's mass. In all these works, masses are taken into account by a suitable rescaling of the struck quark's momentum light-cone fraction x. In this paper, we revisit the basis for the scaling approximations proposed in the mentioned references, and test these against the full analytic model calculation of the process. As in Ref. [28], we will restrict our analysis to light quarks with mass much smaller than the charm's, $m_q \ll m_c$, and in particular consider values of the order of the strange quark mass, $m_q \sim m_s$.

Lastly, we would like to stress that m_{ϕ} and Λ are "internal", unobservable parameters of the model, in the same way that the QCD confinement scale or the remnant mass cannot be directly measured in real electron-proton scattering. Conversely, even in an inclusive measurement, we treat the quark mass as a known "external" parameter. This is akin to what happens in measurements of the charmed structure function F_2^c in DIS [41, 42], where the active charm quark can be tagged by identifying a heavy flavor hadron in the hadronic final state, without however measuring its momentum, or the momentum of any other hadron. We will come back to this internal/external parameter distinction in Section III, where we discuss the kinematic approximations needed to perform collinear factorization in the model.

A. Calculation of the hadronic tensor

The differential cross section for the inelastic scattering of an unpolarized lepton from an unpolarized nucleon target can be written in the Born approximation as

$$\frac{d\sigma}{dx_B dQ^2} = \frac{\pi \alpha^2 y^2}{Q^6} L_{\mu\nu} \, 2M W^{\mu\nu} \,, \tag{5}$$

where $\alpha = \frac{e^2}{4\pi}$ is the fine structure constant, $Q^2 = -q \cdot q$ is the photon's virtuality, $x_B = Q^2/(2p \cdot q)$ is the Bjorken variable, and the Lorentz invariant y is defined as $y = \frac{p \cdot l}{p \cdot q}$ (here and in the following we use the shorthand $a \cdot b \equiv a^{\mu} b_{\mu}$ for the Lorentz contraction of 2 four-vectors). The leptonic $L_{\mu\nu}$ tensor for unpolarized leptons can be directly computed from QED and reads,

$$L_{\mu\nu}(l,l') = 2(l_{\mu}l'_{\nu} + l_{\nu}l'_{\mu} - l \cdot l'g_{\mu\nu}). \tag{6}$$

The hadronic tensor $W^{\mu\nu}$, on the other hand, is an inclusive tensor containing all the information on the structure of the nucleon target. It is defined by summing the transition matrix elements of the electromagnetic current operator J^{μ} between the initial state nucleon and all possible unobserved final states \mathcal{X} ,

$$2MW^{\mu\nu}(p,q) = \frac{1}{2\pi} \sum_{\mathcal{X}} \int \frac{d^3 \mathbf{p}_{\mathcal{X}}}{(2\pi)^3 2E_{\mathcal{X}}} (2\pi)^4 \delta^{(4)} \left(p + q - p_{\mathcal{X}} \right) \langle N | J^{\mu}(0) | \mathcal{X} \rangle \langle \mathcal{X} | J^{\nu}(0) | N \rangle , \qquad (7)$$

where we have used the shorthand notation $d^3\mathbf{p}_{\mathcal{X}}/(2\pi)^3 2E_{\mathcal{X}} = \prod_{i\in\mathcal{X}} d^3\mathbf{p}_i/(2\pi)^3 2E_i$, with $p_{\mathcal{X}}$ the total momentum of the unobserved hadrons. For a derivation of these formulae, see Ref. [43] and the works cited therein. As opposed to QCD, where the matrix elements in Eq. (7) are of non-perturbative nature and need to be parametrized [43], in the spectator model the nucleon-quark-diquark vertex is explicitly known, see Eqs. (1) and (2), and one can analytically compute the hadronic tensor.

At leading order in the strong coupling constant, the involved diagrams are collected in Figure 2. Note that by electric charge conservation, as stressed in Ref. [28], we need not only to consider the coupling of the photon to the quark, which is expected to dominate at large values of the invariant mass squared $W^2 = (p+q)^2$, but also the photon-proton coupling. The LO cross section is therefore composed of 3 physical process that are observationally indistinguishable but theoretically separable, as we will discuss in the next subsection. The first one is photon-quark scattering, and mimics deeply inelastic scattering on the proton, see Figure 2(a). The second one is the photo-induced excitation of the proton, that subsequently decays into into a quark and a diquark, see Figure 2(c). This is akin to resonance excitation and subsequent decay in QCD, except the model as it stands does not include hadrons of higher mass than the nucleon. Finally, the hadronic tensor also receives a contribution from the interference of these two, see Figure 2(b).

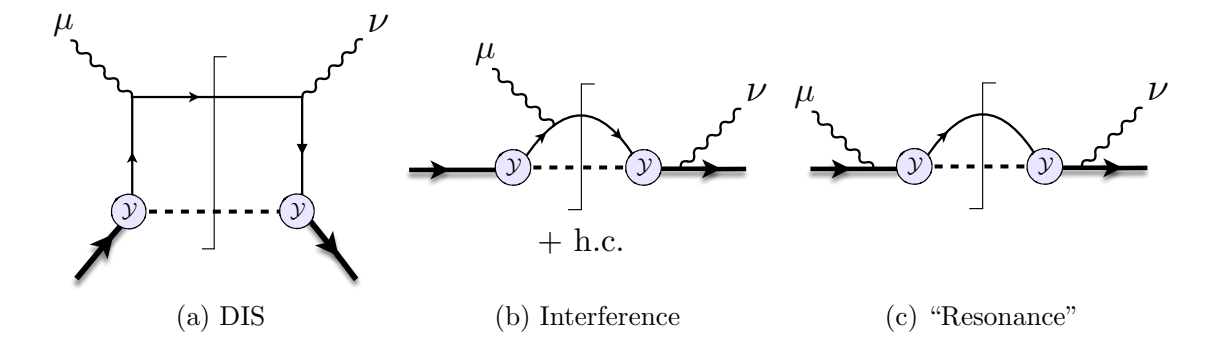


FIG. 2. Diagrams contributing to e + p scattering up to order $O(g^2)$ in the strong coupling constant. Left: DIS contribution. Center: Interference term. Right: Proton resonance.

The hadronic tensor can be written as a sum of these three contributions:

$$W^{\mu\nu} = \sum_{(j)} W^{(j),\mu\nu} = \sum_{(j)} \int_{\Omega_k} d^4k \ \mathcal{W}^{(j),\mu\nu}(k) \qquad (j) = \text{DIS, INT, RES}$$
 (8)

where Ω_k indicates the 4-D integration region in k determined by four-momentum conservation and the external kinematics. The individual, fully unintegrated contribution of each diagram in Figure 2, $W^{(j),\mu\nu}(k)$, can be calculated using the Feynman rules of the model, and at order $O(g^2)$ read:

$$2M\mathcal{W}^{\text{DIS},\mu\nu}(k) = \frac{1}{2} \frac{g^{2}(k^{2})}{(2\pi)^{3}} \frac{\text{Tr}\left[(\not p + M)(\not k + m_{q})\gamma^{\mu}(\not k + \not q + m_{q})\gamma^{\nu}(\not k + m_{q})\right]}{(k^{2} - m_{q}^{2})^{2}} \times \delta((k+q)^{2} - m_{q}^{2})\delta((p-k)^{2} - m_{\phi}^{2}), \tag{9}$$

$$2M\mathcal{W}^{\text{INT},\mu\nu}(k) = \frac{1}{2} \frac{2g^{2}(k^{2})}{(2\pi)^{3}} \frac{\text{Tr}\left[(\not p + M)(\not k + m_{q})\gamma^{\mu}(\not k + \not q + m_{q})(\not p + \not q + M)\gamma^{\nu}\right]}{((p+q)^{2} - M^{2})(k^{2} - m_{q}^{2})} \times \delta((k+q)^{2} - m_{q}^{2})\delta((p-k)^{2} - m_{\phi}^{2}), \tag{10}$$

$$2M\mathcal{W}^{\text{RES},\mu\nu}(k) = \frac{1}{2} \frac{g^{2}(k^{2})}{(2\pi)^{3}} \frac{\text{Tr}\left[(\not p + M)\gamma^{\mu}(\not p + \not q + M)(\not k + \not q + m_{q})(\not p + \not q + M)\gamma^{\nu}\right]}{((p+q)^{2} - M^{2})^{2}} \times \delta((k+q)^{2} - m_{q}^{2})\delta((p-k)^{2} - m_{\phi}^{2}). \tag{11}$$

Note that, following Ref. [28], in the second and third equations we took the liberty to shift the integration variable in order for the δ -functions to match those appearing in the DIS diagram.

We remark from Eq. (10) that the interference term contribution is nominally suppressed by a $1/(W^2 - M^2)$ factor compared to the DIS term (9), due to the presence of one proton propagator. Similarly, the resonance term (11) contains two proton propagators, and is nominally suppressed by one more power of $W^2 - M^2$. As we will demonstrate explicitly in Section II D, this scaling holds to a very good degree for transverse structure functions – hence the DIS term dominates the process at asymptotically large Q^2 or small Bjorken scaling variable $x_B = Q^2/(2p \cdot q)$, where $W^2 \sim Q^2/x_B$. However, this is not the case for the longitudinal structure function, where due to the off-shellness of the quark and proton propagators, all pieces are of similar magnitude and scale with $1/Q^2$.

Finally, it is important to stress that the individual contributions of the 3 diagrams considered in Figure 2 to the hadronic tensor are not gauge invariant by themselves, but their sum (8) satisfies the electromagnetic Ward identities [28]. Since, however, these diagrams contain heuristically distinguishable processes, in the next subsection we propose a method to isolate their gauge invariant part, and obtain a unique and physically meaningful decomposition of the hadronic tensor into a DIS, resonance, and interference contributions. This decomposition is not only of theoretical interest but it will also allow us to test the validity of the collinear factorization procedure, that only purports to approximate the DIS component of the e+p scattering cross section, see Sections III and IV.

B. Gauge invariant decomposition into DIS, resonance, and interference processes

The strategy we follow to uniquely decompose a rank-2 tensor into a gauge invariant and a gauge breaking part is to define a complete set of orthogonal rank-2 projectors, $\{P_{\lambda}^{\mu\nu}\}$, maximizing the number that satisfy the electromagnetic Ward identity, $q \cdot P_{\lambda} \equiv q_{\mu} P_{\lambda}^{\mu\nu} = 0$. Here we limit our treatment to the parity invariant tensors, such as those involved in unpolarized DIS, but will complete the discussion in Appendix A.

Following [17, 44], we define longitudinal, transverse and scalar polarization vectors with respect to a longitudinal momentum p (in our case the proton's momentum) and a reference vector q (in our case the virtual photon's momentum) defining the longitudinal direction and the transverse plane:

$$\varepsilon_0^{\mu}(p,q) = \frac{\hat{p}^{\mu}}{\sqrt{\hat{p}^2}}
\varepsilon_{\pm}^{\mu}(p,q) = \frac{1}{\sqrt{2}}(0, \pm 1, -i, 0)
\varepsilon_q^{\mu}(p,q) = \frac{q^{\mu}}{\sqrt{-q^2}} ,$$
(12)

where $\hat{p}^{\mu} \equiv p^{\mu} - \frac{p \cdot q}{q^2} q^{\mu}$. We note that the transverse ε_{\pm} polarization vectors indeed lie in the plane transverse to both p and q (since $\hat{p} \cdot \varepsilon_{\pm} = q \cdot \varepsilon_{\pm} = 0$) and that the "longitudinal" ε_0 polarization vector is transverse to the photon momentum $(q \cdot \varepsilon_0 = 0)$.

The polarization vectors form an orthogonal basis in Minkowski space,

$$\begin{aligned}
\varepsilon_{\lambda} \cdot \varepsilon_{\lambda'} &= 0 & \text{for } \lambda \neq \lambda' \\
\varepsilon_{\lambda} \cdot \varepsilon_{\lambda} &= 1 & \text{for } \lambda = 0, +, - \\
\varepsilon_{q} \cdot \varepsilon_{q} &= -1 ,
\end{aligned} \tag{13}$$

and can be used to define parity invariant "helicity projectors" for rank 2 tensors. In particular, we define longitudinal, transverse, scalar, and mixed projectors $P_{\lambda}^{\mu\nu}$, with $\lambda=L,T,S,\{LS\}$, as

$$\begin{split} P_{L}^{\mu\nu}(p,q) &= \varepsilon_{0}^{\mu}(p,q)\varepsilon_{0}^{\nu*}(p,q) \\ P_{T}^{\mu\nu}(p,q) &= \varepsilon_{+}^{\mu}(p,q)\varepsilon_{+}^{\nu*}(p,q) + \varepsilon_{-}^{\mu}(p,q)\varepsilon_{-}^{\nu*}(p,q) \\ P_{S}^{\mu\nu}(p,q) &= \varepsilon_{q}^{\mu}(p,q)\varepsilon_{q}^{\nu*}(p,q) \\ P_{\{LS\}}^{\mu\nu}(p,q) &= \varepsilon_{0}^{\mu}(p,q)\varepsilon_{q}^{\nu*}(p,q) + \varepsilon_{q}^{\mu}(p,q)\varepsilon_{0}^{\nu*}(p,q) \; . \end{split} \tag{14}$$

Taking advantage of

$$\varepsilon_{+}^{\mu}(p,q)\varepsilon_{+}^{\nu*}(p,q) + \varepsilon_{-}^{\mu}(p,q)\varepsilon_{-}^{\nu*}(p,q) = -g^{\mu\nu} + \varepsilon_{0}^{\mu}(p,q)\varepsilon_{0}^{\nu*}(p,q) - \varepsilon_{a}^{\mu}(p,q)\varepsilon_{a}^{\nu*}(p,q)$$

$$\tag{15}$$

and of the polarization vectors definition (12), the helicity projectors can be written in a more compact and suggestive way as

$$P_L^{\mu\nu}(p,q) = \frac{\hat{p}^{\mu}\hat{p}^{\nu}}{\hat{p}^2}$$

$$P_T^{\mu\nu}(p,q) = -\hat{g}^{\mu\nu} + \frac{\hat{p}^{\mu}\hat{p}^{\nu}}{\hat{p}^2}$$

$$P_S^{\mu\nu}(p,q) = -\frac{q^{\mu}q^{\nu}}{q^2}$$

$$P_{\{LS\}}^{\mu\nu}(p,q) = \frac{\hat{p}^{\mu}q^{\nu} + q^{\mu}\hat{p}^{\nu}}{\sqrt{-q^2\hat{p}^2}}$$
(16)

where $\hat{g}^{\mu\nu} = g^{\mu\nu} - \frac{q^{\mu}q^{\nu}}{q^2}$ is also transverse to the photon's momentum. In either representation, it is straightforward to verify that these projectors are orthogonal. Indeed,

$$P_{\lambda} \cdot P_{\lambda'} = 0 \qquad \text{for } \lambda \neq \lambda'$$

$$P_{\lambda} \cdot P_{\lambda} = 1 \qquad \text{for } \lambda = L, S$$

$$P_{T} \cdot P_{T} = 2$$

$$P_{\{LS\}} \cdot P_{\{LS\}} = -2$$

$$(17)$$

where we have extended the use of the dot-product symbol to rank-2 tensors: $P_{\lambda} \cdot P_{\lambda'} \equiv P_{\lambda}^{\mu\nu} P_{\lambda',\mu\nu}$. From Eq. (16), it is clear that the 4 defined projectors are also a complete orthogonal basis for symmetric tensors $T^{\mu\nu} = T^{\mu\nu}(p,q)$ that depend on the proton and photon momenta p and q, such as the hadronic tensor for inelastic e + p scattering.

Given a generic symmetric tensor, $T^{\mu\nu} = T^{\mu\nu}(p,q)$, we can now define its helicity structure functions F_{λ} as the projections of the tensor along the helicity basis defined in Eq. (14) or (16):

$$F_{\lambda}(x_B, Q^2) \equiv c_{\lambda} P_{\lambda}(p, q) \cdot T(p, q) \,. \tag{18}$$

with $c_{\lambda}=1/P_{\lambda}\cdot P_{\lambda}$. Thanks to the orthogonality and completeness of the helicity projectors, the tensor T can then be decomposed as $T^{\mu\nu}(p,q)=\sum_{\lambda}F_{\lambda}(x_B,Q^2)P^{\mu\nu}_{\lambda}(p,q)$, One can also go a step further, and separate this into a gauge invariant and gauge breaking components. Indeed, the longitudinal and transverse projectors satisfy the Ward identity,

$$q \cdot P_{L,T} \equiv q_{\mu} P_{L,T}^{\mu\nu} = 0 ,$$
 (19)

and it is immediate to verify that no linear combination of the scalar and mixed projectors can satisfy that, as well. Hence the longitudinal and transverse projectors form a complete orthogonal basis for the space of gauge invariant hadronic tensors. Similarly, the scalar and mixed projectors form a complete orthogonal basis for maximally gauge breaking tensors. As a result,

$$T^{\mu\nu}(p,q) = T^{\mu\nu}_{\text{inv.}}(p,q) + T^{\mu\nu}_{\text{g.b.}}(p,q) ,$$
 (20)

where

$$T_{\text{inv.}}^{\mu\nu}(p,q) = P_T^{\mu\nu} F_T(x_B, Q^2) + P_L^{\mu\nu} F_L(x_B, Q^2)$$
(21)

$$T_{\text{g,b.}}^{\mu\nu}(p,q) = P_S^{\mu\nu} F_S(x_B, Q^2) + P_{\{LS\}}^{\mu\nu} F_{\{LS\}} ,$$
 (22)

are, respectively, the gauge invariant (inv.) and gauge breaking (g.b.) components of the tensor $T^{\mu\nu}$. Accordingly, we also call F_T and F_L "gauge invariant structure functions", and F_S and $F_{\{LS\}}$ "gauge breaking structure functions".

Coming back to our model electron-proton scattering, we can apply this decomposition to each of the 3 processes represented in Figure 3, and define their gauge invariant and gauge breaking parts:

$$2MW_{\text{inv.}}^{(j),\mu\nu}(p,q) = P_T^{\mu\nu} F_T^{(j)}(x_B, Q^2) + P_L^{\mu\nu} F_L^{(j)}(x_B, Q^2), \qquad (23)$$

$$2MW_{g,b}^{(j),\mu\nu}(p,q) = P_S^{\mu\nu} F_S^{(j)}(x_B, Q^2) + P_{\{LS\}}^{\mu\nu} F_{\{LS\}}^{(j)},$$
(24)

for j = DIS, INT, RES. The gauge invariance of the hadronic tensor (8) ensures that the sum of the gauge breaking parts of each diagram in Figure 3 vanishes,

$$W_{\text{g.b}}^{\mu\nu} = \sum_{(j)} W_{\text{g.b}}^{(j),\mu\nu} = 0 \qquad (j) = \text{DIS, INT, RES}$$
 (25)

as one can also explicitly verify utilizing the algebraic manipulations discussed in [28], even though the individual terms in the sum are different from zero.

In summary, the gauge-invariant $F_{T,L}$ structure functions of each individual diagram in Figure 2 are physically meaningful, and allow one to theoretically decompose each e+p scattering structure functions into DIS, resonance and interference contributions. A more detailed discussion of this decomposition in the context of the scalar diquark model will be offered in Sections II D and II E.

C. Kinematics

We parametrize the four-momenta of the proton, photon and incoming quark in Figure 1 in terms of light-cone unit vectors n and \overline{n} , which satisfy $n^2 = \overline{n}^2 = 0$ and $n \cdot \overline{n} = 1$ [34]. The "plus" and "minus" components of a four-vector a^{μ} are defined by $a^+ = a \cdot n = (a^0 + a^z)/\sqrt{2}$ and $a^- = a \cdot \overline{n} = (a^0 - a^z)/\sqrt{2}$. Then, one can decompose

$$a^{\mu} = a^{+} \overline{n}^{\mu} + a^{-} n^{\mu} + a_{T}^{\mu} \equiv (a^{+}, a^{-}, \boldsymbol{a}_{T}), \tag{26}$$

where a_T^{μ} is the vector's transverse four-momentum, which satisfies $a_T \cdot n = a_T \cdot \overline{n} = 0$, with norm $a_T^2 = -a_T^2$, and $a_T \equiv (a_{Tx}, a_{Ty})$ is the 2D Euclidean transverse momentum.

We will work in the "(p,q) frames" class [14], in which the initial proton momentum and virtual photon are collinear in 3-dimensional space and oriented along the z-direction. We can thus decompose

$$p^{\mu} = p^{+} \,\overline{n}^{\mu} + \frac{M^{2}}{2p^{+}} \,n^{\mu},\tag{27}$$

$$q^{\mu} = -\xi p^{+} \,\overline{n}^{\mu} + \frac{Q^{2}}{2\xi p^{+}} \,n^{\mu},\tag{28}$$

$$k^{\mu} = xp^{+} \bar{n}^{\mu} + \frac{k^{2} + k_{T}^{2}}{2xp^{+}} n^{\mu} + k_{T}^{\mu} , \qquad (29)$$

where $x \equiv \frac{k^+}{p^+}$ is the light cone momentum fraction carried by the parton, and ξ is the so-called Nachtmann variable defined as:

$$\xi \equiv -\frac{q^+}{p^+} = \frac{2x_B}{1 + \sqrt{1 + 4x_B^2 M^2/Q^2}} \ . \tag{30}$$

The p^+ component of the nucleon's momentum parametrizes the Lorentz boosts in the z direction, and interpolates between the nucleon rest frame $(p^+ = M/\sqrt{2})$ and the infinite momentum frame $(p^+ \to \infty)$. The use of a light-cone reference frame is justified for hard scattering at large Q^2 , where the proton and scattered quark momenta are dominated by their light-cone plus and minus components, respectively. For the same reason, this is also the frame used to perform collinear factorization, as discussed more extensively in Section III.

Like in e + p scattering in QCD, the Bjorken invariant in the model is bounded, as we discuss in more detail in Appendix C:

$$0 < x_B \le \frac{1}{1 + \frac{(m_\phi + m_q)^2 - M^2}{Q^2}} \equiv x_{B,\text{max}} . \tag{31}$$

The lower bound is due to the fact that in an electron-proton scattering the photon momentum is spacelike. The upper bound, $x_{B,\max}$, is determined by the on-shell condition for particles belonging to a minimal mass 2-particle final state, and is analogous to the "pion threshold" $x_{\pi} = 1/\left[1 + \frac{(M+m_{\pi})^2 - M^2}{Q^2}\right]$ in inelastic e+p collisions in QCD. Likewise, the maximum transverse momentum squared for the scattered quark, $k_{T,\max}^2$, is determined by the available invariant mass W^2 and the masses of the particles in the minimal mass final state, see Appendix C for details:

$$0 \le \mathbf{k}_T^2 \le \frac{\left(W^2 - (m_\phi + m_q)^2\right) \left(W^2 - (m_\phi - m_q)^2\right)}{4W^2} \equiv \mathbf{k}_{T,\text{max}}^2 . \tag{32}$$

It is interesting to note that the kinematic threshold in x_B can be only reached at zero quark transverse momentum. Indeed, solving $k_{T,\text{max}}^2 = 0$ for x_B one recovers the upper limit in (31).

We can now write each of the contributions to the integrated hadronic tensor as

$$W^{(j),\mu\nu}(x_B, Q^2) = \int_0^{\mathbf{k}_{T,\text{max}}^2} d\mathbf{k}_T^2 \iint dx \, dk^2 \, \mathcal{W}^{(j),\mu\nu}(x, k^2, \mathbf{k}_T^2)$$
(33)

where

$$W^{(j),\mu\nu}(x,k^2,\mathbf{k}_T^2) = \frac{\pi}{2x}W^{(j),\mu\nu}(k)$$
(34)

is the fully unintegrated hadronic tensor in the x, k^2 and k_T^2 variables, and the $W^j(k)$ tensors on the right are defined in Eqs. (9)-(11). For simplicity of notation, we distinguish the unintegrated tensors from the integrated tensors only by their arguments. Note that the integral in dk_T^2 appearing in Eq. (33) is limited from above by the maximum transverse momentum squared for the scattered quark defined in Eq. (32).

At LO, due to the δ -functions in the unintegrated hadronic tensors that originate, as mentioned, from the upper and lower cuts in the diagrams of Figure 2, the integrals over dx and dk^2 can be explicitly calculated, and we can define a k_T^2 -unintegrated (but x- and k^- -integrated) hadronic tensor

$$W^{(j),\mu\nu}(\mathbf{k}_T^2) \equiv \frac{\pi}{2x_{\text{ex}}} \frac{1}{|J_{x,k^2,\mathbf{k}_T^2}|} \widetilde{W}^{(j),\mu\nu}(k) \bigg|_{x=x_{\text{ex}}, \ k^2=k_{\text{ex}}^2}, \tag{35}$$

where the Jacobian

$$J_{x,k^2,\mathbf{k}_T^2} = (\xi - 1)\frac{(k^2 + \mathbf{k}_T^2)}{x^2} + \left(1 - \frac{1}{x}\right)\frac{Q^2}{\xi} + \left(1 - \frac{\xi}{x}\right)M^2$$
(36)

arises from the manipulation of the delta functions, and the tilde sign indicates the removal of these from Eqs. (9)-(11). The whole expression (35) is then evaluated at $x = x_{\rm ex}(\mathbf{k}_T^2)$ and $k = k_{\rm ex}^2(\mathbf{k}_T^2)$, which are the solutions of the said delta functions and are explicitly given in Appendix C 3. In Eq. (36) we highlighted the role of the mass scales: beside the external proton mass M^2 and photon virtuality Q^2 , the Jacobian depends on the quark's "light-cone virtuality"

$$v^2 = k^2 + \mathbf{k}_T^2 \tag{37}$$

of the struck quark. The name is justified by noticing that $k^- = v^2/(2k^+)$, so that v^2 quantifies how far the quark momentum is from the light-cone plus direction. As we will discuss, it is this scale, rather than the quark's virtuality k^2 alone, that controls the partonic kinematics in the diagram and determines the applicability of collinear factorization assumptions.

It is now instructive to look in more detail at the internal kinematics of the process. In fact, in an inclusive scattering, the 4-momentum of the scattered quark is not measured, and therefore neither x, nor k^2 , nor k^2 can be experimentally determined. Nonetheless, in the spectator model we do have explicit control over these variables – a major theme of this article – in particular through the analysis of the momentum flow through the cuts in Figure 2. For example, the light-cone fraction x is determined by the the cut of the quark line in the top part of the diagrams, that gives rise to the $\delta((k+q)^2 - m_q^2)$ function in Eqs. (9)-(11). This delta function imposes

$$x = \frac{\xi}{2} \left(1 + \frac{m_q^2 - k^2}{Q^2} + \sqrt{\left(1 + \frac{m_q^2 - k^2}{Q^2} \right)^2 + 4 \frac{k^2 + k_T^2}{Q^2}} \right)$$
(38)

$$= \xi \left(1 + \frac{m_q^2 + \mathbf{k_T}^2}{Q^2} - \frac{v^2 (m_q^2 + \mathbf{k_T}^2)}{Q^4} + O\left(\frac{\mu^6}{Q^6}\right) \right). \tag{39}$$

In the second line, this constraint is expanded in inverse powers of Q^2 and acquires a suggestive form, that in fact holds at any order in the expansion. Indeed in Eq. (39), x depends only on two mass scales: the transverse mass $m_{qT}^2 \equiv m_q^2 + k_T^2$ of the scattered quark and the quark's light-cone virtuality v^2 , with no direct dependence on the diquark mass. The light-cone virtuality is, instead, fixed by the bottom cuts in Figure 2:

$$v^{2} = -\frac{x}{1-x} \left[(m_{\phi}^{2} - M^{2}) + xM^{2} + \mathbf{k}_{T}^{2} \right], \tag{40}$$

see Appendix C 4. Notably, the light-cone virtuality vanishes when $x \to 0$, diverges to negative infinity as $x \to 1$, and is negative over the whole range in x for physical choices of the m_{ϕ} parameter¹. This also means that the quark is off its $k^2 = m_q^2$ mass-shell over the whole range of x_B . This analysis will be substantiated in Section IV, with an explicit calculation of the average values of the internal kinematic variables as a function of Bjorken's x_B .

It is finally important to note that the light-cone virtuality enters Eq. (39) only starting at order $O(1/Q^4)$. Therefore, x and v^2 are coupled essentially only through the quark transverse momentum squared k_T^2 , which is the only variable left free in the loop integrations (9)-(11). Since, as discussed, v^2 remains small except close to the kinematic threshold, where it can become substantially large and negative, truncating Eq. (39) to first order in the $1/Q^2$ expansion appears to be a meaningful approximation over much of the inclusive scattering's (x_B, Q^2) phase space. These considerations will form the basis for the kinematic approximations needed to perform collinear factorization in DIS at subasymptotic energy, as discussed in Section III and numerically tested in Section IV.

D. Transverse structure function

Having discussed the hadronic and partonic kinematics, and isolated the gauge invariant part of the DIS, resonance, and interference diagrams in Figure 2 with the aid of Eqs. (23) and the projections (18), we can study their individual

¹ The only way the light-cone virtuality can become positive and large is if $m_{\phi} \ll M$, such that $v^2 \approx xM^2 - k_T^2/(1-x)$. Evaluating this at $k_T^2 \sim \Lambda^2 \sim 0.4M^2$, the maximum light-cone virtuality remains nonetheless small, only reaching $v_{max}^2 \sim 0.1M^2$ at $x \sim 0.4$ before dropping below 0 as $x \to 1$. This is, however, a quite unphysical choice of diquark mass because ϕ represents the proton's remnant, and thus one would expect $m_{\phi} \sim M$.

role in the e + p scattering process. We focus first on the transverse structure function F_T , which, in our model, gives the dominant contribution to the inelastic cross section, and discuss F_L in the next subsection.

As discussed in Section IIB, the individual DIS, interference and resonance structure functions can be obtained by projecting the respective hadronic tensors:

$$F_T^{(j)} = M P_T^{\mu\nu} W_{\mu\nu}^{(j)}$$
 $(j) = \text{DIS, INT, RES}$. (41)

In the case of the DIS contribution, $F_T^{\rm DIS}$ describes the scattering of a transversely polarized photon with a quark emitted by the proton (see Figure 2(a)). Analogously, the resonance $F_T^{\rm RES}$ structure function describes a transverse photon that scatters on the proton as a whole (see Figure 2(c)). Therefore we expect these structure functions to be non negative:

$$F_T^{\text{DIS}} \propto \left| \mathcal{M}_T^q \right|^2 \ge 0$$
 (42)

$$F_T^{\text{RES}} \propto \left| \mathcal{M}_T^p \right|^2 \ge 0$$
 (43)

where $\mathcal{M}_T^{q,p}$ are the scattering amplitude of the transverse photon-quark and transverse photon-proton processes. This is confirmed in Figure 3, where we numerically evaluate all components of F_T in the spectator model at LO, and show that F_T^{DIS} and F_T^{RES} are indeed positive at all values of x_B and Q^2 . In contrast, the interference structure function F_T^{INT} can have any sign, and in our model it turns out to be negative definite – and not too small, either. In the left panel of Figure 3, we use a value of $Q^2 = 4 \text{ GeV}^2$ and notice that at small x_B the DIS contribution is

In the left panel of Figure 3, we use a value of $Q^2 = 4 \text{ GeV}^2$ and notice that at small x_B the DIS contribution is the dominant one. Nonetheless, the interference piece is large and non negligible even at intermediate and large x_B , and is the main responsible for the visible difference between the DIS curve (blue) and the total contribution (black).

The resonance piece has an extended but small tail at lower x_B , and increases in magnitude as $x_B \to 1$, where in principle it would diverge. However, this divergence is cut off by the phase space, that limits $x_B < x_B^{\rm max} < 1$ when $m_q + m_\phi > M$, as in our model. The interplay of the resonance at $x_B = 1$ and phase space limitations produces an asymmetric bump at $x_B \lesssim x_B^{\rm max}$. This bump becomes visually more prominent and narrow in the total contribution, that seems separated into an inelastic contribution at $x_B \lesssim 0.75$ and a resonance peak at $x_B \gtrsim 0.75$. However, the trough at $x_B \approx 0.75$ is actually a combined effect of the resonance and interference pieces, whose influence extends beyond the edge of phase space, well into what one may consider to be the deep inelastic region. In Figure 4, we show for completeness the calculation for the $m_q + m_\phi < M$ case, where the resonant behavior of the proton excitation is evident.

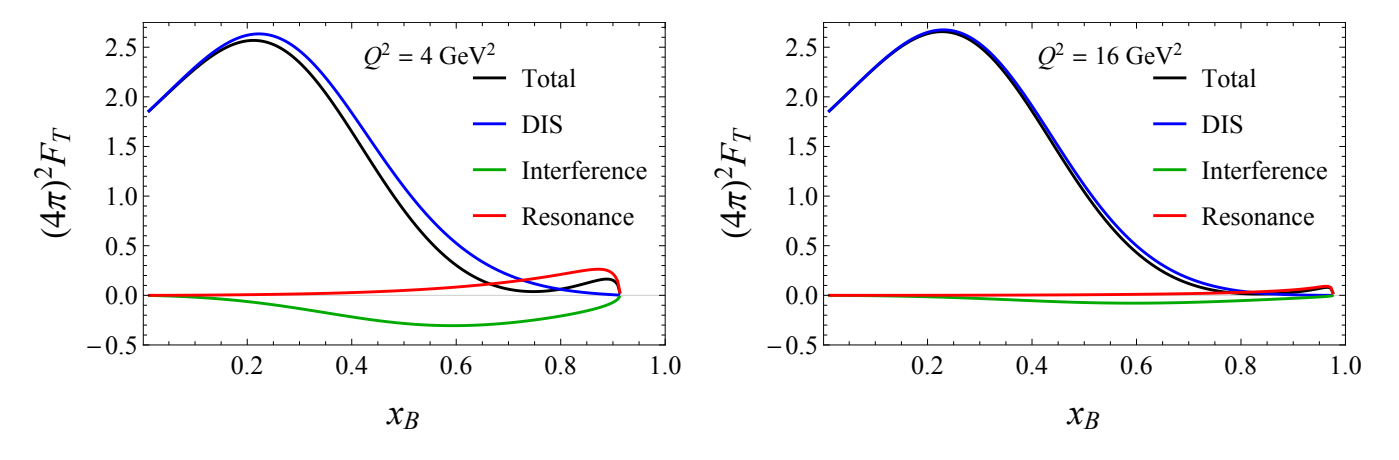


FIG. 3. Gauge invariant decomposition of the transverse structure function F_T at $Q^2 = 4$ GeV² (left plot) and $Q^2 = 16$ GeV² (right plot) for the model parameters specified in Section II [see Eqs. (3)-(4)]. The kinematic thresholds are $x_{B,\text{max}} = 0.913$ and 0.976, respectively.

In e+p scattering, it is important to separate the DIS contribution from the rest, because it is this one that can be factorized into a perturbatively calculable photon-parton hard scattering coefficient and a non-perturbative parton distribution function, thus giving one access to the partonic structure of the target. What the model shows, however, is that the needed phenomenological separation of the DIS piece must be done carefully, and cannot rely only on phenomenological cuts (for example on W^2) to eliminate the apparent resonance "peak". Instead, one needs to also exploit the Q^2 dependence of the structure function, since, as already observed, the interference contribution is parametrically suppressed by a factor $\frac{1}{W^2-M^2} \sim 1/Q^2$ compared to DIS, and the resonance contribution is suppressed

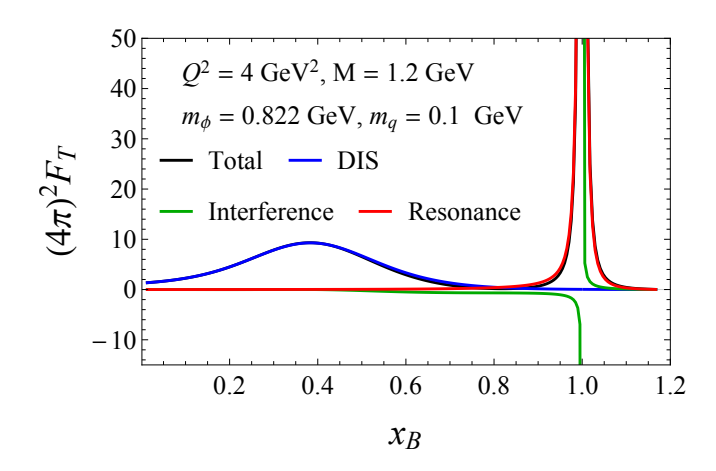


FIG. 4. Same as Figure 3 but for a choice of parameters such that $m_q + m_\phi < M$, which places the kinematic threshold at $x_B = x_{B,\text{max}} = 1.173$. In this case the proton is an unstable particle, and the F_T structure function displays a resonance peak at $x_B = 1$. This corresponds to a $W^2 = M^2$ four momentum squared exchanged in the s channel, see the diagram (c) in Figure 2. An analogous divergence can be seen for the interference contribution, as well.

by $\frac{1}{(W^2-M^2)^2} \sim 1/Q^4$. (In the latter case the parametric scaling does not fully hold numerically, although the resonance piece is still suppressed compared to the resonance contribution, see Appendix B.)

To illustrate the Q^2 suppression of the interference and resonance contributions, we show our calculations for $Q^2 = 16 \text{ GeV}^2$ in the right panel of Figure 3. In this case the interference term contribution is suppressed compared to the plot in the left panel, but still appreciable. The resonance contribution is negligible except at very high x_B values closer to the kinematic threshold, that moved to the right compared to the left panel. There it becomes the dominant contribution, and, combined with the interference, again gives rise to a narrow, but now smaller, "peak". Overall, the DIS piece dominates although a not yet necessarily negligible interference contribution is visible at intermediate x_B . At yet higher Q^2 values the DIS piece would become the dominant contribution over most of the available x_B range, except right before the kinematic threshold.

While an experimental measurement is only sensitive to the full structure function, in the model we can utilize the gauge invariant projectors (16) to explicitly isolate the DIS contribution, as we will do in Section III to confront collinear factorization and study its limitations. Nonetheless, the DIS component can be phenomenologically controlled in a fit that includes power-suppressed $H(x)/Q^2$ terms, with H(x) a suitable polynomial in x, and utilizing data in as large a (x_B, Q^2) range as possible. This was first tried in Ref. [45], and more recently implemented in global fits of parton distributions by the CTEQ-JLab collaboration [46–48] and by Alekhin and collaborators [49, 50]. A similar fit utilizing data generated from the spectator model goes beyond the scope of this paper, but will be presented elsewhere.

E. Longitudinal structure function

The behavior of the longitudinal F_L structure function, illustrated in Figure 5, changes drastically from what we have discussed for its transverse F_T counterpart in at least two respects. Firstly, all 3 components scale approximately as $1/Q^2$, instead of displaying the hierarchy discussed for the transverse case. This also explains why these are typically much smaller than their transverse counterparts (except possibly at the kinematic threshold). Secondly, the total $F_L \to 0$ also as $x_B \to 0$; however, each one of the three components remains different from zero, and, in fact, $F_L^{\rm PIS} \to F_L^{\rm RES}$. We will analytically study the highlighted features of F_L in Appendix B, and instead offer here a heuristic explanation.

For the DIS component, the $1/Q^2$ scaling behavior can be understood noticing that, if the scattered quark was on its mass shell, the Callan-Gross relation would be satisfied and one would find $F_L^{\rm DIS}=0$. However, the quark is virtual, and we can expect the Callan-Gross relation to be broken by an amount proportional to the quark's average virtuality normalized by the scale of the process, which is provided by the invariant mass W^2 : namely, $F_L^{\rm DIS} \propto \langle k^2 \rangle / W^2 \propto \Lambda^2/Q^2$. Note that we have used $\langle k^2 \rangle = O(\Lambda^2)$, because this is the scale that determines the behavior of proton vertex's form factor \mathcal{Y} , and therefore determines the quark's nonperturbative dynamics in the model. In the next section, we will numerically demonstrate this assumption. This argument also justifies the much smaller size of the DIS component of F_L compared to that of F_T . For the resonance piece, the same argument can be applied to the scattered

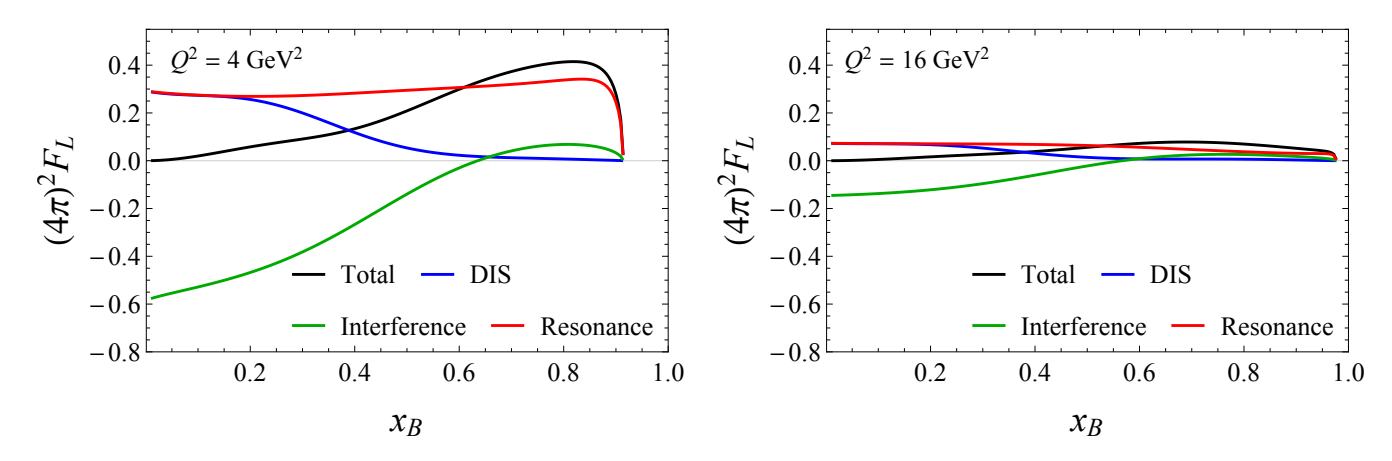


FIG. 5. Gauge invariant decomposition of the longitudinal F_L structure function at $Q^2 = 4 \text{ GeV}^2$ (left) and $Q^2 = 16 \text{ GeV}^2$ (right). The kinematic thresholds are $x_{B,\text{max}} = 0.913$ and 0.976, respectively.

proton, whose virtuality is equal to W^2 by four-momentum conservation. The only scale left to neutralize this is Λ^2 , hence we can expect $F_L^{\rm RES} \propto \frac{1}{W^4} \times \frac{W^2}{\Lambda^2} \propto 1/(\Lambda^2 Q^2)$, where the fourth inverse power of the invariant mass is due to the proton propagator, as evident from Eq. (11). The confinement scale now appears at the denominator, enhancing the resonance piece relative to the DIS contribution (in the transverse case it was much suppressed, instead). The interference piece is a mixture of these two, and we can expect $F_L \propto \frac{1}{W^2} \times \sqrt{\frac{\Lambda^2}{Q^2}} \sqrt{\frac{W^2}{\Lambda^2}} \propto \frac{1}{Q^2}$. In all cases, the three components of the longitudinal structure function scale as $1/Q^2$, as we will analytically corroborate in Appendix B. The limiting behavior of the full F_L , which vanishes as $x_B \to 0$, is a general consequence of gauge invariance. Indeed, one can easily see that the longitudinal projector satisfies

$$P_L^{\mu\nu}(p,q) \xrightarrow[x_B \to 0]{} P_S^{\mu\nu}(p,q)$$
 (44)

Noticing that P_S is one of the two gauge-breaking operators discussed in Section IIB, we obtain

$$F_L \xrightarrow[T_R \to 0]{} 2M P_S \cdot W = 2M P_S \cdot W_{g.b.} = 0 . \tag{45}$$

The last equality is in fact valid for any gauge invariant tensor, see Eq. (25), and therefore also for inelastic scattering at LO in our model, as plotted in Figure 5. Unitarity then imposes specific small- x_B constraints for the resonance and interference components of F_L :

$$F_L^{\text{RES}} \xrightarrow[TR \to 0]{} F_L^{\text{DIS}}$$
, (46)

$$F_L^{\text{RES}} \xrightarrow[x_B \to 0]{} F_L^{\text{DIS}} , \qquad (46)$$

$$F_L^{\text{INT}} \xrightarrow[x_B \to 0]{} -2F_L^{\text{DIS}} . \qquad (47)$$

Indeed, since the two individual e+p scattering amplitudes involving the longitudinal photon-quark and the longitudinal photon-proton interactions are imaginary, $\mathcal{M}_L^{q,p}=iT_{q,p}$, the vanishing of F_L in that limit imposes $T_q^2+T_p^2-2T_qT_p=1$ $(T_q - T_p)^2 \to 0$. Let us stress that Eqs. (45)-(47), are consequence of electromagnetic gauge invariance rather than special features of the model we have considered. What is not constrained by general principles is the limiting behavior of the DIS contribution, that at small x_B could as well tend to zero or diverge (in which case, we note that the interference term should also diverge but with opposite sign). The fact that it is, instead finite, is a feature of the chosen spectator model, as we will analytically demonstrate in Appendix B, where we will also prove the common $1/Q^2$ scaling behavior.

In closing this section, we recall that the spectator model we are considering is only designed to account for the quark dynamics inside the proton, and therefore can only mimic electron-proton scattering in the "valence quark region" at large $x_B \gtrsim 0.2$. In QCD, the DIS longitudinal structure function at small x_B is instead dominated by photon-gluon fusion interactions, that the model as it stands cannot describe². Nonetheless, the conclusion that

² A generalization of the model to include gluon dynamics has been discussed in Ref. [51].

 $F_L \to 0$ as $x_B \to 0$ is a consequence of electromagnetic gauge invariance, and as such is model independent. Therefore we can also expect this to happen in nature. In fact, data on inelastic e+p scattering gathered at HERA [52–54] show that F_L first grows as x_B decreases towards $x_B \sim 10^{-4}$, then falls off as x_B becomes smaller than that value, contrary to expectations from perturbation theory. Many explanations have been advanced for this observation, including higher twist effects [31, 50, 55–57] and deviations from DGLAP evolution [58–61]. Here, we are suggesting that a further source of deviation from perturbative calculations of F_L is due to the limiting behavior of this structure function, that is forced by gauge symmetry to vanish at small x_B .

III. COLLINEAR FACTORIZATION AT SUB-ASYMPTOTIC MOMENTUM TRANSFER

We now wish to factorize the DIS component of the model hadronic tensor in terms of a quark distribution function q(x), and a perturbatively calculable photon-quark hard scattering term $\mathcal{H}^{\mu\nu}$. To our knowledge, factorization of the resonance and interference diagrams either in a model or in QCD, has not yet been discussed in literature and will not be pursued here. Note that our discussion differs from the treatment of factorization for the QCD hadronic tensor essentially only in the absence of strong interaction Wilson lines. These would eventually drop out of the definition of collinear PDFs in the light-cone gauge, and do not affect the arguments put forward in this Section, which is largely concerned with improvements in the treatment of the internal partonic kinematics.

Working at LO in the coupling constant, we consider the handbag diagram shown in Figure 6, where we have included the customary quark correlator $\Phi(p,k)$ in the bottom part [39], and an "inclusive quark jet correlator" $\Xi(k')$ in the top part [62–64]. In the context of collinear factorization, the quark jet correlator was already used in Ref [28, 44, 65] in order to correctly handle the external, hadron-level kinematic constraints in the DIS endpoint region, while allowing one to perform the parton-level momentum approximations needed to prove the factorizability of the DIS hadronic tensor. As a field theoretical object in its own right, the quark jet correlator has also been recently studied in Refs. [62, 63], where it was used to derive a complete set of fragmentation function sum rules and to provide a new way to study the dynamical breaking of chiral symmetry in QCD. In our derivation of factorization, we will incorporate insights from that analysis. In fact, using the jet correlator, we will be able to weaken the needed approximations on the quark's transverse momentum compared to other collinear factorization derivations [28, 39].

Note that the diagrams represented in Figure 6 only include a subclass of all possible diagrams, in which the final state in the current direction does not interact with the target remnant. Considering this subclass of diagrams is justified at large enough values of the Bjorken variable x_B , which is the focus of this paper, because the final state invariant mass $W^2 = (1 - 1/x_B)Q^2 + M^2$ kinematically limits the transverse momentum of particle produced in the quark's direction, squeezing these in a jet-like configuration aligned with the quark's momentum [66, 67]. One can then write the hadronic tensor Eq. (7) as

$$2MW^{\mu\nu} = (2\pi)^3 \int d^4k \ d^4k' \ \text{Tr} \big[\Phi(p,k) \, \gamma^{\mu} \, \Xi(k') \gamma^{\nu} \big] \ \delta^{(4)}(k+q-k') \,, \tag{48}$$

where the δ -function encodes 4-momentum conservation in the photon quark hard-scattering vertex, indicated by red circles in Figure 6, and the factor $(2\pi)^3$ in front of the integral comes from the phase space over the momentum of the Y blob. Following Ref. [63], the quark distribution correlator Φ is defined as

$$\Phi(p,k) = \operatorname{Disc} \int \frac{d^4 \xi}{(2\pi)^4} e^{ik\cdot\xi} \langle N(p)|\bar{\psi}(0)\psi(\xi)|N(p)\rangle , \qquad (49)$$

where ψ is the quark field operator and $|N(p)\rangle$ single nucleon state with momentum p. The quark-to-jet correlator $\Xi(k')$ is analogously defined as

$$\Xi(k') = \operatorname{Disc} \int \frac{d^4 \eta}{(2\pi)^4} e^{ik' \cdot \eta} \langle \Omega | \psi(\eta) \overline{\psi}(0) | \Omega \rangle , \qquad (50)$$

where $|\Omega\rangle$ is the interacting vacuum state, and can be interpreted as the discontinuity of the quark propagator [62, 63]. Note that the model is not a gauge theory, hence, at variance with the QCD case, we do not need to consider Wilson lines in the definition of either Φ or Ξ .

A. Derivation

In order to obtain a factorized expression for the DIS hadronic tensor, usually one approximates the incoming partonic momentum k to be collinear in 3D with the nucleon target and immediately takes advantage of the four

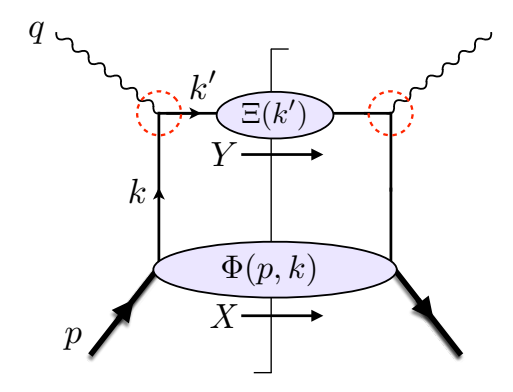


FIG. 6. Leading order inclusive DIS scattering handbag diagram, including a jet correlator in the top part. The red circles indicate the hard scattering vertex, where kinematic approximations will be performed (see Section III A for details).

momentum conservation δ -function to integrate out the recoiled quark momentum k'. In contrast to this, we will treat k' as an "internal" variable as is actually done for SIDIS. The momentum k' can be parametrized in terms of light-cone unit vectors as

$$k'^{\mu} = \left(\frac{k'^2 + \mathbf{k}_T'^2}{2k'^-}, k'^-, \mathbf{k}_T'\right). \tag{51}$$

We now approximate the scattering and recoiled k and k' quark momenta appearing in the in the 4-momentum conservation δ -function. Namely, we take

$$\delta^{(4)}(k+q-k') \simeq \delta^{(4)}(\widetilde{k}+q-\widetilde{k'}), \tag{52}$$

with \widetilde{k} and $\widetilde{k'}$ defined as,

$$k^{\mu} \approx \widetilde{k}^{\mu} = \left(xp^{+}, \frac{\overline{v}^{2}}{2xp^{+}}, \mathbf{k_{T}}\right) \tag{53}$$

$$k^{\prime \mu} \approx \widetilde{k}^{\prime \mu} = \left(\frac{\overline{v}^{\prime 2}}{2k^{\prime -}}, k^{\prime -}, \mathbf{k}_{T}^{\prime}\right). \tag{54}$$

The approximate light cone \bar{v}^2 and \bar{v}'^2 virtualities ideally chosen such that such that $\bar{v}^2 \approx \langle k^2 + k_T^2 \rangle$ and $\bar{v}'^2 \approx \langle k'^2 + k_T'^2 \rangle$. Note, that we are approximating only the sub-leading momentum components of the scattering and recoiled partonic momenta, but fully retain their respective transverse components. In this respect, we depart from the treatment of Refs [28, 39], and do not need further kinematic assumptions.

In the approximated delta function (52), the light-cone k^+ and k'^- momentum components decouple,

$$\delta^{(4)}(\widetilde{k} + q - \widetilde{k'}) = \delta^{(2)}(\mathbf{k_T} - \mathbf{k'_T}) \,\delta\left(k^+ + q^+ - \frac{\overline{v'}^2}{2k'^-}\right) \delta\left(\frac{\overline{v}^2}{2k^+} + q^- - k'^-\right) \tag{55}$$

and the integrations over dk^- and dk'^+ in Eq. (48) can act directly on $\Phi(k)$ and $\Xi(k')$. Therefore, by defining the integrated quark correlator as

$$\Phi(x, \mathbf{k_T}) \equiv \int dk^- \Phi(k) \tag{56}$$

and the TMD inclusive jet correlator [62] as

$$J(k'^{-}, \mathbf{k'_T}) \equiv \frac{1}{2} \int dk'^{+} \Xi(k'), \tag{57}$$

we can write the hadronic tensor as

$$2MW^{\mu\nu} = 2(2\pi)^{3} \int dx \, dk'^{-} \delta\left(x - \xi - \frac{\bar{v}'^{2}}{2p^{+}k'^{-}}\right) \delta\left(\frac{\bar{v}^{2}}{2xp^{+}} + q^{-} - k'^{-}\right) \int d^{2}\mathbf{k_{T}} \operatorname{Tr}\left[\Phi(x, \mathbf{k_{T}}) \gamma^{\mu} J(k'^{-}, \mathbf{k_{T}}) \gamma^{\nu}\right]$$
(58)

Note that the integral over dk^+ was rewritten in term in terms of dx, and that the integration over $d^2k'_T$ fixes $k'_T = k_T$. The remaining d^2k_T transverse momentum integration acts only over the trace term, and the plusand minus-direction delta functions fix the values of the light cone fraction x and of the dominant k'^- component of the recoiled quark momentum, respectively.

Our next step is to introduce the "operational" twist expansion [68] for the integrated correlators, $\Phi(x, \mathbf{k_T})$ and $J(k'^-, \mathbf{k_T'})$. This expansion is predicated on the existence of a hard scale determining a large boost in the light cone direction such that the scattering quark momentum component satisfy $k^+ \gg |\mathbf{k_T}| \gg k^-$, and for the recoiled momentum $k'^- \gg |\mathbf{k_T'}| \gg k'^+$. In DIS, such a scale is provided by the photon's virtuality Q^2 , and one can consider $P^+ \sim k'^- \sim Q$. The quark correlator can then be expressed as a power expansion in M/P^+ , where the power counting scale M can be identified with the proton mass [38]. Limiting ourselves to the unpolarized sector, we write

$$\Phi(x, \boldsymbol{k_T}) = \frac{1}{2} q(x, \boldsymbol{k_T}^2) \, / \!\!\!/ + \frac{M}{2P^+} \left[e(x, \boldsymbol{k_T}^2) \, \mathbb{I} + q^{\perp}(x, \boldsymbol{k_T}^2) \, / \!\!\!/ M \right] + O\left(\frac{M^2}{(P^+)^2}\right)$$

$$(59)$$

where $q(x, \mathbf{k_T}^2)$ is the unpolarized parton distribution function, while $e(x, \mathbf{k_T}^2)$ and $q^{\perp}(x, \mathbf{k_T}^2)$ are twist-3 level parton distributions. For the TMD inclusive jet correlator, the power counting scale can be identified with the "confinement" scale Λ of the model (it would be $\Lambda_{\rm QCD}$ in QCD) and the correlator expanded in powers of k'^-/Λ [62, 67]:

$$J(k'^{-}, \mathbf{k'_{T}}) = \frac{1}{2}\alpha(k'^{-})\hbar + \frac{\Lambda}{2k'^{-}} \left[\zeta(k'^{-}) \mathbb{I} + \alpha(k'^{-}) \frac{k'_{T}}{\Lambda} \right] + O\left(\frac{\Lambda^{2}}{(k'^{-})^{2}}\right).$$
 (60)

Note that the leading twist coefficient $\alpha(k'^-) = \frac{1}{2(2\pi)^3}$ is the analog of the unpolarized D_1 fragmentation function in SIDIS [38]. The chiral-odd twist-3 coefficient $\zeta(k'^-) = \frac{1}{2(2\pi)^3} M_j/\Lambda$ describes perturbative and non-perturbative "jet mass" contributions [63, 67] and is the analog of the chiral-odd fragmentation function E [38].

We can now expand the trace appearing in Eq. (58), which reads:

$$2(2\pi)^{3} \int d^{2}\mathbf{k_{T}} \operatorname{Tr}\left[\Phi(x,\mathbf{k_{T}}) \gamma^{\mu} J(k'^{-},\mathbf{k_{T}}) \gamma^{\nu}\right]$$

$$= \int d^{2}\mathbf{k_{T}} \left[\frac{1}{4}q(x,\mathbf{k_{T}}^{2}) \operatorname{Tr}\left[\vec{n}\gamma^{\mu} \dot{n}\gamma^{\nu}\right] + \frac{M\Lambda}{4P^{+}k'^{-}} \left(\frac{M_{j}}{\Lambda} e(x,\mathbf{k_{T}}^{2}) \operatorname{Tr}\left[\gamma^{\mu}\gamma^{\nu}\right] + q^{\perp}(x,\mathbf{k_{T}}^{2}) \operatorname{Tr}\left[k_{T}^{\mu}\gamma^{\mu} k_{T}^{\nu}\gamma^{\nu}\right]\right)\right]$$

$$= \underbrace{\frac{1}{4}q(x) \operatorname{Tr}\left[\vec{n}\gamma^{\mu} \dot{n}\gamma^{\nu}\right]}_{\text{twist 2}} + \underbrace{\frac{M\Lambda}{P^{+}k'^{-}}}_{\text{twist 4}} \underbrace{\left(\frac{M_{j}}{\Lambda} e(x)g^{\mu\nu} + \frac{1}{4}\int d^{2}\mathbf{k_{T}} q^{\perp}(x,\mathbf{k_{T}}^{2}) \operatorname{Tr}\left[k_{T}^{\mu}\gamma^{\mu} k_{T}^{\nu}\gamma^{\nu}\right]\right)}_{\text{twist 4}} + \operatorname{HT} . \tag{61}$$

At leading twist, the integration over $d^2\mathbf{k}_T$ only acts on the parton distribution, and produces the 1D, collinear PDF

$$q(x) \equiv \int d^2 \mathbf{k_T} \, q(x, \mathbf{k_T^2}) \ . \tag{62}$$

At twist-4, we find a contribution from the collinear $e(x) \equiv \int d^2 \mathbf{k_T} e(x, \mathbf{k_T}^2)$ distribution, as well as from the first $\mathbf{k_T}^2$ moment of the $q^{\perp}(x, \mathbf{k_T}^2)$ distribution. One can thus explicitly see that the dynamics of the parton transverse momentum is not neglected in this approach, but rather included in twist-4 terms. A full treatment of these, however, also requires consideration of 4-parton matrix elements [34, 69, 70] and is left for future work. Note also that the approach we have followed here is not entirely new. In fact it closely corresponds to the treatment of SIDIS cross sections in terms of transverse-momentum-dependent PDFs [38, 43], and a detailed correspondence can be obtained through the use of the fragmentation function sum rules developed in [62, 63, 71]. The SIDIS formalism is, however, at present fully developed only up to twist-3 level.

Limiting ourselves to the leading-twist (LT) contribution in Eq. (61), the hadronic tensor can be written as a convolution of a hard scattering tensor $\mathcal{H}^{\mu\nu}$ and the collinear PDF q(x),

$$2MW^{\mu\nu}\big|_{LT} = \int \frac{dx}{x} \mathcal{H}^{\mu\nu}(x,\bar{x}) q(x) \tag{63}$$

with

$$\mathcal{H}^{\mu\nu}(x,\bar{x}) = \frac{1}{4} x \,\delta(x-\bar{x}) \operatorname{Tr}\left[\bar{n}\gamma^{\mu} \,\dot{n}\gamma^{\nu}\right] \frac{1}{|J_{x,k'}|} \tag{64}$$

In this equation, \bar{x} arises from the manipulation of the delta function appearing in Eq. (58),

$$\bar{x} = \frac{\xi}{2} \left(1 + \frac{\bar{v}'^2 - \bar{v}^2}{Q^2} + \sqrt{\left(1 + \frac{\bar{v}'^2 - \bar{v}^2}{Q^2} \right)^2 + 4\frac{\bar{v}^2}{Q^2}} \right)$$
 (65)

$$= \xi \left(1 + \frac{\bar{v}'^2}{Q^2} - \frac{\bar{v}^2 \bar{v}'^2}{Q^4} + O\left(\frac{\mu^6}{Q^6}\right) \right) , \tag{66}$$

and depends on two mass scales, namely, the approximate incoming and outgoing light cone parton virtualities \bar{v}^2 and \bar{v}'^2 , collectively denoted by μ^2 . Note that the incoming parton's virtuality \bar{v}^2 only contributes at $O(1/Q^4)$, and can be parametrically neglected. The Jacobian factor $J_{x,k'^-} = 1 - \frac{\bar{v}^2 \bar{v}'^2}{4(xp^+k'^-)^2}$ arises from manipulation of the mentioned delta functions. More explicitly, this reads

$$\frac{1}{J_{x,k'^-}} = 1 + \frac{\bar{v}^2 \bar{v}'^2}{Q^4} \left(\frac{1}{(\frac{x}{\xi} + \frac{\bar{v}^2}{Q^2})^2 - \frac{\bar{v}^2 \bar{v}'^2}{Q^4}} \right) , \tag{67}$$

and deviates from 1 by a term scaling as the fourth inverse power of Q. Using $\bar{v}'^2 \approx m_q^2 + \langle \mathbf{k}_T^2 \rangle \sim O(m_q^2)$ one finds $J_{x,k'^-} = 1 + O(\frac{m_q^2 \bar{v}^2}{Q^4})$. Hence, the choice of virtualities will play a secondary role in J_{x,k'^-} compared to the determination of \bar{x} . We will come back to these kinematic considerations in Section IV A.

Finally, the factorized transverse structure function F_T^{CF} can be calculated by contracting the factorized hadronic tensor (63) with the transverse projector P_T defined in Eq. (16). One finds

$$F_T^{\text{CF}}(x_B, Q^2) = q(\bar{x}), \tag{68}$$

which at LO is proportional to the quark PDF evaluated at the \bar{x} variable, that replaces x_B as scaling variable away from the Bjorken limit. Working analogously with the P_L projector, the longitudinal structure function vanishes at LO:

$$F_L^{\text{CF}} = 0 \ . \tag{69}$$

B. Discussion

The hard scattering tensor (64) satisfies by inspection the Ward Identity $q_{\mu}\mathcal{H}^{\mu\nu}=0$, independently of the values of \bar{v}^2 and \bar{v}'^2 . We have thus found in Eq. (63) a gauge invariant generalization of the conventional collinear factorization procedure for the hadronic tensor (48), which is valid for scattering and scattered partons of any virtuality. With this added flexibility, in Section IV we will study a range of choices for \bar{v}^2 and \bar{v}'^2 in order to maximally extend the range of validity of the LT collinear factorization procedure towards large x_B and low Q^2 values.

Clearly, Eq. (64) reduces to the parton model result for light quarks in the $\bar{v}^2 \to 0$ and $\bar{v}'^2 \to 0$ limit, in which the partons are taken to approximately travel on the light cone. But even then, the quarks need not be approximately on their $k^2 \approx k'^2 \approx m_q^2 \approx 0$ mass shell, as often stated in literature, unless one further assumes - with no need - that the quarks are real particles. Outside of this limit, a gauge invariant factorized hadronic tensor can only be obtained if one considers the jet diagram in Figure 6. Had we worked in the parton model from the outset, or even in QCD but with a perturbative quark line instead of a jet correlator in the top part of the handbag diagram of Figure 6, this would not have been possible.

Despite its simplicity, formula (64) is non-trivial and it is worthwhile summarizing under what conditions it has been obtained. First of all, we emphasize once more that the transverse momentum is not approximated but rather included in higher-order terms in the twist expansion, which provides a controlled dynamical approximation. In fact, using the quark field's equation of motion relations, one can show that the twist-3 PDF e can be decomposed as $xe = x \tilde{e} + \frac{m_q}{M}q$, where \tilde{e} correspond to a "pure" twist-3 dynamical contribution [38]. Similarly, the jet mass can be decomposed as $M_j = m_q + m^{\text{corr}}$, where m^{corr} is the dynamical mass of the jet [62, 63]. Thus the twist expansion (61) does not only provide an expansion in the transverse momentum effects, but also in the quark mass contributions. The latter is appropriate as long as the quarks are light enough, otherwise one might want to include the term proportional to m_q^2 in the LT partonic tensor.

The only uncontrolled approximation we have performed is a purely kinematic one. Namely, we have fixed the value of the quark light-cone virtualities v and v', such that the sub-dominant momentum components are approximated by $k^+ \approx \bar{v}^2/2k^+$ and $k'^- \approx \bar{v}'^2/2k'^+$. But, crucially, this approximation is only taken inside the overall parton-level

4-momentum conservation delta function, which is part of the "hard scattering" graphically identified by red circles in Figure 6. Thus, following the philosophy of [39], we have confined the only needed non-controlled approximation to the hard interaction and kept the parton momenta otherwise unapproximated. The price to be paid for this approximation – which is the minimal kinematic approximation compatible with collinear factorization! – is that transverse momentum conservation in the approximated hadronic tensor is effectively broken, and this sets an inescapable limit to the validity of the CF formula at large x_B [28]. We will numerically study this limit for the spectator model in Section V B.

IV. TESTING THE KINEMATIC APPROXIMATIONS

In deriving the factorized hadronic tensor (63) in the previous Section, we have distinguished dynamical and kinematical approximations, namely, the inclusion of the parton transverse momentum loop integral contribution into the twist expansion, and the choice of approximate light cone virtualities \bar{v}^2 and \bar{v}'^2 entering the calculation of the collinear hard scattering tensor $\mathcal{H}^{\mu\nu}$.

The twist expansion is controlled by powers of μ^2/Q^2 and can be calculated up to any desired order (although each order eventually needs the introduction of one or more new non-perturbative functions). The light cone virtualities, instead, are not observable and cannot be experimentally controlled: a physically or theoretically motivated Ansatz is needed to choose suitable \bar{v}^2 and \bar{v}'^2 values, but without an extrinsic way of controlling the validity of one's choice or of improving on the ensuing approximation. In the spectator model, however, one has full control of the unobserved (or "internal") variables, and one's choices can be in fact verified by studying the value of the average internal variables vs. the approximated ones. Furthermore, in the model one can not only calculate the hard-scattering term, but also the PDFs themselves. Hence one can perform a detailed comparison of the factorized vs. full cross section and structure functions.

In this Section, we will explore and validate a number of kinematical approximations by studying suitably defined averages of the internal variables. The range of validity of the collinear factorization approximation of the transverse DIS structure functions will be explored in Section V.

A. Kinematic approximations

In the full DIS process represented in Figure 2(a) we can identify external variables such as Q^2 , the Bjorken-invariant x_B , the target mass M, or the final state quark mass m_q , which are experimentally observable. We can also identify internal variables, such as the parton's light-come momentum fraction x, its intrinsic transverse momentum k_T^2 and its light-cone virtuality $v^2 = k^2 + k_T^2$, which cannot be experimentally accessed with an inclusive measurement. We then need to carefully choose the approximate \bar{x} scaling variable, and the \bar{v}^2 parton light-cone virtuality that enter the collinear factorization formula (63)-(64).

Looking at Eq. (66), the light-cone fraction $\bar{x} = \xi(1 + \bar{v}'^2/Q^2 - \bar{v}^2\bar{v}'^2/Q^4) + O(\mu^6/Q^6)$ depends on \bar{v}^2 only starting at order $O(\mu^4/Q^4)$ and can be approximated in first instance as $\bar{x} \approx \xi\left(1 + \frac{\bar{v}'^2}{Q^2}\right)$. This is equivalent to choosing

$$\bar{v}^2 = 0 \tag{70}$$

in Eq. (66). As one can expect from Eq. (40) and we will numerically confirm below, this is in fact a good approximation for v^2 at not too large values of x_B , and as long as one considers small enough quark masses. It is also the approximation taken in the parton model, and in conventional derivations of collinear factorization.

We now turn to the scattered quark approximate light-cone virtuality, $\bar{v}'^2 \approx \langle k'^2 + k_T'^2 \rangle$. The quark passes the cut in the LO diagram in Figure 2 as well as in Figure 6 as part of the jet diagram. Hence, its virtuality k'^2 must be at least as large as m_q^2 , and since we do not measure its transverse momentum in an inclusive process we can only choose

$$\bar{v}^{\,\prime\,2} = m_q^2 \ . ag{71}$$

This is the minimum value that v'^2 can take, and in fact this choice remains valid at any perturbative order, see Appendix C 5.

Differently from the scattered quark, the incoming quark is a virtual particle and its light-cone virtuality is determined by the scattering dynamics. In fact, as we shall shortly demonstrate numerically, this quark is typically off its mass shell: at small values of x_B its virtuality is $\langle k^2 \rangle \approx -\langle k_T^2 \rangle$, and this becomes increasingly negative as x_B grows closer to its kinematic threshold.

With the light-cone virtuality choices (70) and (71), one obtains

$$\bar{x} \approx \xi \left(1 + \frac{m_q^2}{Q^2} \right) \equiv \xi_q \ , \tag{72}$$

which is in fact analogous to the χ scaling variable used in Ref. [17, 33] to study charm production in charged current $W+s\to c$ events. With a non-zero \bar{v}'^2 like in Eq. (71) we are more closely respecting the internal kinematics of the handbag diagram than with $\bar{v}'^2=0$. Therefore, we can expect that $\bar{x}=\xi_q$ to provide a better approximation to the non-factorized diagram's than in conventional collinear factorization.

At large values of x_B , closer to the kinematic threshold, the virtuality (40) diverges to minus infinity, and a different approximation may be needed. As discussed in detail in Appendix C4, a suitable approximation to the model's v^2 that is valid in both the small- x_B and large- x_B regimes is

$$\bar{v}^2(\bar{x}) = -\frac{\bar{x}}{1-\bar{x}} \left(m_\phi^2 + (\bar{x}-1)M^2 \right),$$
 (73)

and an analogous approximation for QCD can be obtained by replacing $m_{\phi}^2 \rightsquigarrow M^2$ in the above equation. Substituting Eq. (73) in Eq. (66), solving the resulting equation for \bar{x} perturbatively in powers of μ^2/Q^2 , and finally setting $\bar{v}'^2 = m_q^2$ as in Eq. (71), we find

$$\bar{x} \approx \xi \left[1 + \frac{m_q^2}{Q^2} + \frac{\xi}{1 - \xi} \frac{m_q^2 (m_\phi^2 + (\xi - 1)M^2)}{Q^4} \right] \equiv \xi_q^*$$
 (74)

up to corrections of $O\left(\frac{\mu^6}{Q^6}\right)$. Note that at small x_B the fourth order term quickly vanishes, and one recovers Eq. (72). Closer to the kinematic threshold, this new scaling variables accounts for the non-vanishing of the scattered quark's light-cone virtuality. Substituting this back in Eq. (73) we can also write the corresponding virtuality purely in terms of external variables:

$$\bar{v}_*^2 \equiv \bar{v}^2(\xi_q^*) \ . \tag{75}$$

Non-zero virtualities have also been studied in Ref. [72], where the target is assumed to be a composite system of generic subsystems. Here we shall consider their role in the kinematics of the handbag diagram.

B. Average internal variables

The kinematic Ansätze just discussed for the internal variables x and v^2 , that cannot be directly measured in inclusive processes, can be compared to their $\langle v^2 \rangle$ and $\langle x \rangle$ values, which are calculable in the model. Likewise, we can explore the size of $\langle k_T^2 \rangle$ and estimate the effects of neglecting it in the determination of \bar{x} , \bar{v}^2 , and \bar{v}'^2 .

Let us then define the average of a generic function $\mathcal{O} = \mathcal{O}(x, k^2, \mathbf{k_T^2})$ of the internal variables as:

$$\langle \mathcal{O} \rangle (x_B, Q^2) = \frac{\int_0^{\mathbf{k_{T,\text{max}}}} d\mathbf{k_T}^2 dk^2 dx \, \mathcal{O}(x, k^2, \mathbf{k_T}^2) \mathcal{F}_T^{\text{DIS}}(x, k^2, \mathbf{k_T}^2)_{x_B, Q^2}}{\int_0^{\mathbf{k_{T,\text{max}}}} d\mathbf{k_T}^2 dk^2 dx \, \mathcal{F}_T^{\text{DIS}}(x, k^2, \mathbf{k_T}^2)_{x_B, Q^2}},$$
(76)

where $k_{T,\text{max}}^2$ was defined in Eq. (32), and the fully unintegrated structure function $\mathcal{F}_T^{\text{DIS}}$ is defined as the transverse projection of the fully unintegrated DIS hadronic tensor (9):

$$\mathcal{F}_T^{\text{DIS}}(x, k^2, \mathbf{k}_T^2)_{x_B, Q^2} = M P_T^{\mu\nu} \mathcal{W}_{\mu\nu}^{\text{DIS}}(x, k^2, \mathbf{k}_T^2)_{x_B, Q^2}.$$
 (77)

The dependence of $\langle \mathcal{O} \rangle$ on x_B and Q^2 is due to the hard scattering delta function inside \mathcal{F}_T , and is symbolically denoted in the subscript following the functional dependence on the internal variables. The denominator at the right hand side of Eq. (76) is easily recognized as the DIS transverse function F_T^{DIS} .

C. Numerical validation

In order to numerically study the validity of the kinematic approximations discussed in Section IV A, we will consider the sequence of \bar{x} scaling variables summarized in Table I. Starting with Eq. (72), that is by neglecting the

\bar{x}	M	m_q	\bar{v}^{2}	$oldsymbol{k_T}^2$
x_B	0	0	0	0
ξ	✓	0	0	0
ξ_q	✓	\checkmark	0	0
ξ_q^*	✓	\checkmark	\bar{v}_{*}^{2}	0
ξ_{qT}^*	√	✓	\bar{v}_{*T}^{2}	$\overline{\langle oldsymbol{k_T}^2 angle}$

TABLE I. Sequence of kinematic approximations considered for the validation of the approximations and scaling variables \bar{x} discussed in Section IV A. A check mark indicates the inclusion of M or m_q in \bar{x} , and the approximation to the internal v^2 and \mathbf{k}_T^2 variables is indicated in the last two columns. (The \bar{v}_*^2 and \bar{v}_{*T}^2 approximated light-cone virtualities are defined in Eqs. (75) and (79), repectively.) Below the thin horizontal line, we collected approximations that can only be considered in the spectator model, where the dynamics of the internal degrees of freedom is explicitly known, but not in QCD.

scattered quark virtuality as well as all external mass scales (i.e., $M=0,m_q=0$), we then consecutively switch on the target mass and the quark mass. Finally, we consider the parton virtuality effects captured in Eq. (74). These scaling variable are suitable for collinear factorization of inclusive scattering processes. By necessity, however, they neglect the kinematic effect of the internal transverse momentum, because no particles other than the scattered lepton is measured in the final state, so that no measured scale is available to control the size of $\langle k_T^2 \rangle$. Nonetheless, Eq. (39), shows that k_T^2 contributes to the scaling variables at the same order as m_q^2 , and it would be desirable to estimate the size of its contribution.

An estimate of the average transverse momentum squared is actually possible in the model, where $\langle \boldsymbol{k_T^2} \rangle$ can be explicitly calculated using Eq. (76). The result is presented in Figure 7 as a function of x_B at several values of Q^2 . The upper left panel utilizes the default model parameter choices discussed in Section II, and the other two panels increase, respectively, the values of the target mass and the quark mass³. A comprehensive study of the systematic dependence on the model parameters is presented in Appendix D. As one can expect, $\langle \boldsymbol{k_T^2} \rangle = O(\Lambda^2)$ is of non perturbative origin and determined by the "confinement" scale Λ , with a mild dependence on the model parameters (see also Figure 14). The average transverse momentum squared is independent of the scattering kinematics at small x_B , then decreases at large x_B , where four momentum conservation limits the amount of invariant energy in the final state and forces this to vanish: $\langle \boldsymbol{k_T^2} \rangle \to 0$ as $x_B \to x_B^{\text{max}}$ (see Appendix C for more detail). Leveraging the detailed calculations in Appendix C we can then define theoretical, transverse-momentum-improved scaling variables simply by substituting $m_q^2 \leadsto m_q^2 + \langle \boldsymbol{k_T^2} \rangle$ and $m_\phi^2 + (x-1)M^2 \leadsto m_\phi^2 + (x-1)M^2 + \langle \boldsymbol{k_T^2} \rangle$ in Eqs. (74) and (75), and define:

$$\xi_{qT}^* \equiv \xi \left(1 + \frac{m_q^2 + \langle \mathbf{k}_T^2 \rangle}{Q^2} + \frac{\xi}{1 - \xi} \frac{\left(m_q^2 + \langle \mathbf{k}_T^2 \rangle \right) \left(m_\phi^2 + (\xi - 1)M^2 + \langle \mathbf{k}_T^2 \rangle \right)}{Q^4} \right)$$
(78)

$$\bar{v}_{*T}^2 \equiv v^2(\xi_{qT}^*) ,$$
 (79)

With these we will estimate the importance of including in the calculation the transverse momentum dynamics, that is neglected in collinear factorization if one limits the analysis to leading twist level.

We then look at the average light-cone virtuality $\langle v^2 \rangle = \langle k^2 + k_T^2 \rangle$, shown as a black line in Figure 8 and compared to the 3 choices of approximated \bar{v}^2 defined in Eqs. (70), (75) and (79). At small x_B , all vanish and the parton can be effectively considered collinear to the nucleon in the plus light-cone direction. As x_B increases, however, the light cone virtuality becomes more and more negative until the kinematic threshold $x_{B,\max}$ is reached. The only exception occurs at larger target mass values, for which a modest rise with x_B is followed again by a fast dive as x_B approaches its threshold. This behavior was already expected from the analysis of Eq. (40) offered in Section II C. The deviation of $\langle v^2 \rangle$ from $\bar{v}^2 = 0$ is qualitatively captured by \bar{v}_*^2 , and the remaining small gap is closed if the transverse momentum is taken into account by including the calculated, but unobserved, $\langle k_T^2 \rangle$ into \bar{v}_{*T}^2 .

It is worthwhile remarking that the plots in Figs. 7-8, combined, also clearly show that the incoming quark virtuality $\langle k^2 \rangle = \langle v^2 \rangle - \langle k_T^2 \rangle$ is negative and of order $O(\Lambda^2)$ at all x_B values: the quark is indeed a bound state of the proton. Clearly, the $k^2 \approx 0$ approximation utilized in many parton model calculations and derivation of factorization formulas is wrong, and should rather be replaced, by $v^2 \approx 0$, unless one is interested in extreme values of x_B where \bar{v}_*^2 better describes the parton's light-cone virtuality.

³ This layout will be used also when studying other internal variables in this Section, and for the study of factorized vs. full structure function in Section V.

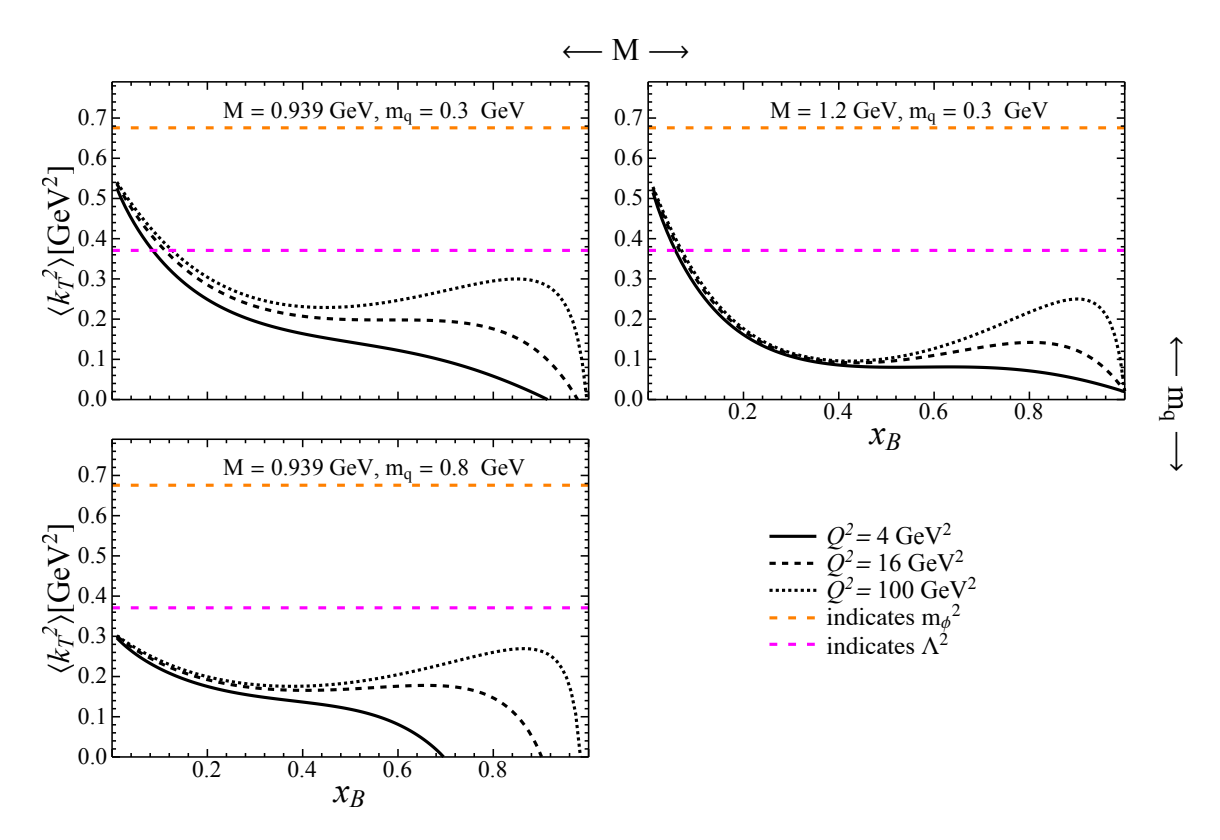


FIG. 7. Average unobserved k_T^2 of the incoming quark calculated in the full model as a function of x_B at various Q^2 values and for different values of the model parameters M and m_q . For scale comparison, the orange dashed line indicates the model's value of m_{ϕ}^2 , while the magenta dashed line indicates the model's value of Λ^2 , see Eq. (3).

The average light-cone fraction $\langle x \rangle$ is another important internal variable that can be calculated in the model but only indirectly controlled experimentally by measuring the Bjorken invariant x_B . The comparison to the 5 approximations listed in Table I is performed for clarity by plotting the corresponding $\bar{x}/\langle x \rangle$ ratios as a function of x_B in Figure 9, where the same choice of kinematics and model parameters as in the average light-cone virtuality just discussed was adopted. One can immediately see that the standard massless collinear approximation $x = x_B$ (blue line) very poorly approximates the parton's fractional momentum x, and results in a $\bar{x}/\langle x \rangle$ ratio that is very sensitive to the model parameters. While this is not a problem at small x_B , where a small shift in the x value at which the PDFs are calculated does not significantly alter the cross section, this can lead to significant under- or over-estimation of the structure functions at larger x_B . On the contrary, keeping into account the target's mass inside the $\bar{x} = \xi$ scaling variable stabilizes the large x_B approximation, but the new scaling variable can still significantly underestimate $\langle x \rangle$, especially if the quark is heavy, see the green line. This is remedied by including the quark mass inside $\bar{x} = \xi_q$ (red line), which produces a good approximation for the model parameter values considered in Figure 9. In fact, the approximation degrades for higher values of the "confinement" scale Λ or the spectator mass m_{ϕ} , see Appendix D. The latter case is important particularly meaningful because, in reality, the proton's remnant after the hard scattering is a multi-particle state with a distribution in invariant mass not fully captured by $m_{\phi} \sim \langle m_X \rangle$. Finally, one can consider the effects of a non-vanishing virtuality \bar{v}_*^2 , which however are suppressed by $1/Q^4$ and do not improve much the approximation, see the purple line compared to the red one.

In summary, there seems indeed to be a limit to what any experimentally controllable inclusive DIS kinematic approximation to $\langle x \rangle$ can achieve. However, as it was the case for $\langle v^2 \rangle$, if one was able to control the partonic k_T^2 accessed in the hard scattering reaction, the approximation would become nearly perfect, as the orange dashed lines representing $\xi_{qT}^*/\langle x \rangle$ shows. At the end of this Section, we will briefly discuss how this could in fact be achieved, either by utilizing the TMD factorization formalism, or including HT terms in the collinear calculation.

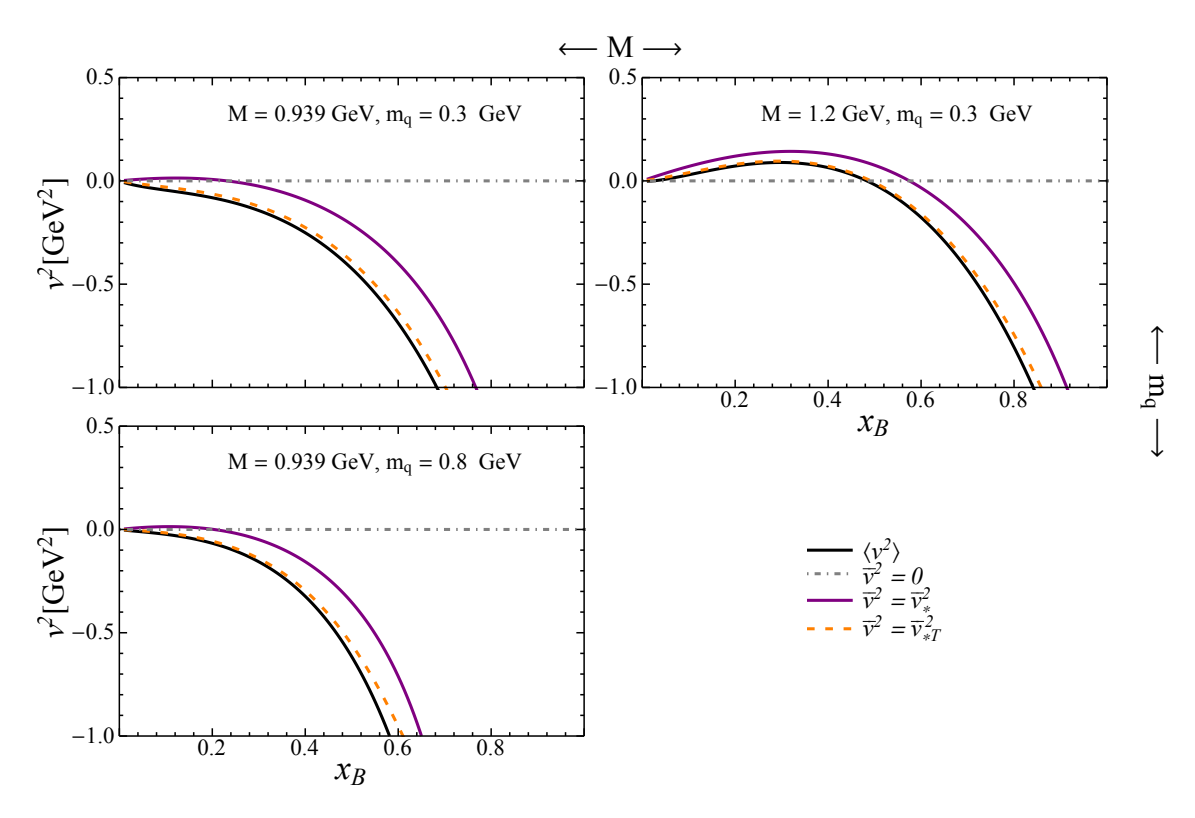


FIG. 8. Average light cone virtuality $v^2 = k^2 + k_T^2$ calculated in the full model for $Q^2 = 4 \text{ GeV}^2$, compared to the \bar{v}^2 approximations discussed in the text. In the top left panel, the default model parameters are used, and the other panels show the effect of increasing, respectively, M and m_q .

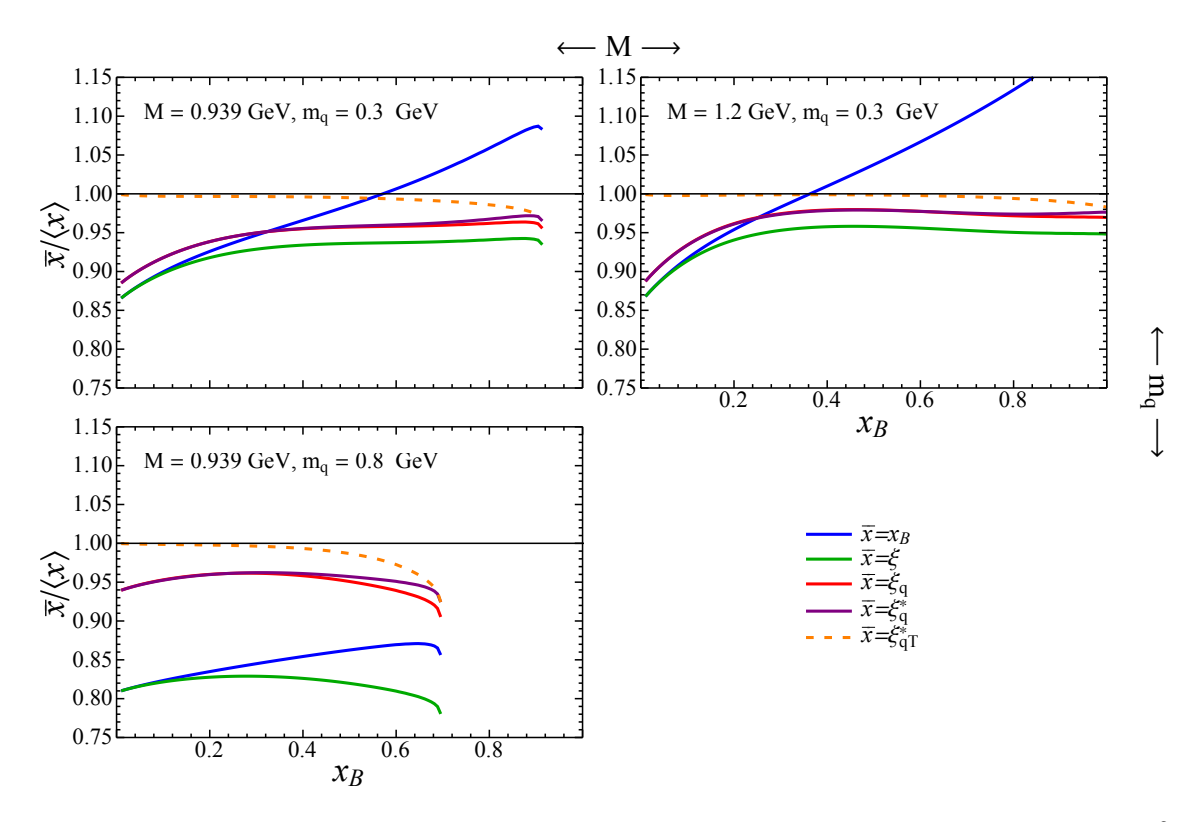


FIG. 9. Ratio of approximated \bar{x} parton light-cone momentum fraction to the full $\langle x \rangle$ calculated in the model at $Q^2=4~{\rm GeV}^2$. In the top left panel, the default model parameters are used, and the other panels show the effect of increasing, respectively, M and m_q .

V. TESTING THE LIMITS OF FACTORIZATION

The calculation of the transverse F_T^{DIS} structure function (68) requires knowledge of the quark PDF q(x). In QCD, this is a non-perturbative quantity and needs to be extracted from the data. However, in the model one can also explicitly calculate q(x) (see also Refs [27, 73]). From the definition (59), we find

$$q(x) = \int d^{2}\mathbf{k_{T}} dk^{-} \operatorname{Tr} \left[\frac{\gamma^{+}}{2} \Phi(p, k) \right]_{k^{+} = xp^{+}} = \int \frac{d^{2}\mathbf{k_{T}} dk^{-}}{(2\pi)^{4}} \operatorname{Tr} \left[\begin{array}{c} \gamma^{+} \\ 2 \end{array} \right]_{k^{+} = xp^{+}}$$
(80)

and applying the Feynman rules to write the contribution of the diagram inside the trace, we obtain

$$q(x) = \int \frac{d^2 \mathbf{k_T} \, dk^-}{(2\pi)^4} g^2(k^2) \frac{1}{2} \frac{\text{Tr}\left[(\not p + M)(\not k + m_q)\frac{\gamma^+}{2}(\not k + m_q)\right]}{(k^2 - m_q^2)^2} (2\pi) \, \delta((p - k)^2 - m_\phi^2)$$
(81)

$$= \frac{1}{4(2\pi)^2} \int d\mathbf{k}_T^2 dk^- g^2(k^2) \frac{\text{Tr}\left[(\not p + M)(\not k + m_q)\frac{\gamma^+}{2}(\not k + m_q)\right]}{(k^2 - m_q^2)^2} \delta((p - k)^2 - m_\phi^2)$$
(82)

$$=\frac{g^2}{(2\pi)^2} \frac{\left[2(m_q + xM)^2 + L^2(\Lambda^2)\right](1-x)^3}{24L^6(\Lambda^2)},\tag{83}$$

where

$$L^{2}(\Lambda^{2}) = xm_{\phi}^{2} + (1-x)\Lambda^{2} - x(1-x)M^{2}.$$
(84)

In the model, we can therefore test the validity of the proposed generalized collinear factorization by comparing the factorized and full calculations of the DIS structure functions. By also comparing k_T -unintegrated structure functions, we will furthermore be able to numerically explore the conditions for the breakdown of this approximation.

A. Validity of the factorization approximations

We first study to what degree collinear factorization provides a good approximation of the DIS process in the model by comparing the full F_T^{DIS} calculated as in Eq.(41) with the factorized F_T^{CF} (68) calculated with the model PDF (83). (The longitudinal structure function identically vanishes at LO, and an analogous test would require one to extend the model calculation to NLO, which goes beyond the scope of this article.)

We do this first in Figure 10, where $F_T^{\rm DIS}$ is plotted as a black line, and various factorized $F_T^{\rm CF}$ structure functions computed at $Q^2=4~{\rm GeV^2}$ with the scaling variables collected in Table I are represented by colored lines. We adopt the same choice of model parameters as in the study of the internal kinematics performed in Section IV C, and present a more detailed study of model parameter variations in Appendix D. One can immediately notice that the same pattern observed in Section IV C. First, the asymptotic kinematic choice $x=x_B$ (blue line) is very unstable with respect to the model parameters – something already observed in Ref. [28] for k_T -dependent structure functions. Second, taking into account mass corrections by using the $\bar{x}=\xi_q$ or $\bar{x}=\xi_q^*$ scaling variables provides a much better and more stable approximation of $F_T^{\rm DIS}$. Finally, the k_T^2 corrections theoretically estimated with $\bar{x}=\xi_{qT}^*$ (but not controllable experimentally) explain most of the remaining differences. One can also see that none of the factorized cross section does respect the kinematic $x_B \leq x_{B,\rm max}$ bound (unless one was working strictly in the Bjorken $Q^2 \to \infty$ limit), which is a first illustration of the fact that the adopted factorization approximation breaks 4-momentum conservation, as already remarked in Section III.

The hierarchy of approximations just discussed can be better appreciated in Figure 11, where we show the ratio of the F_T^{CF} collinear structure functions to their exact F_T^{DIS} counterpart. The fact that $F_T^{\text{CF}}|_{\bar{x}=x_B}$ does not approximate F_T^{DIS} in any accurate way, can be traced to the failure of x_B to approximate the average partonic momentum fraction $\langle x \rangle$. For example looking at the blue line in Figure 11(a), where the default model parameters are utilized, we see that the CF structure function overestimates the exact DIS calculation at small x_B , then suddenly drops and underestimates it even down to the $\sim 50\%$ level before surging again closer to the kinematic threshold. This behavior can be understood from Figure 9(a), where the choice $\bar{x}=x_B$ first underestimates the average $\langle x \rangle$ at $x_B \lesssim 0.6$ then overestimates it at $x_B \gtrsim 0.6$, right around the value where $F_T^{\text{CF}}|_{\bar{x}=x_B}$ becomes smaller than F_T^{DIS} . This clearly highlights the need of a more accurate kinematic approximation, which is indeed reached by fully taking into account

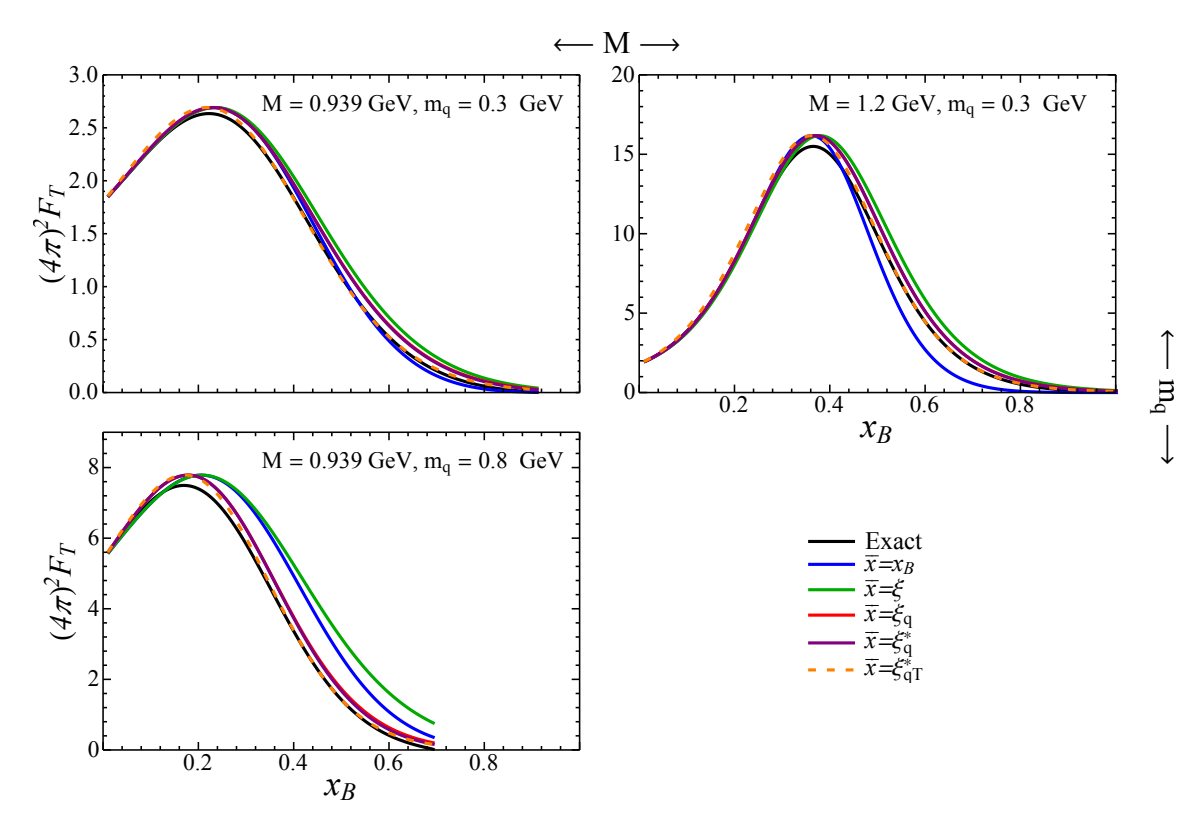


FIG. 10. Transverse F_T structure function calculated in the model at $Q^2 = 4 \text{ GeV}^2$ compared to a generalized collinear factorization calculation utilizing the kinematic approximations listed in Table I. In the top left panel, the default model parameters are used, and the other panels show the effect of increasing, respectively, M and m_q .

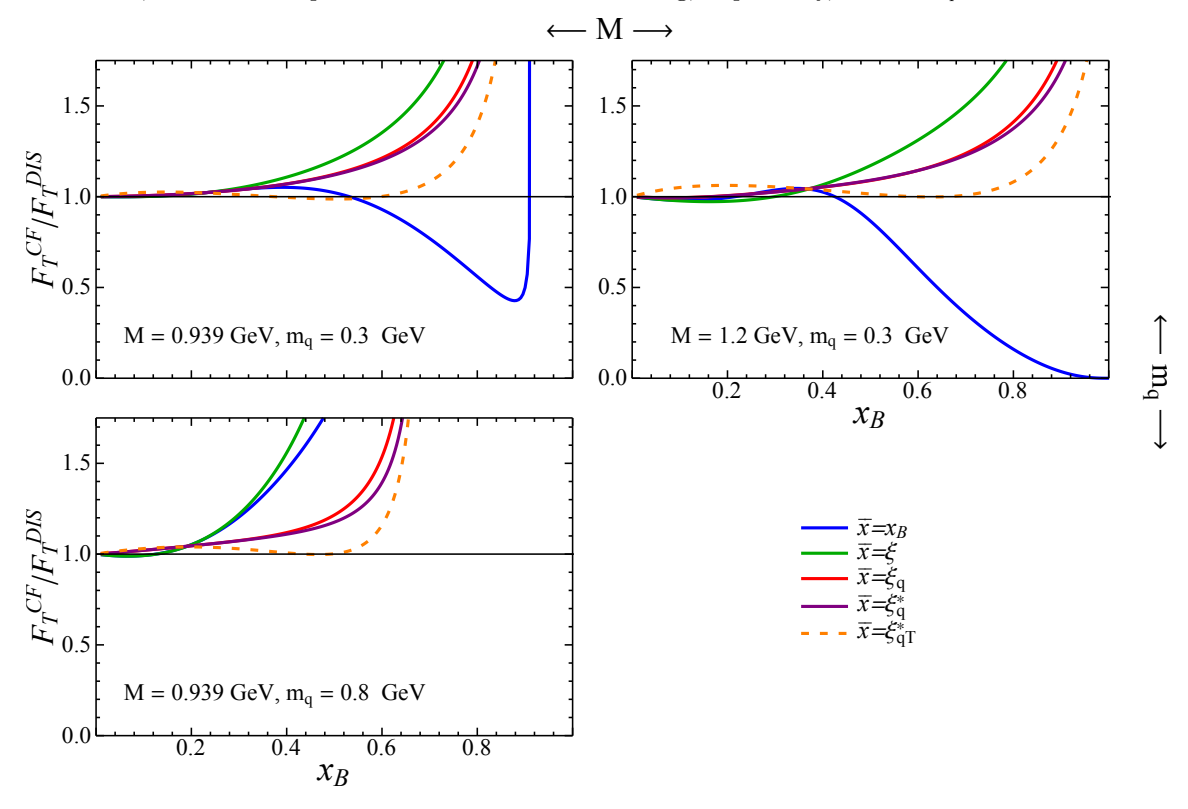


FIG. 11. Ratio of the factorized to exact DIS transverse structure functions presented in Figure 10.

the target and quark masses in $\bar{x} = \xi_q$. The order $O(1/Q^4)$ corrections included in $\bar{x} = \xi_q^*$ do not qualitatively improve the agreement of F_T^{CF} with F_T^{DIS} , unless the final state quark is much heavier than the strange quark.

In summary, it is clear that the use of the $\bar{x} = \xi_q$ scaling variable effectively provides the closest F_T^{CF} approximation to the real one, and extends the kinematic range of validity of CF to the largest x_B value that can be achieved considering only external variables. The validity of CF is naturally extended at larger Q^2 , where mass effects are suppressed by an inverse of power of the photon virtuality and become sizable only in an increasingly narrow region close to the kinematic threshold, see Figure 12.

As observed many times, however, the CF cross section at leading twist misses the transverse momentum effects, which are parametrically of the same order of magnitude as the mass effects successfully incorporated in ξ_q . The "missing" k_T^2 corrections can be nonetheless estimated by choosing $\bar{x} = \xi_q^*$, and are shown as a dashed orange line in Figures 11 and 12. The exact calculation is largely reproduced in this way, showing that maximizing the range of validity of a factorized calculation requires control over transverse-motion-induced power corrections. Even though these are beyond the scope of our leading twist calculation, one can handle their contribution to the cross section either by extending collinear factorization to higher-twist [34, 70], or by utilizing a TMD formalism where these are taken into account at parton distribution level [38, 39]. We will discuss this point more extensively at the end of this Section.

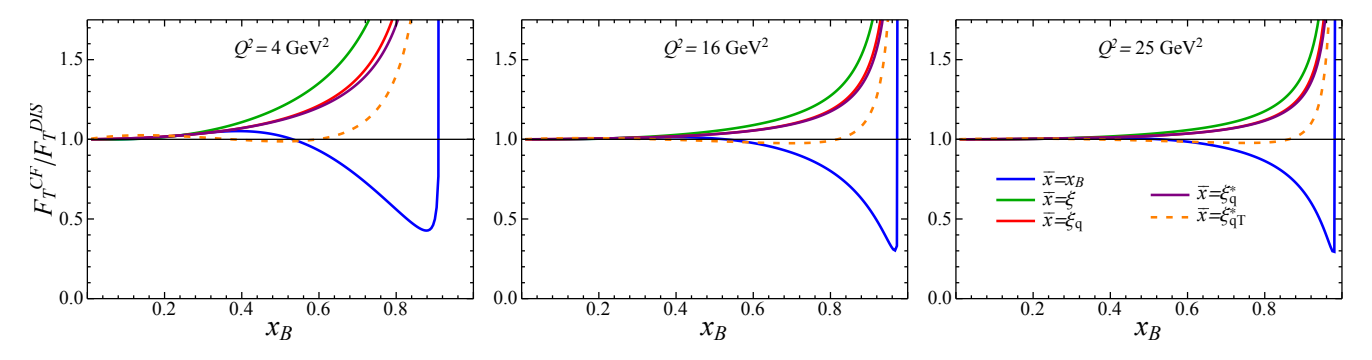


FIG. 12. Ratio of the factorized to exact DIS structure functions calculated in the model for several Q^2 values, and the default model parameters. The generalized collinear factorization calculation was performed utilizing the kinematic approximations listed in Table I.

B. Breaking of Collinear Factorization

Even after considering transverse momentum contributions, one can notice in Figures 11 and 12 that the ratio $F_T^{\text{CF}}/F_T^{\text{DIS}}$ strongly deviates from 1 at a Bjorken momentum fraction x_B larger than a scale-dependent, "factorization breaking" threshold $x_{B,\text{break}} = x_{B,\text{break}}(Q^2)$. Defining breaking of factorization as a $\sim 10\%$ deviation of the CF structure function from the exactly calculated one, we obtain the values of $x_{B,\text{break}}$ collected in Table II, where we also indicate the corresponding value of W^2 in parentheses, denoted by W^2_{break} . A more complete study of the parameter systematics can be found in Appendix D.

Phenomenologically, one can notice that the dependence of $x_{B,\text{break}}$ on Q^2 and on the model parameters, both internal and external, is largely determined by that of $x_{B,\text{max}}$, derived in Appendix C:

$$x_{B,\text{max}} = \frac{1}{1 + \frac{(m_{\phi} + m_q)^2 - M^2}{O^2}} \ . \tag{85}$$

Indeed, the larger the target mass M the higher the x_B value where factorization breaks down, and the larger the quark mass m_q (or indeed the remnant's m_{ϕ}) the smaller the breaking threshold. We can thus see that breaking of factorization is mostly a kinematic effect, and occurs when the process is too close to the edge of phase space. As a rule of thumb, we can see that this happens when

$$W^2 \lesssim 4 \text{ GeV}^2 , \qquad (86)$$

with the quoted numerical value being a slight overestimate of the worst case combination of parameters shown here or in Appendix D. Even if the obtained numerical values depends on the chosen spectator model, the parameters of latter have been chosen to reproduce the PDFs phenomenologically extracted in QCD by means of global fits, and

			$Q^2 = 4 \text{ GeV}^2$		$Q^2 = 16 \text{ GeV}^2$			$Q^2 = 25 \text{ GeV}^2$ $x_{B,\text{break}} \ W_{\text{break}}^2 \ [\text{GeV}^2] \ R_{\text{break}}$		
$M [{ m GeV}]$	m_q [GeV]	$x_{B,\text{break}}$	$W_{\text{break}}^2 \text{ [GeV}^2\text{]}$	$R_{\rm break}$	$x_{B,\text{break}}$	$W_{\text{break}}^2 \text{ [GeV}^2\text{]}$	$R_{\rm break}$	$x_{B,\text{break}}$	$W_{\text{break}}^2 \text{ [GeV}^2\text{]}$	$R_{\rm break}$
0.94	0.3 0.3 0.8	0.72	(2.4)	0.29	0.89	(2.9)	0.29	0.92	(3.1)	0.27
1.2	0.3	0.82	(2.4) (2.3)	0.21						
0.94	0.8	0.59	(3.7)	0.24						

TABLE II. Factorization breaking thresholds $x_{B,\text{break}}$, (in parentheses) the corresponding values of invariant mass W_{break}^2 and R_{break} [see. Eq (92)] for the choices of target mass M and quark mass m_q discussed in the main text.

thus we can take the model to be a fair proxy for the latter. This makes us hopeful that the region of applicability of collinear factorization may be controlled at least in first approximation by a simple kinematic cuts even in QCD (and in that case, it looks like one would simply need to neglect the hadron resonance region, which is anyway removed from global QCD fits).

Theoretically, the breaking of factorization can be traced back to the violation of momentum conservation in the kinematic approximations (53)–(54), and in particular to the lack of transverse momentum conservation in the factorized diagram [28]. To see this explicitly, let us define k_T -unintegrated DIS structure function

$$\mathcal{F}_T^{\text{DIS}}(\boldsymbol{k_T}^2) \equiv \iint dx \, dk^2 \, \mathcal{F}_T^{\text{DIS}}(x, k^2, \boldsymbol{k_T}^2)_{x_B, Q^2} , \qquad (87)$$

where the fully unintegrated DIS structure function appearing in the integrand was defined in Eqs. (77) as the $P_T^{\mu\nu}W_{\mu\nu}^{\rm DIS}(k)$ projection of the fully unintegrated DIS hadronic tensor. Similarly, we can define the k_T -unintegrated CF structure function as

$$\mathcal{F}_{T}^{\text{CF}}(x, k^{2}, \boldsymbol{k}_{T}^{2})_{x_{B}, Q^{2}} \equiv M P_{T}^{\mu\nu} \mathcal{W}_{\mu\nu}^{\text{CF}}(x, k^{2}, \boldsymbol{k}_{T}^{2})_{x_{B}, Q^{2}},$$
(88)

with the fully unintegrated collinearly factorized hadronic tensor defined as

$$2M\mathcal{W}_{\mu\nu}^{CF}(x,k^2,k_T^2)_{x_B,Q^2} \equiv \frac{\pi}{2x} \frac{1}{2k^+} \text{Tr}[\not h\Phi(k)] \mathcal{H}_{\mu\nu}(x,\bar{x}). \tag{89}$$

In either the DIS or the CF case, the structure function can then be obtained as an integral over dk_T^2 :

$$F_T^{\text{DIS}}(x_B, Q^2) = \int_0^{k_{T,\text{max}}^2} d\mathbf{k_T}^2 \ \mathcal{F}_T^{\text{DIS}}(\mathbf{k_T}^2)_{x_B, Q^2}$$
(90)

$$F_T^{\text{CF}}(x_B, Q^2) = \int_0^\infty d\mathbf{k_T}^2 \, \mathcal{F}_T^{\text{CF}}(\mathbf{k_T}^2)_{x_B, Q^2} \tag{91}$$

The crucial difference is the limit of integration: in the DIS case, k_T^2 is limited by four momentum conservation at any fixed value of the invariant mass W^2 , and the integrand does not have support beyond $k_{T,\max}^2$; in the CF calculation, k_T^2 can run up to infinity after being effectively decoupled from the light-cone plus and minus directions by the approximations (53)–(54).

The difference between the handling of k_T in the DIS and the CF calculations is evident from Figure 13, where the k_T -dependent \mathcal{F}_T structure functions are plotted as a function of k_T^2 for $x_B = 0.6$, $Q^2 = 4$ GeV², and nominal model parameter values.

At small k_T^2 , we have a generally good enough approximation, except when using the $\bar{x}=x_B$ scaling variable (blue line) that consistently underestimates the transverse structure function. On the contrary, taking into account both the target and the quark mass in the $\bar{x}=\xi_q$ scaling variable provides one with the best approximation achievable considering only external variables. Nonetheless, this calculation slightly overestimates the full one and displays a less steep slope. This cannot be remedied without handling the transverse motion of the quark in detail, which one cannot do at LT in collinear factorization; however, including the average $\langle k_T^2 \rangle$ in the theoretical $\bar{x}=\xi_{qT}^*$ scaling variable, one can obtain a good description on average of the full \mathcal{F}_T , slightly underestimating it at small k_T^2 values, and slightly overestimating it at intermediate k_T^2 values. This is the reason why the $\bar{x}=\xi_{qT}^*$ choice gives the best approximation for the k_T -integrated F_T previously discussed.

At even larger values of k_T^2 the factorized calculation is radically different: the black DIS curve displays an integrable divergence at $k_{T,\text{max}}^2$, while the CF colored curves have noticeable tails beyond that. At high Q^2 values, this happens at large enough k_T^2 that he unintegrated \mathcal{F}_T , dropping approximately as an inverse power of k_T^2 , does not contribute

much to the integrated F_T . However, at smaller Q^2 values the CF tail exceeding the kinematic limit provides a non negligible contribution to F_T . In order to quantify this contribution, we define the ratio

$$R(x_B, Q^2) = \frac{\int_{\mathbf{k}_{T,\text{max}}}^{\infty} d\mathbf{k}_T^2 \, \mathcal{F}_T^{\text{CF}}(\mathbf{k}_T^2)_{x_B, Q^2}}{\int_0^{\infty} d\mathbf{k}_T^2 \, \mathcal{F}_T^{\text{CF}}(\mathbf{k}_T^2)_{x_B, Q^2}} , \qquad (92)$$

that provides one with the relative amount of integrated F_T^{CF} coming from the 4-momentum non-conserving $k_T^2 > k_{T,\text{max}}^2$ region. In Table II, we collect the R values corresponding to each $x_{B,\text{break}}$ and denote these by R_{break} . As a rule of thumb we found that the CF calculation strongly deviates from the full calculation and factorization breaks down for (x_B, Q^2) values such that 20% or more of the integrated F_T^{CF} resides in the tail at $k_T^2 > k_{T,\text{max}}^2$.

The breaking of factorization just described is unavoidable, as it is rooted in the very approximation that allows one to define the quark PDF as an integral of the quark correlator Φ over the sub-leading parton momentum components k_T and k^+ , and to factorize these from the parton-level, hard scattering. Being rooted in kinematics, however, the values x_B and Q^2 at which the breakdown occurs can be at least qualitatively, if not semi-quantitatively, controlled by calculating the kinematic limits and estimating how far from these one should safely stay. As argued in the previous subsection in the context of our spectator model, a simple cut in W^2 may indeed be sufficient for inclusive structure functions. However, similar issues appear and are amplified in the case of semi-inclusive DIS measurements, and in particular when the hadron's transverse momentum is also measured [25, 26]. More refined analyses are urgently called for, especially in the context of the Jefferson Lab SIDIS program at the 12 GeV upgraded CEBAF facility [9], where the kinematics is inherently sub-asymptotic due to the relatively low beam energy.

C. Discussion: theory and phenomenology beyond the leading twist

In summary, there seems indeed to be a limit to the degree of accuracy with which a CF calculation can reproduce the inclusive DIS structure functions. This is due to 2 reasons:

- there is an intrinsic limitation in the approximation of high- k_T^2 scattering contributions, due to the neglect of transverse momentum conservation in the kinematic approximations;
- the \bar{x} scaling variable in inclusive processes can only be determined using external variables, and cannot incorporate the unobserved transverse momentum scale.

The first limitation is unavoidable, and one should try to identify in what region of phase space this occurs, to ensure factorization is properly applied to describe experimental data and, conversely, to accurately extract parton distribution from these. In this paper, we suggest that, at least for inclusive observables, a measure of control over the validity of the factorized description of the scattering can be reached by kinematic consideration, and in particular by estimating of the $x_{B,\text{max}}$. The latter can be calculated exactly in the model, where all masses are known and all particles are asymptotic states, but would require a dose of phenomenology in QCD to be usefully estimated. Identifying the region of applicability of factorization is, instead, more intricate in semi-inclusive measurements [25, 26].

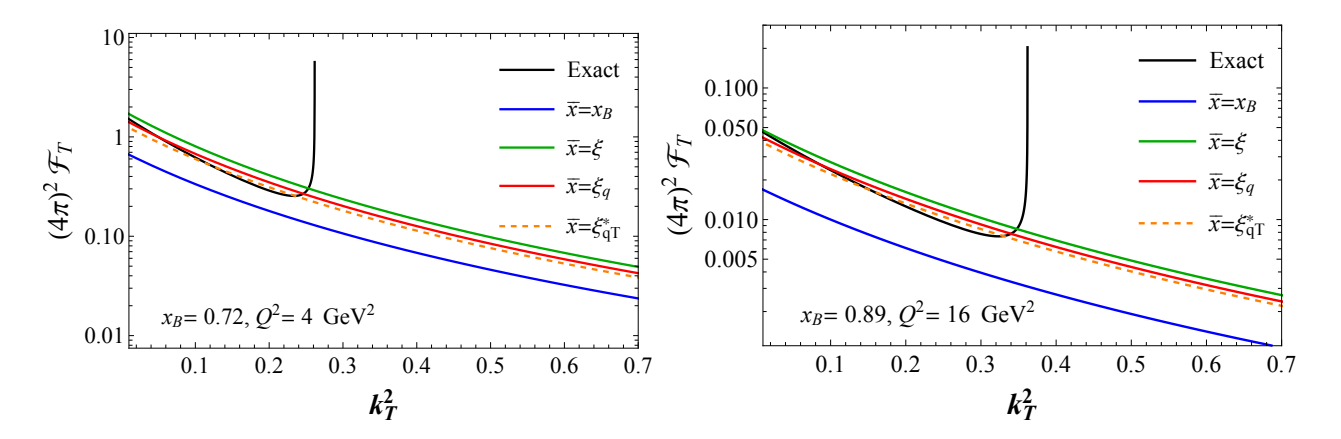


FIG. 13. k_T -dependent transverse structure function for the default parameters of the model. The two panels correspond to a low $Q^2 = 4$ GeV scale and a higher $Q^2 = 16$ GeV² scale. Their respective factorization breaking thresholds, $x_{B,\text{break}} = 0.72$ and $x_{B,\text{break}} = 0.89$ are chosen to maximize the difference between the factorized and full model calculations.

In both cases, we believe this is an important endeavor and more studies will be needed, lest we interpret as partonic features of the data that are not.

Even within the region of validity of factorization, an imperfect description of the DIS cross section at large x_B arises due to the neglect of transverse momentum in the factorized calculation at leading twist, see Figures 11, 12 and 17. However, after incorporating all external mass scales in the $\bar{x} = \xi_q$ scaling variable, the difference between the LT and the full cross section is small, and quite independent of the Λ and m_{ϕ} internal parameters that mimic the dynamics of the target in QCD. As demonstrated by incorporating $\langle k_T^2 \rangle$ in the scaling variable, these transverse momentum correction scale as powers of $\langle k_T^2 \rangle / Q^2$, and the calculation seems systematically improvable.

The needed control of the partonic k_T^2 accessed in the hard scattering reaction can be theoretically achieved either by utilizing the TMD factorization formalism, where parton distributions themselves depend on k_T [38, 39], or by performing collinear factorization up to higher twist level, in which case the transverse momentum dynamics is effectively included in multi-parton matrix elements [70].

Remaining in the context of collinear factorization, on can also try to absorb the contributions from the partonic transverse momentum into a phenomenological HT term to be fitted to the data:

$$F_T^{\text{DIS}}(x_B, Q^2) \approx F_T^{\text{CF}}(x_B, Q^2) + H(x_B)/Q^2$$
. (93)

Given a large enough leverage in Q^2 , the H(x) coefficient can clearly absorb the difference between the solid read and dashed orange curves in, say, Figure 12 and take care of the missing $O(\langle k_T^2 \rangle/Q^2)$ transverse momentum corrections. However, a fit to model pseudo-data is needed to establish the accuracy to which PDFs can be extracted given the still imperfect, and not improvable, estimate of the internal partonic kinematic provided by the ξ_q scaling variable, see Figure 9. We leave this phenomenological investigation, as well as a determination of the level to which the DIS contribution to the lepton-nucleon cross section can be separated from the interference and resonance contributions discussed in Section II D, to future work.

VI. SUMMARY AND CONCLUSIONS

In this work, we have presented a detailed model calculation designed to simulate the essential aspects of leptonproton scattering in QCD and to test the validity of collinear factorization at subasymptotic values of the hard scale Q^2 , where hadron and quark masses cannot be altogether neglected as customarily done in the Bjorken limit [17, 28, 33]. We have, in particular, focused our attention on inclusive observables as a first step towards an analysis of semi-inclusive scattering processes, in which the mass of the detected hadron comes also into play with non negligible effects in measurements performed at the Jefferson Lab, and higher beam energies up to the HERMES and COMPASS experiments [15, 16].

A. Collinear Factorization in DIS at sub-asymptotic Q^2

In the context of inclusive DIS, we have re-derived the factorization formula at LO with the aid of a final state quark jet function, explicitly separating the partonic internal kinematics, which needs to be approximated, from the hard scattering dynamics, that can be systematically expanded in powers of $|\mathbf{k}_T/Q|$ and, for light quarks, of m_q/Q . In particular, we have obtained a gauge invariant factorized formula for the leading power (or "leading-twist") contribution to the DIS cross section, that in fact coincides with the asymptotic formula evaluated at a rescaled variable \bar{x} instead of x_B . While our proof has been obtained at LO, its generalization to NLO should not present essential difficulties because any diagram at any order can be written as a trace term multiplied by an overall 4-momentum conservation delta function, as we have done in Eq. 48, thus isolating the part of the cross section in need of kinematic approximation from the part where the partonic dynamics comes into play, that can be expanded in a power series around collinear partons. This is the central idea of our approach: isolating the kinematics of the external legs of the hard scattering diagram from the rest, and performing a minimal set of (uncontrolled) approximations only there. The goodness of these approximations, can then be checked by factorizing the model cross section and comparing this to the full calculation.

The choice of the scaling variable \bar{x} is arbitrary, in principle, but can be guided by considering the kinematics of the hard vertex. In particular, we have verified that choosing $\bar{x} = \xi_q$ with $\xi_q \equiv \xi \left(1 + \frac{m_q^2}{Q^2}\right)$ one can reproduce the DIS cross section, with only a relatively small overestimation at the large values of x_B close to the inelastic scattering kinematic threshold. The variable ξ_q , originally proposed in [17], captures the kinematic effect of the initial state target mass and of the final state quark mass, and is analogous to the SIDIS scaling variable $\xi_h = \xi \left(1 + \frac{m_q^2}{\zeta_h Q^2}\right)$ proposed

in [14, 15] and successfully utilized in [16] to incorporate the corrections due to the mass of the observed hadron in the final state. The freedom guaranteed by our approach has also allowed us to explore the effects of $O(\mu^4/Q^4)$ mass corrections which are not necessarily small due to the parton becoming more and more offshell as one approaches the boundary of phase space at large x_B . Fortunately, these corrections turn out to be small, unless the mass of the quark is increased beyond the range suitable for our light-quark treatment.

The remaining difference between the CF and full calculation of the transverse structure function is mostly explained by incorporating the average $\langle k_T^2 \rangle$ in the scaling variable, and considering corrections only up to $O(\langle k_T^2 \rangle/Q^2)$. This procedure is only possible in a model, but as we found, the result is stable against variations of the internal confinement parameter Λ and mass of the target remnant m_ϕ . These results strongly suggest that the range of validity of collinear factorization can be maximized in the large- x_B and low- Q^2 region by extending the calculations to twist-4 level, either theoretically (including contributions from multi-parton diagrams) or phenomenologically (by adding a fitting a $H(x)/Q^2$ term to the LT factorized calculation). A fit of model pseudo-data is under way to verify if a phenomenological extraction of PDFs can be pushed to as large values of x_B as the factorized calculation, which is still underestimating by $\sim 10\%$ the values of $\langle x \rangle$ approximated by ξ_q .

Finally, as already pointed out in [28], we have explicitly illustrated an inherent limitation of collinear factorization, that breaks down at large x_B due to the neglect of momentum conservation in the transverse direction. Here, we suggest that the region in x_B and Q^2 where this happens might be semi-quantitatively controlled by kinematic considerations, and in fact a cut in invariant mass of the order of $W^2 \gtrsim 4 \text{ GeV}^2$ might circumscribe the factorization breaking region. Given that in QCD the excluded region corresponds to resonance excitations, which are outside the scope of the DIS handbag diagram, such a requirement does not seem to be an unduly restrictive condition.

These results are very encouraging regarding the validity of the treatment of hadron mass corrections advocated in Refs. [15, 16] for SIDIS and in Ref. [74] for semi-inclusive hadron annihilation in $e^+ + e^-$ scattering. In those works the scattered quark virtuality is bound by $v'^2 \ge m_h^2/\zeta$ (with m_h the identified hadron mass and ζ its light-cone fractional momentum) instead of $v'^2 \ge m_q^2$ as in the DIS case. It remains an important exercise to perform a similar model analysis for these two cases, and study the range of validity of collinear factorization for semi-inclusive processes, before extending the analysis to transverse momentum dependent measurements.

B. Beyond Deep Inelastic Scattering

The model used in this study has an even richer structure than summarized so far, as it also includes e+p resonant quasi-elastic scattering and the interference between this and the DIS scattering. (In fact, suitably generalized to higher mass resonances, the model may prove to be an useful tool in the study of quark-hadron duality [75], potentially allowing one to access PDFs in lepton-proton scattering processes at even higher x_B than currently possible.)

With a gauge-invariant decomposition of the physical process into these 3 pieces, we have shown that the interference and resonance contribution to the transverse F_T structure function exhibit an approximate $1/Q^2$ and $1/Q^4$ scaling. Thus one can also envision using model pseudo-data to test how effectively a phenomenological HT piece can decouple these from the DIS contribution in a PDF fit.

The longitudinal F_L structure function, instead, is constrained at smaller x by gauge invariance and does not exhibit the strongly ordered power-law scaling of its 3 components exhibited by F_T . Rather, all components are of the same order of magnitude and its $F_L^{\rm DIS}$ DIS component may substantially deviate from a CF calculation. In fact, small-x tensions between data and CF calculations have been recently exposed by small- x_B measurements at HERA [52–54]. A CF analysis of F_L in this region would require a NLO model calculation that is outside of the scope of the present article, but remains an interesting exercise for the future.

ACKNOWLEDGMENTS

We thank A. Bacchetta, L. Gamberg, M. Radici and A. Signori and for helpful discussions and remarks. This work was supported by the U.S. Department of Energy contract DE-AC05-06OR23177, under which Jefferson Science Associates LLC manages and operates Jefferson Lab. AA also acknowledges support from DOE contract DE-SC0008791. JVG also acknowledges partial support from the Jefferson Science Associates (JSA) 2018-2019 Graduate Fellowship Program. This work is also supported in part within the framework of the TMD Topical Collaboration.

Appendix A: Invariant and helicity structure functions

In Section II A, we discussed how to uniquely decompose a rank-2 tensor, $T^{\mu\nu}$, into a gauge invariant and a gauge breaking part. The procedure we adopted consists in defining a complete set of orthogonal rank-2 projectors, $\{P^{\mu\nu}_{\lambda}\}$, maximizing the number that satisfy the electromagnetic Ward identity, $q_{\mu}P^{\mu\nu}_{\lambda}$. For simplicity, in the main text we focused only on the parity invariant tensors, which are involved in neutral current exchanges such as in the model. In this appendix we complete that discussion by also consider the parity breaking tensors. We will also examine the $x_B \to 0$ limit of the structure functions, completing the analysis initiated in Section II E for the longitudinal F_L structure function.

We can now use the polarization vectors (12) to define the parity breaking helicity projectors for rank two tensors as

$$P_{[LS]}^{\mu\nu}(p,q) = \varepsilon_{+}^{\mu}(p,q)\varepsilon_{+}^{\nu*}(p,q) - \varepsilon_{-}^{\mu}(p,q)\varepsilon_{-}^{\nu*}(p,q) P_{[LS]}^{\mu\nu}(p,q) = \varepsilon_{0}^{\mu}(p,q)\varepsilon_{q}^{\nu*}(p,q) - \varepsilon_{q}^{\mu}(p,q)\varepsilon_{0}^{\nu*}(p,q).$$
(A1)

Using

$$\varepsilon_{+}^{\mu}(p,q)\varepsilon_{+}^{\nu*}(p,q) - \varepsilon_{-}^{\mu}(p,q)\varepsilon_{-}^{\nu*}(p,q) = \frac{-i\varepsilon^{\mu\nu\alpha\beta}p_{\alpha}q_{\beta}}{\sqrt{(p\cdot q)^{2} - p^{2}q^{2}}}$$
(A2)

and the explicit polarization vectors definition (12), the parity breaking projectors can be more compactly written in "Lorentz" representation as

$$P_A^{\mu\nu}(p,q) = \frac{-i\varepsilon^{\mu\nu\alpha\beta}\hat{p}_{\alpha}q_{\beta}}{\sqrt{-q^2\hat{p}^2}}$$

$$P_{[LS]}^{\mu\nu}(p,q) = \frac{\hat{p}^{\mu}q^{\nu} - q^{\mu}\hat{p}^{\nu}}{\sqrt{-q^2\hat{p}^2}}$$
(A3)

where $\hat{p}^{\mu} \equiv p^{\mu} - \frac{p \cdot q}{q^2} q^{\mu}$. In this form it is easy to verify that these two projectors are orthogonal to each other. Moreover, the parity breaking projectors are antisymmetric in the indices, and therefore also orthogonal to the parity invariant projectors (16), that are symmetric in the indices and we report here for reading convenience:

$$\begin{split} P_L^{\mu\nu}(p,q) &= \frac{\hat{p}^{\mu}\hat{p}^{\nu}}{\hat{p}^2} \\ P_T^{\mu\nu}(p,q) &= -\hat{g}^{\mu\nu} + \frac{\hat{p}^{\mu}\hat{p}^{\nu}}{\hat{p}^2} \\ P_S^{\mu\nu}(p,q) &= -\frac{q^{\mu}q^{\nu}}{q^2} \\ P_{\{LS\}}^{\mu\nu}(p,q) &= \frac{\hat{p}^{\mu}q^{\nu} + q^{\mu}\hat{p}^{\nu}}{\sqrt{-q^2\hat{p}^2}} \;, \end{split} \tag{A4}$$

with $\hat{g}^{\mu\nu} = g^{\mu\nu} - \frac{q^{\mu}q^{\nu}}{q^2}$. In summary,

$$\begin{split} P_{\lambda} \cdot P_{\lambda'} &= 0 & \text{for } \lambda \neq \lambda' \\ P_{\lambda} \cdot P_{\lambda} &= 1 & \text{for } \lambda = L, S \\ P_{\lambda} \cdot P_{\lambda} &= 2 & \text{for } \lambda = T \\ P_{\lambda} \cdot P_{\lambda} &= -2 & \text{for } \lambda = A, \{LS\}, [LS] \end{split} \tag{A5}$$

In the Lorentz representation (A3) and (A4), it is easy to convince oneself that these 6 defined projectors are also a complete orthogonal basis for the space of rank-2 tensors $T^{\mu\nu}=T^{\mu\nu}(p,q)$ built of the proton and photon momenta p and q, such as the hadronic tensor for inelastic e+p scattering.

Exploiting the the completeness of this basis, and noticing that the axial projector satisfy the Ward identity,

$$q \cdot P_A \equiv q_\mu P_A^{\mu\nu} = 0 , \qquad (A6)$$

we can extend to the anti-symmetric sector the decomposition (20) of a $T^{\mu\nu}$ tensor into a gauge invariant and maximally gauge breaking piece by defining

$$T^{\mu\nu} = T^{\mu\nu}_{\text{inv.}} + T^{\mu\nu}_{\text{g.b.}} ,$$
 (A7)

with

$$T_{\text{inv}}^{\mu\nu}(p,q) = P_T^{\mu\nu} F_T(x_B, Q^2) + P_L^{\mu\nu} F_L(x_B, Q^2) + P_A^{\mu\nu} F_A(x_B, Q^2)$$
(A8)

$$T_{\text{g.b.}}^{\mu\nu}(p,q) = P_S^{\mu\nu} F_S(x_B, Q^2) + P_{\{LS\}}^{\mu\nu} F_{\{LS\}} + P_{[LS]}^{\mu\nu} F_{[LS]} . \tag{A9}$$

The F_{λ} structure function are defined as in Eq. (18), i.e.,

$$F_{\lambda}(x_B, Q^2) \equiv c_{\lambda} P_{\lambda}(p, q) \cdot T(p, q) , \qquad (A10)$$

but with the index now ranging over the full range $\lambda = L, T, A, S, \{LS\}, [LS]$ and $c_{\lambda} = 1/P_{\lambda} \cdot P_{\lambda}$.

As demonstrated in Section II E, it is instructive to study the $x_B \to 0$ limit of the helicity projectors. Utilizing $\hat{p}^{\mu} \to -(p \cdot q/q^2)q^{\mu} = (1/2x_B)q^{\mu}$ and $\hat{p}^2 \to -(p \cdot q)^2/q^2 = -q^2/(2x_B)^2$, it is easy to see that

$$P_{T}^{\mu\nu} \xrightarrow[x_{B} \to 0]{} -g^{\mu\nu}$$

$$P_{L}^{\mu\nu} \xrightarrow[x_{B} \to 0]{} P_{S}^{\mu\nu} \qquad P_{\{LS\}}^{\mu\nu} \xrightarrow[x_{B} \to 0]{} -2P_{S}^{\mu\nu}$$

$$P_{A}^{\mu\nu} \xrightarrow[x_{B} \to 0]{} 0 \qquad P_{[LS]}^{\mu\nu} \xrightarrow[x_{B} \to 0]{} 0.$$
(A11)

Therefore, all structure functions except F_T are constrained at small x_B :

$$F_L \xrightarrow[\pi_S \to 0]{} F_S \qquad F_{\{LS\}} \xrightarrow[\pi_S \to 0]{} F_S$$
 (A12)

$$F_{L} \xrightarrow[x_{B} \to 0]{} F_{S} \qquad F_{\{LS\}} \xrightarrow[x_{B} \to 0]{} F_{S}$$

$$F_{A} \xrightarrow[x_{B} \to 0]{} 0 \qquad F_{[LS]} \xrightarrow[x_{B} \to 0]{} 0 .$$
(A12)

For gauge conserving interactions, such as electromagnetism, we furthermore find

$$F_L \xrightarrow[x_B \to 0]{} 0$$
. (A14)

An interesting consequence of this constrain, already discussed in Section IIE, is that

$$F_L^{\text{DIS}} \xrightarrow[x_B \to 0]{} -F_L^{\text{non-DIS}}$$
, (A15)

which alters the usual scaling expectations based on perturbative arguments, and introduces a novel source of "highertwist", or rather inverse Q^2 power corrections. In particular, we have explicitly demonstrated for electromagnetic interactions in our model that $F_L^{\rm DIS} \propto 1/Q^2$ in the small x_B limit, see also Appendix B. We remark, however, that Eq. (A14) is purely a consequence of gauge invariance, and therefore we expect this remark to be important also for the QCD interpretation of small- x_B measurements of the proton's F_L . Similar considerations are also valid for F_A and $F_{[LS]}$.

Appendix B: Scaling at small x_B

In this appendix, we justify from an analytic point of view the Q^2 scaling observed numerically for $F_L^{(j)}$ at small values of x_B in Figure 5. In fact, as also justified on the basis of gauge invariance considerations there and in more detail in Appendix B, all components of F_L are of order $1/Q^2$ in that limit, instead of being strongly ordered as in the transverse case, i.e., $F_T^{\rm DIS} \sim Q^2 F_T^{\rm INT} \sim Q^4 F_T^{\rm RES}$.

1. Small- x_B scaling of F_L

To compute $F_L^{(j)}$, we have to contract the longitudinal tensor P_L with the individual contributions to the hadronic tensor.

$$F_L^{(j)} = 2M P_L^{\mu\nu} W_{\mu\nu}^{(j)} \tag{B1}$$

$$= \frac{\pi}{4(2\pi)^3} \int_0^{k_{T,\text{max}}^2} dk_T^2 \iint \frac{dx}{x} dk^2 g^2(k^2) \frac{P_L \cdot \text{Tr}_{(j)}}{\text{Den}_{(j)}} \frac{1}{|J_{x,k^2,k_T^2}|} \delta(x - x_{\text{ex}}) \delta(k^2 - k_{\text{ex}}^2)$$
(B2)

where $\text{Tr}_{(j)} = \text{Tr}[...\gamma^{\mu}....\gamma^{\nu}...]$ are the traces appearing for each contribution and $\text{Den}_{(j)}$ are the respective denominators (note the traces and denominators in Eqs. (9)-(11)), while J_{x,k^2,k_T^2} is the Jacobian appearing after rewriting the final state delta functions in Eqs. (9)-(11), defined in Eq. (36).

At small x_B , we note from Eq. (40) that the light-cone virtuality follows $v^2 = k^2 + k_T^2 \sim 0$. Then the light cone fraction x, given by Eq. (38), can be expanded at small- x_B and fixed Q^2 value,

$$x = \xi \left(1 + \frac{m_q^2 - k^2}{Q^2} + O(\frac{\mu^4}{Q^4}) \right), \tag{B3}$$

where $\omega^2 = m_q^2 - k^2$. This is different from the "twist" expansion done in Eq. (39), where we assume $Q^2 \gg \mu^2$ (with μ any the scales involved) at fixed x_B . We also note from Eq. (40) that when $x_B \to 0$ the quark virtuality tends to $k^2 \to -k_T^2$, and then the two expansions, (39) and (B3), coincide at least up to $O(1/Q^2)$. In the low x_B limit, we note that:

$$x_{\rm ex} \to \xi \left(1 + \frac{\omega^2}{Q^2}\right)$$
 (B4)

$$\frac{v_{\text{ex}}^2}{x_{\text{ex}}} = \frac{k_{\text{ex}}^2 + k_T^2}{x_{\text{ex}}} \to -(m_\phi^2 - M^2) - k_T^2$$
(B5)

$$J_{x,k^2,\mathbf{k}_T^2} \to -\frac{Q^2}{x\,\xi} \tag{B6}$$

$$g(k^2) = g \frac{k^2 - m_q^2}{|k^2 - \Lambda^2|^2} \to -g \frac{m_q^2 + k_T^2}{|\Lambda^2 + k_T^2|^2} = -g \frac{\omega^2}{|\Lambda^2 + k_T^2|^2}$$
(B7)

$$k_{T,\text{max}}^2 \to \frac{Q^2}{4x_B}$$
 (B8)

and, therefore, we can write the longitudinal structure function for each contribution as,

$$F_L^{(j)} = \frac{\pi}{4(2\pi)^3} \frac{\xi}{Q^2} \int_0^{\mathbf{k}_{T,\text{max}}^2} d\mathbf{k}_T^2 \iint dx \, dk^2 \, g^2(k^2) \frac{P_L \cdot \text{Tr}_{(j)}}{\text{Den}_{(j)}} \delta(x - x_{\text{ex}}) \delta(k^2 - k_{\text{ex}}^2) \,. \tag{B9}$$

A factor $\frac{\xi}{Q^2}$ already explicitly appears in this equation. Therefore, to establish the Q^2 scaling behavior of the DIS, INT and RES contributions to F_L , we will need to study case by case the scaling of $P_L \cdot \text{Tr}_{(j)} / \text{Den}_{(j)}$.

We look firstly at the trace contributing to the DIS piece:

$$P_{L} \cdot \text{Tr}_{\text{DIS}} = \frac{1}{\hat{p}^{2}} \text{Tr} \left[(\not p + M) (\not k + m_{q}) \not p (\not k + \not q + m_{q}) \not p (\not k + m_{q}) \right]$$

$$= \frac{\omega^{2}}{2x_{B}} + O(x_{B}^{0})$$

$$= -4(k^{2} - m_{q}^{2}) \left(2k \cdot \hat{p} - k \cdot p - p \cdot q \right)$$

$$+ 4m_{q} M \left(2 \frac{\left(k \cdot \hat{p} \right)^{2}}{\hat{p}^{2}} - k \cdot q \right) + 4 \underbrace{\left(2k \cdot p + M m_{q} \right) \left(2 \frac{\left(k \cdot \hat{p} \right)^{2}}{\hat{p}^{2}} - k \cdot q - (k^{2} - m_{q}^{2}) \right)}_{O(x_{B}^{0})}$$

$$= 2 \frac{\omega^{4}}{x_{B}} + O(x_{B}^{0}). \tag{B10}$$

The denominator including the quark propagators for the DIS diagram is $Den_{DIS} = (k^2 - m_q^2)^2 = \omega^4$, and therefore we can write explicitly,

$$\frac{P_L \cdot \text{Tr}_{\text{DIS}}}{\text{Den}_{\text{DIS}}} = \frac{2}{x_B} + O(x_B^0). \tag{B11}$$

Notice that no additional Q^2 dependence is therefore introduced in Eq. (B9), and therefore F_L^{DIS} does scale as $1/Q^2$ at small x as observed numerically.

We can now repeat a similar calculation for the resonance contribution,

$$\begin{split} P_{L} \cdot \mathrm{Tr}_{\mathrm{RES}} &= \frac{1}{\hat{p}^{2}} \mathrm{Tr} \big[(\not p + M) \not p (\not p + \not q + M) (\not k + \not q + m_{q}) (\not p + \not q + M) \not p \big] \\ &= \frac{\omega^{2}}{2x_{B}} + O(x_{B}^{0}) \\ &= -4(W^{2} - M^{2}) \underbrace{\left(2k \cdot \hat{p} - k \cdot p - p \cdot q \right)}_{Q(1/x_{B}^{2})} + 4 \underbrace{\left(2(k + q) \cdot (p + q) + M m_{q} \right)}_{=W^{2} - M^{2} + O(x_{B}^{0})} \underbrace{\left(2\hat{p}^{2} - p \cdot q \right)}_{=\frac{1}{2x_{B}}(W^{2} - M^{2})} \\ &= 2 \underbrace{\frac{(W^{2} - M^{2})^{2}}{x_{B}}}_{(B12)} + O(1/x_{B}^{2}) \,, \end{split} \tag{B12}$$

where $(W^2 - M^2)^2 = Q^4/x_B^2 + O(1/x_B)$, but we keep it explicit in order to cancel exactly the denominator, $Den_{RES} = (W^2 - M^2)^2$. Then,

$$\frac{P_L \cdot \text{Tr}_{\text{RES}}}{\text{Den}_{\text{RES}}} = \frac{2}{x_B} + O(x_B^0)$$
(B13)

which corroborates the fact that $F_L^{\text{DIS}} = F_L^{\text{RES}}$ when $x_B \to 0$. Explicitly, we find that

$$F_L^{(j)} \to \frac{\pi}{2(2\pi)^3} \frac{\xi}{x_B} \frac{1}{Q^2} \int_0^{k_{T,\text{max}}^2} d\mathbf{k}_T^2 \ g^2(k^2)$$
 (j) = DIS, RES (B14)

which explains the $1/Q^2$ scaling observed in Figure 3 for small x_B . An analogous calculation can be done for the interference contribution to show that,

$$F_L^{\rm INT} \to -\frac{\pi}{(2\pi)^3} \frac{\xi}{x_B} \frac{1}{Q^2} \int_0^{k_{T,\text{max}}^2} d\mathbf{k_T}^2 \ g^2(k^2)$$
 (B15)

and then $F_L \to 0$ in the small- x_B limit.

2. Small- x_B scaling of F_T

The calculation for F_T is analogous to the one just performed for F_L , but in this case we must project the hadronic tensor with P_T . Then, in the low- x_B limit the transverse structure function for each contribution can be written as,

$$F_T^{(j)} = \frac{\pi}{8(2\pi)^3} \frac{\xi}{Q^2} \int_0^{k_{T,\text{max}}^2} d\mathbf{k_T}^2 \iint dx \, dk^2 \, g^2(k^2) \frac{P_T \cdot \text{Tr}_{(j)}}{\text{Den}_{(j)}} \delta(x - x_{\text{ex}}) \delta(k^2 - k_{\text{ex}}^2)$$
(B16)

Again, we need to focus on the Q^2 scaling of $\frac{P_L \cdot \text{Tr}_{(j)}}{\text{Den}_{(j)}}$. These DIS, INT and RES contributions can be computed and expanded in x_B , and they read

$$\frac{P_T \cdot \text{Tr}_{\text{DIS}}}{\text{Den}_{\text{DIS}}} = \frac{4Q^2}{\omega^2 x_B} + O(x_B^0)$$
(B17)

$$\frac{P_T \cdot \text{Tr}_{\text{INT}}}{\text{Den}_{\text{INT}}} = -\frac{8m_q^2}{\omega^2} + O(x_B)$$
(B18)

$$\frac{P_T \cdot \text{Tr}_{\text{RES}}}{\text{Den}_{\text{RES}}} = \frac{4(\omega^2 - 2M^2)}{Q^2} + O(x_B^2)$$
(B19)

Now, we can obtain the leading term for each of the contributions to the transverse structure function in the low $-x_B$ limit. We first focus on the DIS and interference contributions,

$$F_T^{\rm DIS} \to \frac{\pi}{2(2\pi)^3} \frac{\xi}{x_B} \int_0^{k_{T,\rm max}^2} d\mathbf{k_T}^2 \frac{g^2(k^2)}{\omega^2}$$
 (B20)

$$F_T^{\rm INT} \to -\frac{\pi}{(2\pi)^3} \frac{\xi m_q^2}{Q^2} \int_0^{k_{T,\rm max}^2} dk_T^2 \frac{g^2(k^2)}{\omega^2}$$
 (B21)

We first note a suppression of a factor $1/Q^2$ of the interference contribution compared to DIS, something observed in Figure 3 and this was the expected scaling from the structure of the hadronic tensor (10). Moreover, the factor ξ in the interference contribution explains why it approaches to $F_L^{\rm INT} \to 0$ when $x_B \to 0$, as one can note in Figure 3. For the resonance part, the transverse structure function in the low- x_B limit reads,

$$F_T^{\text{RES}} \to \frac{\pi}{2(2\pi)^3} \frac{\xi x_B}{Q^4} \int_0^{k_{T,\text{max}}^2} d\mathbf{k}_T^2 \ g^2(k^2)(\omega^2 - 2M^2)$$
 (B22)

$$= \frac{\pi}{2(2\pi)^3} \frac{\xi x_B}{Q^4} \left[g^2 \int_0^{\mathbf{k_{T,\text{max}}^2}} d\mathbf{k_T^2} \frac{(m_q^2 + \mathbf{k_T^2})^3}{(\Lambda^2 + \mathbf{k_T^2})^4} - 2M^2 \int_0^{\mathbf{k_{T,\text{max}}^2}} d\mathbf{k_T^2} g^2(k^2) \right]$$
(B23)

where the first term of the integral scales $\sim \log\left(\frac{Q^2}{4x_B\Lambda^2}\right)$ and breaks the expected naive scaling $\frac{1}{W^2-M^2}\sim 1/Q^4$, something observed numerically in Figure 3. This log term is a direct consequence of the dipole form factor used to simulate confinement; had we used an exponential form factor the resonance contribution would have followed the naive scaling $1/Q^4$. Despite this, the resonance contribution to F_T still vanishes at small x_B , as also observed in Figure 3, because of the x_B factor in front of the integral.

Appendix C: Kinematic bounds

We discuss here in some detail the kinematics of the model, and derive a number of bounds on relevant internal and external variables. The discussion, in fact, is general and does not rely on model peculiarities, nor is it confined to LO diagrams. A generalization to QCD will also be presented. As in the main text, we restrict our attention to the case of light quarks.

1. Limits on x_B

We start by considering the total invariant mass, W^2 ,

$$W^{2} = (p+q)^{2} = M^{2} + Q^{2} \left(\frac{1}{x_{B}} - 1\right).$$
 (C1)

In the model, by four momentum and lepton number conservation we can write

$$W^2 \ge (p_\phi + k')^2 \tag{C2}$$

where we have exploited the fact that a quark and a meson are the minimal mass final state that can be produced in an inelastic scattering. These particles in are asymptotic states of the model, and we can use $p_{\phi}^2 = m_{\phi}^2$, $k'^2 = m_q^2$ and $p_{\phi} \cdot k' \geq m_{\phi} m_q$ to derive an upper limit for x_B ,

$$x_B \le \frac{1}{1 + \frac{(m_\phi + m_q)^2 - M^2}{Q^2}} \equiv x_{B,\text{max}} .$$
 (C3)

The threshold $x_{B,\text{max}}$ corresponds to the production of the scattered quark and spectator meson at rest in the target rest frame.

In QCD, the quark needs to hadronize, minimally into a pion, and by baryon number conservation a proton must also be minimally present in the final state. The QCD threshold value can then be obtained from Eq. (C3) substituting $m_{\phi} \rightsquigarrow M$ and $m_{q} \rightsquigarrow m_{\pi}$, and is known as the "pion threshold" x_{π} :

$$x_{B|QCD} \le \frac{1}{1 + \frac{2m_{\pi}M + m_{\pi}^2}{Q^2}} \equiv x_{\pi} .$$
 (C4)

2. Limits on k_T^2

Given a finite final state invariant mass W^2 , the transverse momentum squared of the scattered quark is also limited. To derive its bounds, we consider the center of mass frame, where $\mathbf{k}' = -\mathbf{p}_{\phi}$ and $\mathbf{p}_{\phi,T} = -\mathbf{k}_T' = -\mathbf{k}_T$. Then,

$$W^{2} \ge (p_{\phi}^{0} + k^{\prime 0})^{2} = \left(\sqrt{m_{\phi}^{2} + \mathbf{k}_{T}^{2} + (p_{\phi}^{z})^{2}} + \sqrt{m_{q}^{2} + \mathbf{k}_{T}^{2} + (k^{\prime z})^{2}}\right)^{2}$$
(C5)

$$\geq \left(\sqrt{m_{\phi}^2 + \boldsymbol{k_T}^2} + \sqrt{m_q^2 + \boldsymbol{k_T}^2}\right)^2 \tag{C6}$$

where we have used $(p_{\phi}^z)^2 \ge 0$ and $(k'^z)^2 \ge 0$. Now, solving the last inequality imposes an upper limit in k_T^2 ,

$$\mathbf{k}_{T}^{2} \le \frac{\left(W^{2} - (m_{\phi} + m_{q})^{2}\right)\left(W^{2} - (m_{\phi} - m_{q})^{2}\right)}{4W^{2}} \equiv \mathbf{k}_{T,\text{max}}^{2}$$
 (C7)

Note that solving this for x_B when $k_{T,\text{max}}^2 = 0$ one recovers the upper limit Eq. (31). This is as it should, since $x_{B,\text{max}}$ corresponds to the production of the recoiled quark and spectator both at rest in the target rest frame.

As with the derivation of $x_{B,\text{max}}$, the transverse momentum bound in QCD can be obtained by substituting $m_{\phi} \rightsquigarrow M$ and $m_q \rightsquigarrow m_{\pi}$ in Eq. (C7).

3. Exact solutions of the delta functions

At LO, the unintegrated hadronic tensor contains two delta functions, see Eqs. (9)-(11), which originate from the upper and lower cuts in the diagrams of Figure 2. These delta functions impose

$$(k+q)^2 - m_q^2 = 0 (C8)$$

$$(p-k)^2 - m_\phi^2 = 0 (C9)$$

and the solutions of this equation system, denoted by $x_{\rm ex}$ and $k_{\rm ex}^2$, enter in the calculation of the k_T -unintegrated hadronic tensor (35). Note that Eqs. (C8) and (C9) are coupled. However, as we discussed in the main text, the upper cut (C8) provides the main constraint on the light cone fraction x, since k^2 only contributes to it at next to leading order in $1/Q^4$ (or rather $1/W^4$). The lower cut (C9) then constraints k^2 as a function of x.

In order to highlight the role of the W^2 scale in determining the kinematics of the process, we can express the hard scattering invariant mass, $(k+q)^2$, as

$$(k+q)^{2} = W^{2} + (k-p)^{2} + 2(p+q) \cdot (k-p)$$

$$= W^{2} + (k-p)^{2} + (1-\xi) \left(\frac{k^{2} + \mathbf{k}_{T}^{2}}{x} - M^{2}\right) + \frac{x-1}{1-\xi} W^{2}$$
(C10)

where in the last line we have used $W^2 = (1 - \xi) \left(M^2 + \frac{Q^2}{\xi} \right)$. Substituting this in Eq. (C8), and solving the resulting system, we obtain a relatively compact solution:

$$x_{\rm ex} = \frac{1+\xi}{2} - \frac{1-\xi}{2} \sqrt{\frac{4(\mathbf{k}_{T,\rm max}^2 - \mathbf{k}_T^2)}{W^2}} + \frac{(1-\xi)(m_q^2 - m_\phi^2)}{2W^2}$$
(C11)

$$k_{\rm ex}^2 = x_{\rm ex}M^2 - \frac{W^2}{2(1-\xi)} \left[1 - \sqrt{\frac{4(\mathbf{k_{T,max}^2 - k_T^2})}{W^2}} - \frac{m_q^2 + (1-2\xi)m_\phi^2}{W^2} \right]$$
(C12)

where $k_{T,\text{max}}^2$ is given by Eq. (C7). Note that Eqs. (C11) and (C12) highlight the role of the $k_{T,\text{max}}^2$ transverse momentum threshold, and explicitly show how the kinematics of the process is determined by the W^2 scale. It is therefore interesting to study their expansion in powers of $1/W^2$. Using

$$\sqrt{\frac{4(\boldsymbol{k}_{T,\text{max}}^2 - \boldsymbol{k}_T^2)}{W^2}} = 1 - \frac{m_q^2 + m_\phi^2 + 2\boldsymbol{k}_T^2}{W^2} - \frac{2(m_q^2 + \boldsymbol{k}_T^2)(m_\phi^2 + \boldsymbol{k}_T^2)}{W^4} + O\left(\frac{1}{W^6}\right), \tag{C13}$$

we find

$$x_{\text{ex}} = \xi + (1 - \xi) \frac{m_q^2 + k_T^2}{W^2} + (1 - \xi) \frac{(m_q^2 + k_T^2)(m_\phi^2 + k_T^2)}{W^4} + O\left(\frac{1}{W^6}\right)$$
(C14)

$$k_{\rm ex}^2 = \xi M^2 - \frac{\xi m_\phi^2 + k_T^2}{1 - \xi} + O\left(\frac{1}{W^2}\right)$$
 (C15)

We do not need to expand $k_{\rm ex}^2$ beyond the leading order because, as mentioned, the parton virtuality plays a role in the determination of $x_{\rm ex}$ only starting at $O(1/W^4)$. In the high-energy $W^2 \to \infty$ limit (reached, for example, when $x_B \to 0$ at fixed Q^2 , or when $Q^2 \to \infty$ at fixed x_B or ξ) one then easily sees that

$$x_{\text{ex}} \xrightarrow{W^2 \to \infty} x_B$$
 (C16)

$$k_{\rm ex}^2 \xrightarrow[W^2 \to \infty]{} x_B M^2 - \frac{x_B m_\phi^2 + k_T^2}{1 - x_B} \ .$$
 (C17)

In other words, the quark's light-cone momentum fraction becomes independent of the internal partonic kinematics, while the quark remains off its mass shell at any value of x_B (and by quite a large amount if $x_B \sim 1$).

A more compact expansion of $x_{\rm ex}$ can be obtained in terms of a $1/Q^2$ instead of $1/W^2$ power series, and in terms of the light-cone virtuality $v_{\rm ex}^2 = k_{\rm ex}^2 + k_T^2$ instead of the virtuality $k_{\rm ex}^2$. Indeed,

$$x_{\text{ex}} = \xi + \xi \frac{m_q^2 + \mathbf{k}_T^2}{Q^2} + \xi \frac{m_q^2 + \mathbf{k}_T^2}{Q^4} \frac{\xi(m_\phi^2 + \mathbf{k}_T^2 - (1 - \xi)M^2)}{1 - \xi} + O\left(\frac{1}{Q^6}\right)$$
(C18)

$$= \xi \left(1 + \frac{m_q^2 + \mathbf{k_T}^2}{Q^2} - \frac{(m_q^2 + \mathbf{k_T}^2)v_{\text{ex}}^2}{Q^4} + O\left(\frac{1}{Q^6}\right) \right) , \tag{C19}$$

where

$$v_{\rm ex}^2 = -\frac{\xi}{1-\xi} \left[(m_\phi^2 - M^2) + \xi M^2 + k_T^2 \right] + O\left(\frac{1}{Q^2}\right). \tag{C20}$$

Note that Eq. (C19) coincides with the expansion (39) discussed in the main text. It is now also clear that, as mentioned previously, v_{ex}^2 and therefore k_{ex}^2 only plays a role at $O(1/Q^4)$ or higher. Contrary to the ordinary virtuality k^2 , the light-cone virtuality vanishes at small Bjorken x_B :

$$v_{\text{ex}}^2 \xrightarrow[x_B \to 0]{} 0$$
. (C21)

4. Approximating v^2 in DIS

As discussed in Section III A, collinear factorization requires one to approximate the incoming and outgoing quark virtualities, namely to take $v^2 \approx \bar{v}^2$ and $v'^2 \approx \bar{v}'^2$. In this Section, we develop kinematic bounds on v^2 valid at any order in perturbation theory, and use these to obtain a good Ansatz for \bar{v}^2 . In the next Section we will turn our attention to \bar{v}'^2 .

Considering the lower vertex in the DIS diagrams of Figure 1 (i.e., target fragmentation) we find it is possible to obtain a quite simple expression for the parton virtuality in either the model, or in QCD. Starting with the model (Figure 1 right), we find that at Leading Order in the strong coupling constant,

$$m_{\phi}^{2} = (p - k)^{2} = 2(p^{+} - k^{+})(p^{-} - k^{-}) - \mathbf{k}_{T}^{2}$$
$$= (1 - x)\left(M^{2} - \frac{k^{2} + \mathbf{k}_{T}^{2}}{x}\right) - \mathbf{k}_{T}^{2}, \tag{C22}$$

hence the light cone virtuality $v^2 = k^2 + k_T^2$ reads

$$v^{2}|_{LO} = x \left[M^{2} - \frac{1}{1-x} (m_{\phi}^{2} + \mathbf{k}_{T}^{2}) \right]$$

$$= -\frac{x}{1-x} \left[(m_{\phi}^{2} - M^{2}) + xM^{2} + \mathbf{k}_{T}^{2}) \right].$$
(C23)

In the main text we dispensed from the LO subscript for simplicity, since all calculations are performed at that order. Note that the light-cone virtuality vanishes as $x \to 0$, and becomes negative as $x \to 1$. At intermediate values of x it can become slightly positive if one sets $m_{\phi} \ll M$, which is not the case if one wants the model to produce PDFs similar to the valence distribution in QCD. At higher perturbative orders, more than one particle can be produced in the target remnant, and p_{ϕ} needs to be considered a multi-particle state: $p_{\phi} \leadsto p_X$ and $m_{\phi}^2 \leadsto m_X^2 \ge m_{\phi}^2$. Hence, in general,

$$v^{2} \le -\frac{x}{1-x} \left[(m_{\phi}^{2} - M^{2}) + xM^{2} + k_{T}^{2}) \right],$$
 (C24)

with the upper bound saturated at LO, see Eq. (C23). Since the partonic cross section decrease at least as fast as an inverse v^2 power law, it is then reasonable to choose

$$\bar{v}^2 = -\frac{x}{1-x} \left[(m_\phi^2 - M^2) + xM^2 \right] \tag{C25}$$

as a minimal approximation of the average $\langle v^2 \rangle$, where we also neglected the internal variable k_T^2 that cannot be experimentally controlled in inclusive lepton-proton scattering.

In QCD, with the substitution $m_{\phi} \rightsquigarrow m_X \geq M$ because of baryon number conservation [16, 44], we obtain

$$v^2|_{\text{QCD}} \le -\frac{x}{1-x} \left[xM^2 + k_T^2 \right] ,$$
 (C26)

and, correspondingly, one can choose

$$\bar{v}^2|_{\text{QCD}} = -\frac{x^2}{1-x}M^2$$
 (C27)

In fact, at least for the applications discussed in this article, choosing for simplicity $\bar{v}^2 = 0$ over the whole x range seems sufficient because v^2 contributes to the factorized kinematics only at order $O(1/Q^4)$, see main text. Should one apply this analysis to regions closer to the kinematic thresholds, such as in a study of Quark-Hadron Duality, the light-cone virtuality could become quite large and the full Eqs. (C25) and (C27) might be needed.

5. Approximating $v^{\prime 2}$ in DIS

Consider now the jet subdiagram on top of Figure 6, in which the struck quark of momentum k' is fragmenting in a number of particles. By fermion number conservation, the incoming quark line should also pass the cut and appear in the final state. Thus, by 4-momentum conservation,

$$v'^2 = k'^2 + k_T'^2 \ge m_q^2 + k_T'^2$$
 (C28)

Note that in the model, where the quark can also exist as an asymptotic state, the lower bound is actually saturated at LO. In inclusive scattering, where no transverse momentum scale is measured, we can then only choose

$$\bar{v}^{\prime 2} = m_q^2 \tag{C29}$$

as approximate light-cone virtuality of the scattered quark, bearing in mind that this is actually smaller than $\langle v'^2 \rangle$. In QCD, instead, the quark needs to fragment into at least one hadron and therefore one should take into account the mass of the lightest hadron the quark can quark hadronize into, that is, the pion. Hence,

$$v_{\text{OCD}}^{\prime 2} \ge m_{\pi}^2 + k_T^{\prime 2} \ .$$
 (C30)

For a fully inclusive scattering, the light-cone virtuality can then be approximated by

$$\bar{v}_{\text{OCD}}^{\prime 2} = m_{\pi}^2 . \tag{C31}$$

Appendix D: Model systematics

In Secs. IV and V we tested the kinematic approximation and investigated the region of validity of collinear factorization for a selection of representative values of the target mass M and the quark m_q , both "external" parameters of the model. In this Appendix, complete the analysis of the systematics of the model results, by also varying the "internal" parameters of the model, which mimic physics that can not be experimentally controlled in DIS: the confinement scale Λ , and the proton remnant mass modeled by the spectator mass $m_{\phi} \sim \langle m_X \rangle$. The results are presented, in Figures 14-17, that share the same structure:

- the central panel corresponds to the default model parameters, determined by a fit of the model PDF to the quark PDFs of QCD phenomenologically fitted to experimental data as discussed in Section II, and the parameters are varied one by one in the horizontal, vertical, and diagonal directions, respectively;
- the horizontal and vertical rows show the variation of the spectator mass m_{ϕ} , and confinement scale Λ , respectively;
- the two diagonal rows show variations of the external target mass M and quark mass m_q .

The plots in Figure 14 show the behavior of $\langle {\bf k_T^2} \rangle$ as a function of x_B . As expected, $\langle {\bf k_T^2} \rangle \approx O(\Lambda^2)$ is not a priori negligible compared to the target and quark squared masses, M^2 and m_q^2 .

In Figure 15, we present a comparison between the average light-cone virtuality in the DIS process compared to the approximations $\bar{v}^2 = 0$, $\bar{v}^2 = \bar{v}_*^2$ [Eq. (75)], and $\bar{v}^2 = \bar{v}_{*T}^2$ [Eq. (79)]. The last two clearly better approximate $\langle v^2 \rangle$ at large x. However, the light-cone virtuality only contributes at $O(1/Q^4)$ to the determination of the struck quark momentum fraction, see for example Eq. 66, and these non-zero choices for \bar{v}^2 have a minor impact on the calculation of the CF structure functions (see also below).

In Figure 16, we compare the average light-cone fraction $\langle x \rangle$ to the collinear choices collected in Table I. As already discussed in Section IV C, the choice $\bar{x}=x_B$ approximation provides an inaccurate description of the parton's longitudinal kinematics, while $x=\xi_q$ describes $\sim 95\%$ of the light-cone fraction, with only minor improvements obtained when including non-zero virtuality $O(1/Q^4)$ corrections in $\bar{x}=\xi_q^*$. Only keeping into account the partonic transverse dynamics through $\langle k_T^2 \rangle/Q^2$ corrections in $\bar{x}=\xi_q$ can one obtain a fully accurate approximation.

Finally, in Figure 17 we show the ratio of the collinear structure functions to the exact one. This plots illustrate that the conclusions made from Figure 11 are not very sensitive to the variation of Λ and m_{ϕ} : a factorized calculation utilizing $\bar{x} = \xi_q$ provides nearly the best possible description of the full DIS structure function achievable only considering external variables, and the quality of this approximation is independent of the value of the internal (unobservable) model parameters. Taking into consideration the transverse momentum dynamics allows one to maximize the kinematic range of validity of the CF calculation before this unavoidably breaks down due to neglect of momentum conservation.

In Table III we present for all cases discussed in this Appendix the $x_{B,\text{break}}$ factorization breaking thresholds, and the corresponding invariant mass value. We also present the corresponding R_{break} relative contribution of the $k_T^2 > k_{T,\text{max}}^2$ tails to the factorized F_T structure function. As a rough summary, factorization breaks down $W^2 \gtrsim 4$ and 20% or more of the CF structure functions originates from k_T^2 values beyind the kinematic $k_{T,\text{max}}^2$ threshold imposed by four momentum conservation.

$x_{B,\mathrm{break}}$ I	$W_{\text{break}}^2 [\text{GeV}^2]$	$R_{ m break}$	$x_{B,\text{break}}$	$W_{\rm break}^2 \ [{ m GeV^2}]$	$R_{ m break}$	$x_{B,\text{break}}$	$W_{\rm break}^2 \ [{ m GeV^2}]$	$R_{\rm break}$
M = 0.75 GeV				$\Lambda = 0.45 \text{ GeV}$		$m_q = 0.8 \text{ GeV}$		
0.67	(2.5)	0.34	0.75	(2.2)	0.31	0.59	(3.7)	0.24
\overline{m}	$_{\phi}=0.65~\mathrm{GeV}$			Default			$m_{\phi} = 1 \text{ GeV}$	
0.83	(1.7)	0.24	0.72	(2.4)	0.29	0.61	(3.4)	0.34
				$\Lambda=0.8~{\rm GeV}$			$M=1.2~{\rm GeV}$	
			0.66	(2.9)	0.25	0.82	(2.3)	0.21

TABLE III. Factorization breaking thresholds $x_{B,\text{break}}$, (in parentheses) the corresponding values of invariant mass W_{break}^2 and R for $Q^2 = 4 \,\text{GeV}^2$ and the parameters variations discussed.

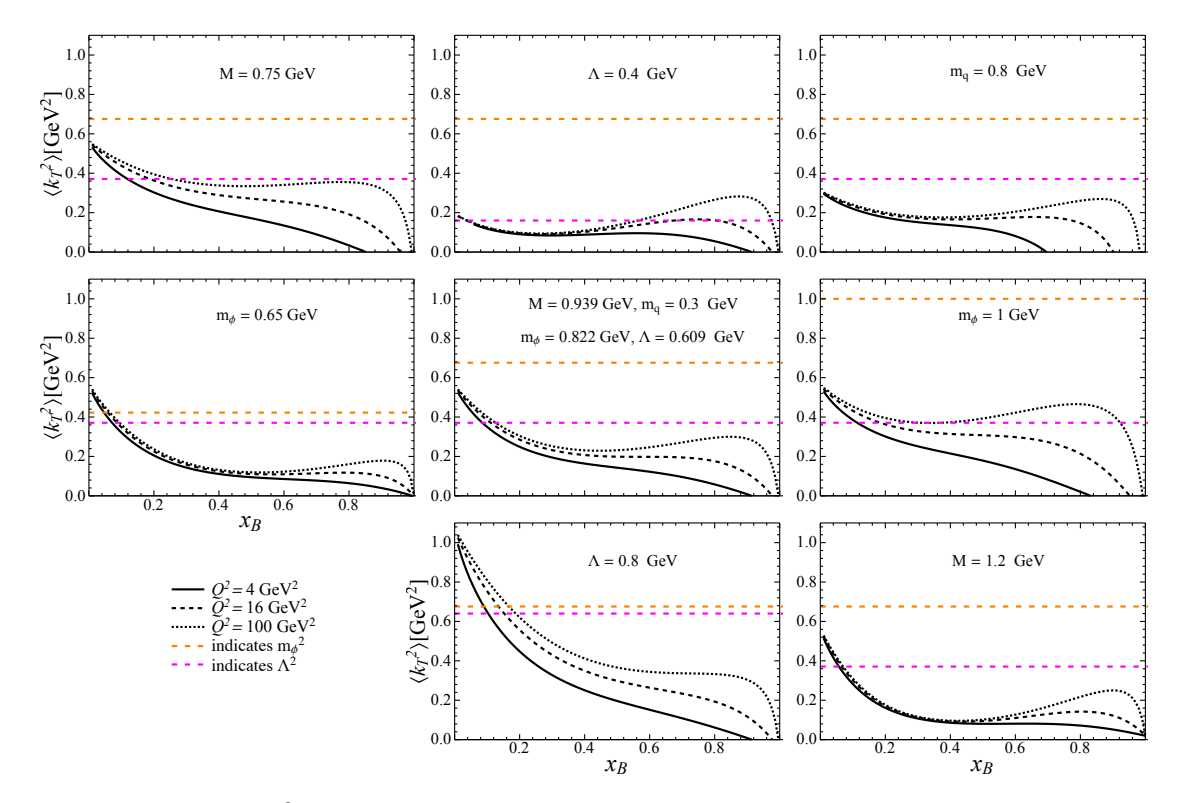


FIG. 14. Average unobserved k_T^2 of the incoming quark calculated in the full model as a function of x_B for various choices of Q^2 (black lines). Fore reference, the orange dashed line marks the chosen model m_q^2 value, and the magenta dashed line Λ^2 . The center plot corresponds to the default model parameters, while the others show variations of one parameter at a time.

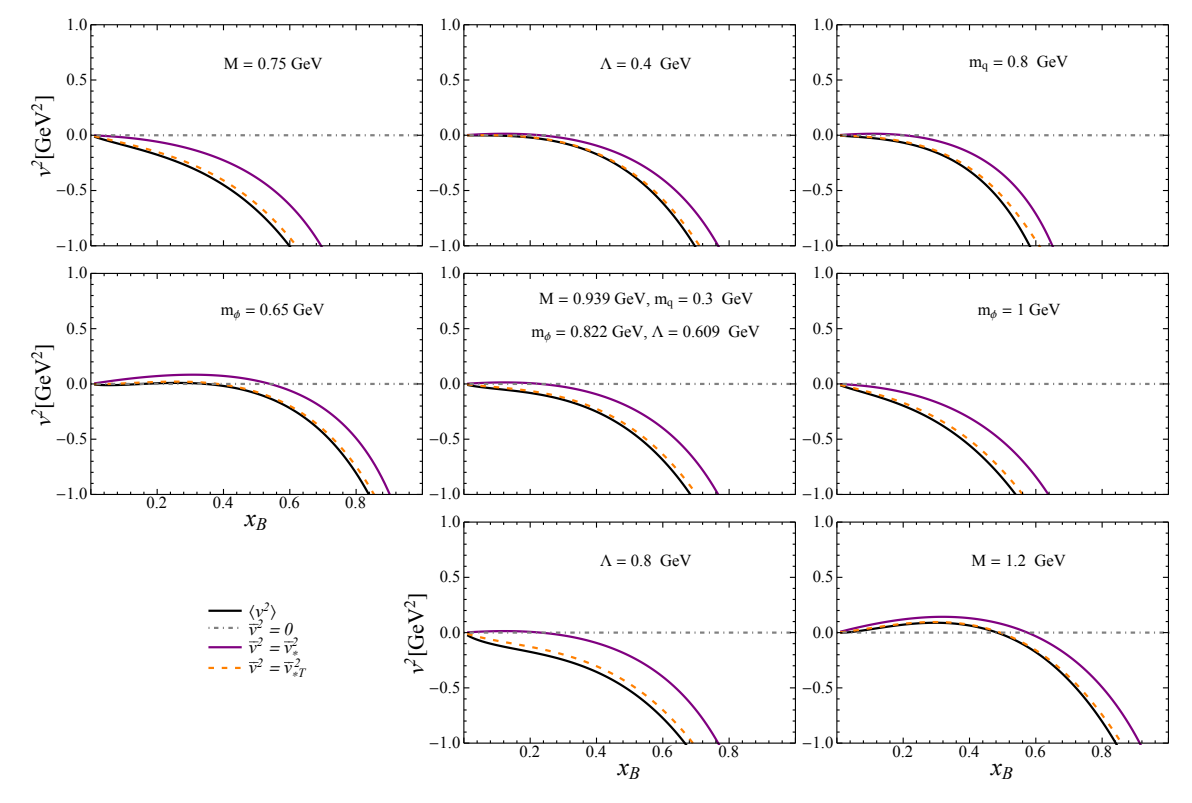


FIG. 15. Average light cone virtuality $v^2 = k^2 + k_T^2$ in the full model, compared to various collinear approximations. The center plot corresponds to the default model parameters, while the others show variations of one parameter at a time.

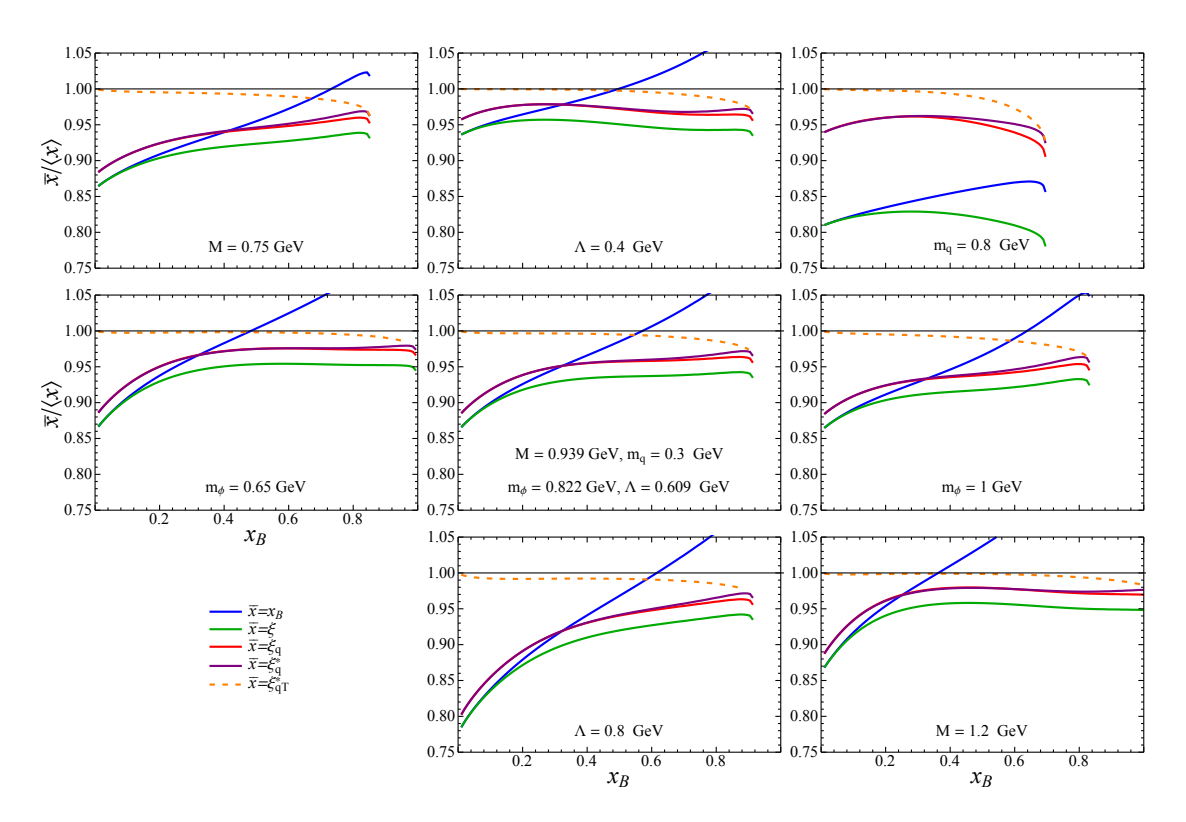


FIG. 16. Ratio of approximated \bar{x} parton light-cone momentum fraction to the full $\langle x \rangle$ calculated in the model at $Q^2 = 4 \text{ GeV}^2$. In the center panel plot, the default model parameters are used, and the other panels show the effect of varying one parameter at a time.

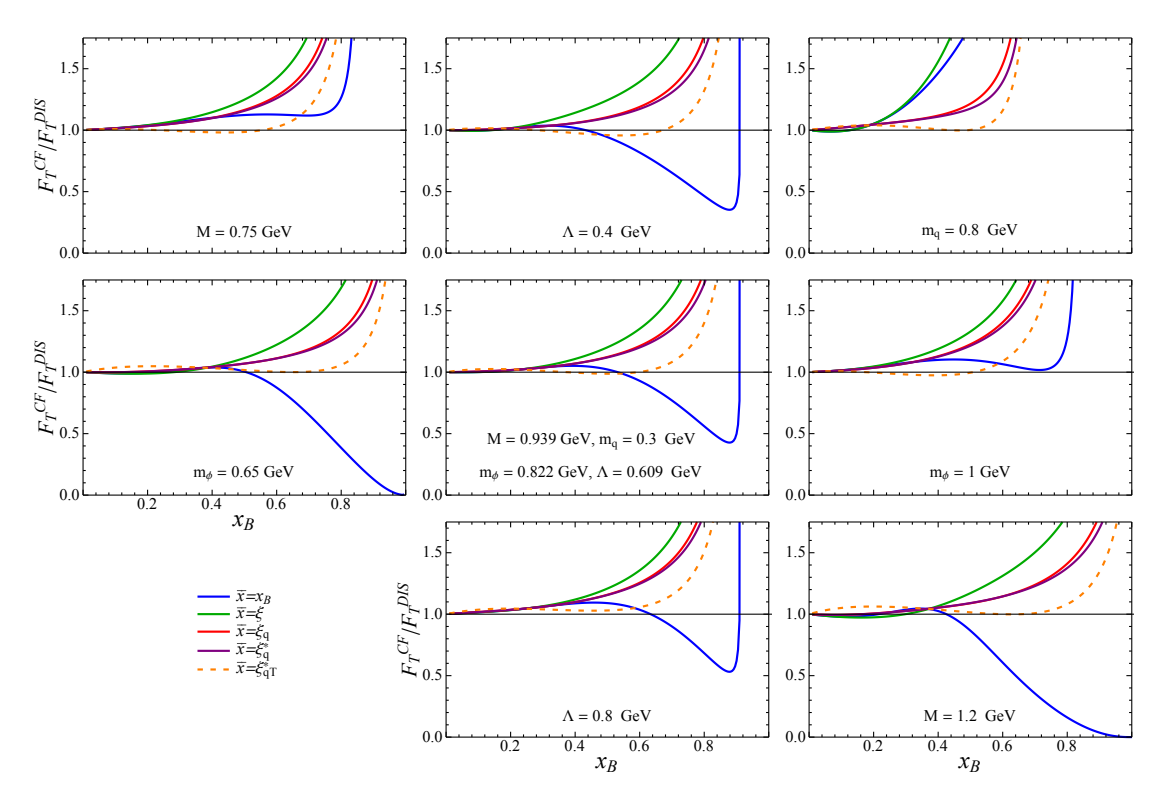


FIG. 17. Ratio of the factorized to full DIS structure functions calculated in the model at $Q^2 = 4 \text{ GeV}^2$. In the center panel plot, the default model parameters are used, and the other panels show the effect of varying one parameter at a time.

- [1] P. Jimenez-Delgado, W. Melnitchouk, and J. Owens, J. Phys. G 40, 093102 (2013), arXiv:1306.6515 [hep-ph].
- [2] J. Gao, L. Harland-Lang, and J. Rojo, Phys. Rept. 742, 1 (2018), arXiv:1709.04922 [hep-ph].
- [3] H.-W. Lin et al., Prog. Part. Nucl. Phys. 100, 107 (2018), arXiv:1711.07916 [hep-ph].
- [4] J. J. Ethier and E. R. Nocera, Ann. Rev. Nucl. Part. Sci., 1 (2020), arXiv:2001.07722 [hep-ph].
- [5] M. Constantinou et al., (2020), arXiv:2006.08636 [hep-ph].
- [6] T.-J. Hou et al., (2019), arXiv:1912.10053 [hep-ph].
- [7] S. Bailey and L. Harland-Lang, Eur. Phys. J. C 80, 60 (2020), arXiv:1909.10541 [hep-ph].
- [8] R. Abdul Khalek et al., (2020), arXiv:2005.11327 [hep-ph].
- [9] J. Dudek et al., Eur. Phys. J. A 48, 187 (2012), arXiv:1208.1244 [hep-ex].
- [10] V. D. Burkert, Ann. Rev. Nucl. Part. Sci. 68, 405 (2018).
- [11] A. Accardi et al., Eur. Phys. J. A52, 268 (2016), arXiv:1212.1701 [nucl-ex].
- [12] C. A. Aidala et al., Probing Nucleons and Nuclei in High Energy Collisions (WSP, 2020) arXiv:2002.12333 [hep-ph].
- [13] J. C. Collins, D. E. Soper, and G. F. Sterman, "Factorization of Hard Processes in QCD," (1989) pp. 1–91, arXiv:hep-ph/0409313.
- [14] A. Accardi, T. Hobbs, and W. Melnitchouk, JHEP 11, 084 (2009), arXiv:0907.2395 [hep-ph].
- [15] J. V. Guerrero, J. J. Ethier, A. Accardi, S. W. Casper, and W. Melnitchouk, JHEP 09, 169 (2015), arXiv:1505.02739 [hep-ph].
- [16] J. V. Guerrero and A. Accardi, Phys. Rev. D97, 114012 (2018), arXiv:1711.04346 [hep-ph].
- [17] M. A. G. Aivazis, F. I. Olness, and W.-K. Tung, Phys. Rev. D50, 3085 (1994), arXiv:hep-ph/9312318 [hep-ph].
- [18] S. Kretzer and M. H. Reno, Phys. Rev. D69, 034002 (2004), arXiv:hep-ph/0307023 [hep-ph].
- [19] S. Albino, B. A. Kniehl, and G. Kramer, Nucl. Phys. B803, 42 (2008), arXiv:0803.2768 [hep-ph].
- [20] A. Airapetian et al. (HERMES), Phys. Rev. D87, 074029 (2013), arXiv:1212.5407 [hep-ex].
- [21] C. Adolph *et al.* (COMPASS), Phys. Lett. **B767**, 133 (2017), arXiv:1608.06760 [hep-ex].
- [22] E. Seder (COMPASS), Proceedings, 23rd International Workshop on Deep-Inelastic Scattering and Related Subjects (DIS 2015): Dallas, Texas, USA, April 27-May 01, 2015, PoS **DIS2015**, 214 (2015).
- [23] R. Akhunzyanov et al. (COMPASS), Phys. Lett. **B786**, 390 (2018), arXiv:1802.00584 [hep-ex].
- [24] G. D. Alexeev et al. (COMPASS), Phys. Lett. **B807**, 135600 (2020), arXiv:2003.11791 [hep-ex].
- [25] J. Gonzalez-Hernandez, T. Rogers, N. Sato, and B. Wang, Phys. Rev. D 98, 114005 (2018), arXiv:1808.04396 [hep-ph].
- [26] M. Boglione, A. Dotson, L. Gamberg, S. Gordon, J. Gonzalez-Hernandez, A. Prokudin, T. Rogers, and N. Sato, JHEP 10, 122 (2019), arXiv:1904.12882 [hep-ph].
- [27] A. Bacchetta, F. Conti, and M. Radici, Phys. Rev. D78, 074010 (2008), arXiv:0807.0323 [hep-ph].
- [28] E. Moffat, W. Melnitchouk, T. C. Rogers, and N. Sato, Phys. Rev. D95, 096008 (2017), arXiv:1702.03955 [hep-ph].
- [29] J. V. Guerrero and A. Accardi, Proceedings, 27th International Workshop on Deep Inelastic Scattering and Related Subjects (DIS 2019): Torino, Italy, April 8-12, 2019, PoS DIS2019, 015 (2019), arXiv:1906.01191 [hep-ph].
- [30] J. V. Guerrero, Hadron Mass Corrections in Deep Inelastic Scattering, Ph.D. thesis (2019).
- [31] I. Abt, A. M. Cooper-Sarkar, B. Foster, V. Myronenko, K. Wichmann, and M. Wing, Phys. Rev. D94, 034032 (2016), arXiv:1604.02299 [hep-ph].
- [32] W.-K. Tung, S. Kretzer, and C. Schmidt, Proceedings, Ringberg Workshop on New Trends in HERA Physics 2001: Ringberg Castle, Tegernsee, Germany, June 17-22, 2001, J. Phys. G28, 983 (2002), arXiv:hep-ph/0110247 [hep-ph].
- [33] P. M. Nadolsky and W.-K. Tung, Phys. Rev. D79, 113014 (2009), arXiv:0903.2667 [hep-ph].
- [34] R. Ellis, W. Furmanski, and R. Petronzio, Nucl. Phys. B 212, 29 (1983).
- [35] H. Georgi and H. D. Politzer, Phys. Rev. D14, 1829 (1976).
- [36] P. Frampton, Lett. Nuovo Cim. 17, 499 (1976).
- [37] O. Nachtmann, Nucl. Phys. **B63**, 237 (1973).
- [38] A. Bacchetta, M. Diehl, K. Goeke, A. Metz, P. J. Mulders, and M. Schlegel, JHEP 02, 093 (2007), arXiv:hep-ph/0611265 [hep-ph].
- [39] J. Collins, Camb. Monogr. Part. Phys. Nucl. Phys. Cosmol. 32, 1 (2011).
- [40] S. Chekanov et al. (ZEUS), Phys. Rev. D67, 012007 (2003), arXiv:hep-ex/0208023 [hep-ex].
- [41] C. Adloff et al. (H1), Phys. Lett. B528, 199 (2002), arXiv:hep-ex/0108039 [hep-ex].
- [42] J. J. Aubert et al. (European Muon), Nucl. Phys. **B213**, 31 (1983).
- [43] A. Bacchetta, "Transverse momentum distributions," (2012), http://www2.pv.infn.it/\$\sim\$bacchett/teaching/Bacchetta\$_\$Trento2012.pdf. Lecture Notes, Unpublished.
- [44] A. Accardi and J.-W. Qiu, JHEP **07**, 090 (2008), arXiv:0805.1496 [hep-ph].
- [45] M. Virchaux and A. Milsztajn, Phys. Lett. **B274**, 221 (1992).
- [46] A. Accardi, M. E. Christy, C. E. Keppel, W. Melnitchouk, P. Monaghan, J. G. Morfín, and J. F. Owens, Phys. Rev. D81, 034016 (2010), arXiv:0911.2254 [hep-ph].
- [47] J. F. Owens, A. Accardi, and W. Melnitchouk, Phys. Rev. D87, 094012 (2013), arXiv:1212.1702 [hep-ph].
- [48] A. Accardi, L. T. Brady, W. Melnitchouk, J. F. Owens, and N. Sato, Phys. Rev. D93, 114017 (2016), arXiv:1602.03154 [hep-ph].
- [49] S. I. Alekhin, S. A. Kulagin, and S. Liuti, Phys. Rev. D69, 114009 (2004), arXiv:hep-ph/0304210 [hep-ph].
- [50] S. Alekhin, J. Blümlein, S. Moch, and R. Placakyte, Phys. Rev. **D96**, 014011 (2017), arXiv:1701.05838 [hep-ph].

- [51] A. Bacchetta, F. G. Celiberto, M. Radici, and P. Taels, (2020), arXiv:2005.02288 [hep-ph].
- [52] V. Andreev et al. (H1), Eur. Phys. J. C74, 2814 (2014), arXiv:1312.4821 [hep-ex].
- [53] H. Abramowicz et al. (ZEUS), Phys. Rev. D90, 072002 (2014), arXiv:1404.6376 [hep-ex].
- [54] H. Abramowicz et al. (H1, ZEUS), Eur. Phys. J. C75, 580 (2015), arXiv:1506.06042 [hep-ex].
- [55] J. Bartels, K. J. Golec-Biernat, and K. Peters, Eur. Phys. J. C17, 121 (2000), arXiv:hep-ph/0003042 [hep-ph].
- [56] L. A. Harland-Lang, A. D. Martin, P. Motylinski, and R. S. Thorne, Eur. Phys. J. C76, 186 (2016), arXiv:1601.03413 [hep-ph].
- [57] L. Motyka, M. Sadzikowski, W. Słomiński, and K. Wichmann, Eur. Phys. J. C78, 80 (2018), arXiv:1707.05992 [hep-ph].
- [58] H. Abdolmaleki et al. (xFitter Developers' Team), Eur. Phys. J. C78, 621 (2018), arXiv:1802.00064 [hep-ph].
- [59] R. D. Ball, V. Bertone, M. Bonvini, S. Marzani, J. Rojo, and L. Rottoli, Eur. Phys. J. C78, 321 (2018), arXiv:1710.05935 [hep-ph].
- [60] J. Bartels, K. J. Golec-Biernat, and H. Kowalski, Phys. Rev. **D66**, 014001 (2002), arXiv:hep-ph/0203258 [hep-ph].
- [61] F. Gelis, E. Iancu, J. Jalilian-Marian, and R. Venugopalan, Ann. Rev. Nucl. Part. Sci. 60, 463 (2010), arXiv:1002.0333 [hep-ph].
- [62] A. Accardi and A. Signori, Phys. Lett. **B798**, 134993 (2019), arXiv:1903.04458 [hep-ph].
- [63] A. Accardi and A. Signori, (2020), arXiv:2005.11310 [hep-ph].
- [64] M. Procura and I. W. Stewart, Phys. Rev. D 81, 074009 (2010), [Erratum: Phys.Rev.D 83, 039902 (2011)], arXiv:0911.4980 [hep-ph].
- [65] J. C. Collins, T. C. Rogers, and A. M. Stasto, Phys. Rev. D77, 085009 (2008), arXiv:0708.2833 [hep-ph].
- [66] A. V. Manohar, Phys. Lett. B 633, 729 (2006), arXiv:hep-ph/0512173.
- [67] A. Accardi and A. Signori, Proceedings, 26th International Workshop on Deep Inelastic Scattering and Related Subjects (DIS 2018): Port Island, Kobe, Japan, April 16-20, 2018, PoS DIS2018, 158 (2018), arXiv:1808.00565 [hep-ph].
- [68] R. L. Jaffe, in The spin structure of the nucleon. Proceedings, International School of Nucleon Structure, 1st Course, Erice, Italy, August 3-10, 1995 (1996) pp. 42–129, arXiv:hep-ph/9602236 [hep-ph].
- [69] R. Jaffe, Nucl. Phys. B 229, 205 (1983).
- [70] J.-W. Qiu, Phys. Rev. **D42**, 30 (1990).
- [71] A. Accardi and A. Bacchetta, Phys. Lett. **B773**, 632 (2017), arXiv:1706.02000 [hep-ph].
- [72] E. Moffat, T. C. Rogers, W. Melnitchouk, N. Sato, and F. Steffens, Phys. Rev. D99, 096008 (2019), arXiv:1901.09016 [hep-ph].
- [73] L. Gamberg, Z.-B. Kang, I. Vitev, and H. Xing, Phys. Lett. **B743**, 112 (2015), arXiv:1412.3401 [hep-ph].
- [74] A. Accardi, D. P. Anderle, and F. Ringer, Phys. Rev. **D91**, 034008 (2015), arXiv:1411.3649 [hep-ph].
- [75] W. Melnitchouk, R. Ent, and C. Keppel, Phys. Rept. 406, 127 (2005), arXiv:hep-ph/0501217 [hep-ph].